Kinetic Modeling of Amyloid Fibrillation and Synaptic Plasticity as Memory Loss and Formation Mechanisms

by

Chuang-Chung (Justin) Lee

B.S. Chemical Engineering
National Taiwan University, 2001

M.S. Chemical Engineering Practice
Massachusetts Institute of Technology, 2005

SUBMITTED TO THE DEPARTMENT OF CHEMICAL ENGINEERING IN PARTIAL FULFILLMENT OF THE REQUIREMENTS FOR THE DEGREE OF

DOCTOR OF PHILOSOPHY IN CHEMICAL ENGINEERING
AT THE
MASSACHUSETTS INSTITUTE OF TECHNOLOGY
[June 2008]
MAY 2008

Author.....
Department of Chemical Engineering
May 5, 2008

Certified by.....
Gregory J. McRae
Hoyt C. Hottel Professor of Chemical Engineering
Thesis Supervisor

Accepted by.....
William M. Deen
Professor of Chemical Engineering
Chairman, Committee on Graduate Students

Kinetic Modeling of Amyloid Fibrillation and Synaptic Plasticity as Memory Loss and Formation Mechanisms

by

Chuang-Chung (Justin) Lee

Submitted to the Department of Chemical Engineering
on May 15, 2008 in Partial Fulfillment of the Requirements for the Degree of
Doctor of Philosophy at Massachusetts Institute of Technology

Abstract

The principles of biochemical kinetics and system engineering are applied to explain memory-related neuroscientific phenomena. Amyloid fibrillation and synaptic plasticity have been our focus of research due to their significance. The former is related to the pathology of many neurodegenerative diseases and the later is regarded as the principal mechanism underlying learning and memory.

Claimed to be the number one cause of senile dementia, Alzheimer's disease (AD) is one of the disorders that involve misfolding of amyloid protein and formation of insoluble fibrils. Although a variety of time dependent fibrillation data *in vitro* are available, few mechanistic models have been developed. To bridge this gap we used chemical engineering concepts from polymer dynamics, particle mechanics and population balance models to develop a mathematical formulation of amyloid growth dynamics. A three-stage mechanism consisting of natural protein misfolding, nucleation, and fibril elongation phases was proposed to capture the features of homogeneous fibrillation responses. While our cooperative laboratory provided us with experimental findings, we guided them with experimental design based on modeling work. It was through the iterative process that the size of fibril nuclei and concentration profiles of soluble proteins were elucidated. The study also reveals further experiments for diagnosing the evolution of amyloid coagulation and probing desired properties of potential fibrillation inhibitors.

Synaptic plasticity at various time ranges has been studied experimentally to elucidate memory formation mechanism. By comparison, the theoretical work is underdeveloped and insufficient to explain some experiments. To resolve the issue, we developed models for short-term, long-term, and spike timing dependent synaptic plasticity, respectively. First, presynaptic vesicle trafficking that leads to the release of glutamate as neurotransmitter was taken into account to explain short-term plasticity data. Second, long-term plasticity data lasting for hours after tetanus stimuli has been matched by a calcium entrapment model we developed. Model differentiation was done to demonstrate the better performance of calcium entrapment model than an alternative bistable theory in fitting graded long-term potentiation responses. Finally, to decipher spike timing dependent plasticity (STDP), we developed a systematic model incorporating backpropagation of action potential, dual requirement of NMDA receptors, and calcium dependent plasticity. This built model is supported by five different types of STDP experimental data.

The accumulation of amyloid beta has been found to disrupt the sustainable modification of long-term synaptic plasticity which might explain the inability of AD patients to form new memory at early stage of the disease. Yet the linkage between the existence of amyloid beta species and failure of long-term plasticity was unclear. We suggest that the abnormality of calcium entrapment function caused by amyloid oligomers is the intermediate step that eventually leads to memory loss. Unsustainable calcium level and decreased postsynaptic activities result into the removal or internalization of alpha-amino-3-hydroxy-5-methyl-4-isoxazolepropionic acid (AMPA) receptors. The number of AMPA receptors as the indicators of synaptic strength may result into disconnection between neurons and even neuronal apoptosis. New experiments have been suggested to validate this hypothesis and to elucidate the pathology of Alzheimer's disease.

Thesis supervisor: Gregory J. McRae
Hoyt C. Hottel Professor of Chemical Engineering

Acknowledgement

Five years at MIT have been the time of my life. In addition to the wonderful environment for pursuing advancement in technology, the professors and students here are extraordinary. I am grateful for graduating from MIT on time as much as being able to get enrolled here in the first place. There are of course a group of people who made this possible and I would like to express my thanks to them.

First of all, my family supported me to come to MIT for advanced education. My lovely parents, Ching-Jieh Lee and Shuei-Mien Cheng, have been encouraging me whenever I face any difficulty at graduate school. My dear brother, Chuang-Yuan Lee, was doing his PhD in Los Angeles while I have been working on mine here in Boston. Thus, we cheered each other up during our days as PhD students. My wife Jiejin Chen, also an MIT graduate student, loved me and supported me throughout our time working on the thesis.

Thanks to the generosity of my advisor, Prof. Gregory J. McRae, I can enjoy the interdisciplinary research between chemical engineering and neuroscience. Also valuable is the statistical way of thinking he instilled, which is applicable to a variety of fields. Also the guidance from Dr. Chi-Sang Poon helps me in strengthening my background of neuroscience and directs me to the prominent research topic in this field. In addition at each thesis committee meeting, other committee members, including Prof. Gregory Stephanopoulos, Prof. Georges Belfort, and Prof. Narendra Maheshri, always gave me thoughtful and helpful comments and questions.

Quite a few experimental work of amyloid fibrillation was carried out by Prof. Belfort's group at Rensselaer Polytechnic Institute. Prof. Belfort and Arpan Nayak cooperated with us for three years within which we put experimental and modeling work together. Also thanks to their fellow students, Ananthakrishnan Sethuraman, Amit Dutta, and Mirco Sorci for the contribution.

Also I feel lucky being able to work with my colleagues at McRae research group: Mihai Anton, Alex Lewis, Ingrid Berkelmans, Bo Gong, Anusha Kothandaraman, Kenneth Hu, and Adekunle Adeyemo. Because of them, my life as a graduate student was joyful as well as productive.

Research done in the thesis has been funded by U.S. Department of Energy (DOE), British Petroleum (BP), and Novartis Pharmaceuticals. I have been very grateful for the financial support provided throughout the whole doctoral program.

Table of Content

List of Figures

List of Tables

1 Introduction

1.1 Thesis statement

Learning and memory has been an active research field in neuroscience. Memory formation mechanisms and the causes of memory loss have been intensively studied yet there remain a great deal of unresolved issues and unanswered questions in both areas. For instance, what are the physiological reactions, mostly reversible, that lead to irreversible memory formation? What are the pathological species that cause memory loss? The list of unanswered memory-related questions can go on and on but some problems are more urgent than others.

There are two eminent reasons for studying learning and memory. The first one is the U.S. society is aging rapidly and senility is a significant risk factor for many neurodegenerative diseases. Since amyloid beta (Aβ) fibrillation is the most suspected cause of Alzheimers' disease, theoretical and experimental work on Aβ has been intensively carried out in hope of understanding the disease mechanism before the development of corresponding therapy. The second one is memory is closely related to the advancement of technology. The dramatic surge of information available at internet age is daunting. The capability of understanding memory formation mechanisms and utilizing them can be a rate determining step toward taking advantage of the information space.

Neurons are the basic unit of information processing in the nervous system. A single neuron is capable of receiving and transmitting signals at precise timing. The basic structure of neurons is shown in Figure 1-1. The cell body of neurons contains basic functional components such as nucleus, ribosome, and mitochondria. The axon is the long cable-like structure that transfers electrochemical signal to the further end. Dendrites are the branch-like structure that exists on either end [51]. Finally, neurons are physically connected with one another through linking structure called synapse. Also synapses can transfer signals across neurons chemically or electrically [77]. They have been intensively studied because synaptic plasticity, the ability of connections between neurons to change in strength, has been recognized as the underlying mechanism of learning and memory.

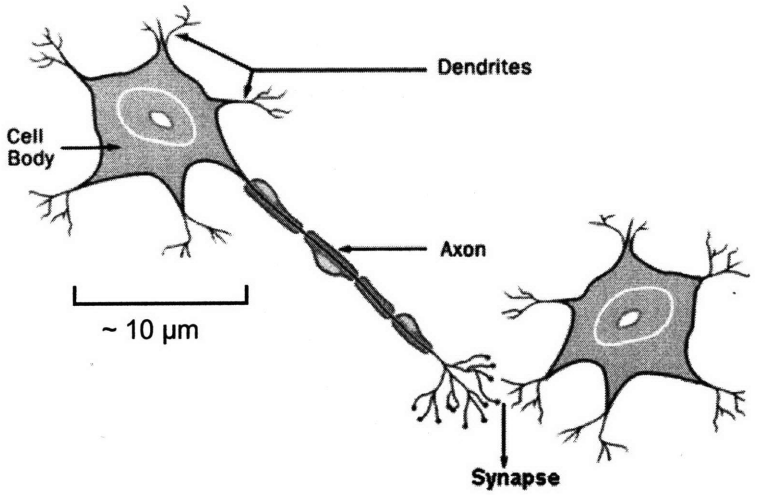

Figure 1-1 Basic neuron structure with key components labeled [51].

Half century ago, two mathematical models developed in neuroscience have great impact on the study of neuronal systems. The first one was Hebb's learning rule that predict the activity-dependent synaptic strength [65]. This synaptic plasticity updating rule is crucial in evaluating how connections may evolve for neuronal networks under stimulation. The rule and its derivatives have been widely used as the leading rule in artificial learning and memory. The second one was the Hodgkin-Huxley model that well explained the dynamics of action potentials by developing equivalent electrical circuits to mimic ion flows across neuronal membranes [68]. The circuits incorporate variable conductance to follow the dynamics of ion channels and capacitors to represent the neuronal membranes that separate charges. The output responses of the model include the action potential itself as well as the sodium and potassium currents that lead to the change in membrane potentials.

The principles of chemical engineering are fairly applicable for unraveling the complicated issues of learning and memory. Even though the systems of interest between these two fields are different, the fundamental principles in fact remain similar. Also interdisciplinary research may facilitate generation of new theories through exchange of ideas. First, the reaction kinetics provides guidelines for setting up physiological reaction schemes either *in vivo* or at synapses. Second, the algorithms of signal processing in chemical process control are applicable for modeling signal transduction pathways at synaptic compartments. Lastly, from the perspective of system engineering, complex physiological reaction pathways can be viewed as hierarchical systems consisting of subsystems each of which is solvable. In return, the insight gained from studying neurological systems can potentially stimulate the development of new paradigms in process control.

Process control systems intend to stabilize the operational conditions while nerve systems strive to homeostasis in body. Since uncertainty exists everywhere, these two systems manage to execute their own algorithm under noise. By comparison, the neuronal networks are more adaptive to process controllers. The adaptability arises because nerve systems implement long-lasting change of state variables after memorizing and analyzing historical data. The capability of memory storage is needed for the collection of past events. Perception or pattern recognition is crucial in analyzing the data collected. Adaptability is especially valuable for systems surrounded by environment of higher

uncertainty. In addition to the feedback and feedforward control, these are a few other algorithms that can be added to the toolbox of modern control systems. For instance, neural networks can be potentially useful to establish models relating system inputs and outputs. Yet there are intrinsic drawbacks with the current neural networks most of which are related to the oversimplification of the basic neuronal units. These problems can probably be overcome through biophysical modeling of neurons and neuronal connections.

1.2 Motivation

There are three different but related subjects that are addressed in this thesis. The common themes they share are the relevance to human memory and the research methodology we took. Yet the specific reasons for modeling each individual system are explained in the following sections.

1.2.1 Amyloid fibrillation: the pathology of memory loss

Alzheimer's disease (AD) is the most common cause of senile dementia and memory loss. There are currently (in the year 2008) about six million patients of AD here in the U.S and the number is rising dramatically as the population ages. Many neurodegenerative diseases including Alzheimer's and Parkinson's diseases are found to be related to amyloid fibril formation. Lots of experiments were done separately in different systems of amyloid proteins. Independent of the types of amyloid proteins, the responses of amyloid fibrillation appear similar, which is an indication of common underlying biophysical mechanism. Before the start of our theoretical work, there were few biophysical models able to well interpret experimental data of amyloid fibrillation *in vitro*. In the meantime, the kinetic process of how soluble amyloid proteins turn into insoluble amyloid fibrils was unclear. Therefore, a biophysical model considering key biomolecular species and reactions is required.

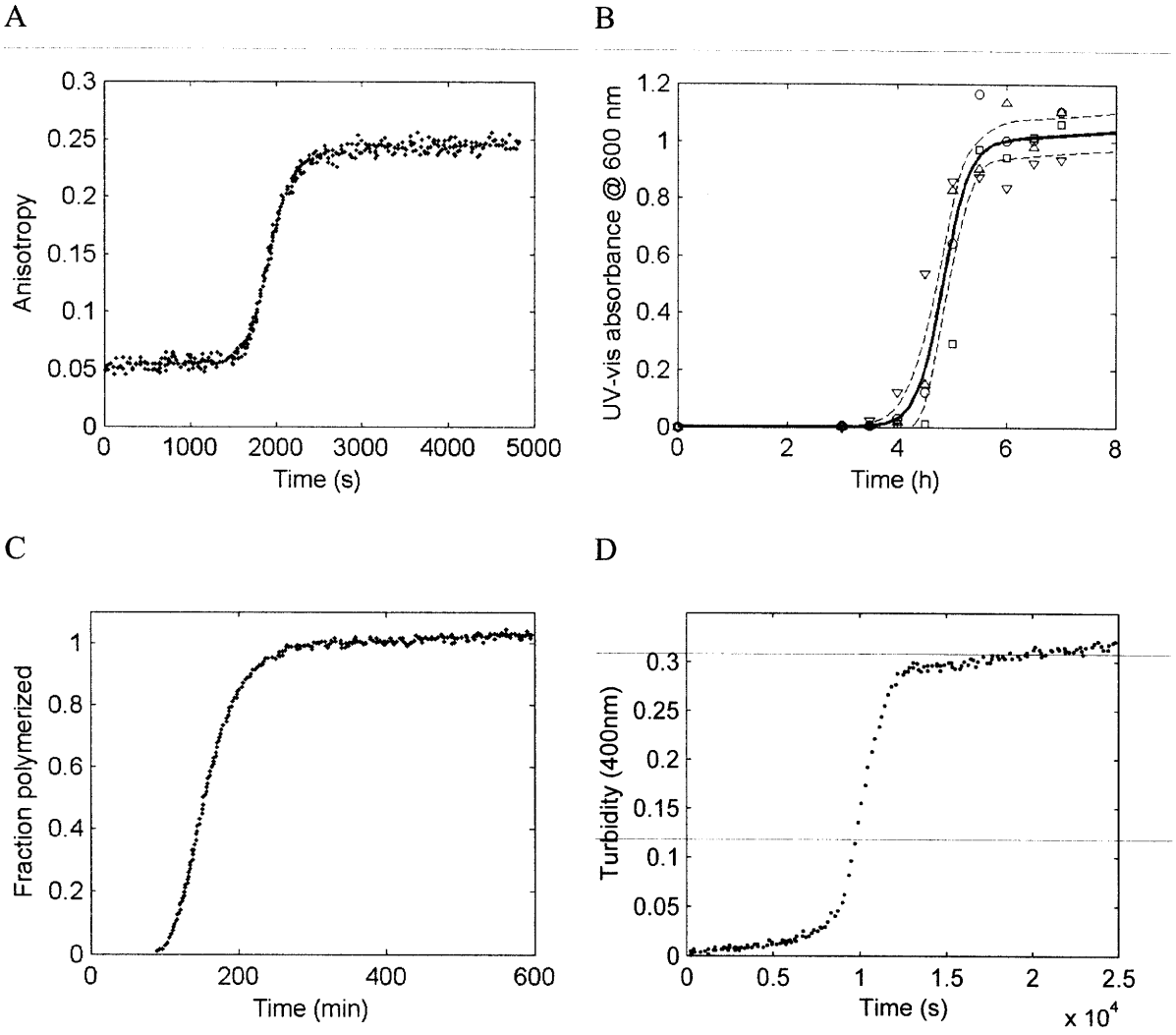

Figure 1-2 Amyloid fibrillation responses of different proteins or peptides.
(A) The fibrillation response of islet amyloid [122]. (B) The fibrillation response of insulin [90]. (C) The fibrillation response of prion [32]. (D) The fibrillation response of Aβ [45].

1.2.2 Synaptic plasticity: the mechanism of memory formation

Since the proposal of Hebb's rule in 1949 [65], synaptic plasticity has become the leading hypothesis of memory formation mechanisms at cellular level. Yet the hypothesis had not been validated until the experimental work of long term potentiation done by Bliss and Lømo in 1973 [20]. Synaptic plasticity is a crucial concept in relating microscopic neuronal connection to macroscopic perception. Experiments revealed that changes in probability of neurotransmitter release and in calcium-induced insertion or removal of postsynaptic receptors are the mechanisms of short-term and long-term plasticity, respectively [38, 91]. Yet few biophysical models have been developed to well quantify and integrate the dynamics of these reactions.

The learning rules by which synaptic plasticity varies with respect to external stimuli are critical to predict how connections between neurons evolve within neuronal network. In

addition to Hebb's rule, BCM rule developed by is physiologically more reasonable and demonstrates more sophisticated responses. The common and different attributes of these rules have significant impact on collective behaviors of interconnected neurons. Yet current understanding of how cognition and behavior can arise from groups of interconnected neurons is still at its infancy. Theoretical work and simulation need to be done to first understand the fundamental biophysics of synaptic plasticity and then to implement the biophysical models in neuronal network to check on the resultant collective behavior.

1.2.3 Spike timing dependent plasticity (STDP)

The spike timing dependent plasticity is a relatively new experimental protocol to elicit either long-term potentiation or depression. It has been intensively studied because of its relevance to associative learning and Hebb's rule. There are quite a lot of experimental data available and accordingly speculations regarding the key species and reactions which contribute to the phenomena. Yet few mechanistic models are capable of confirming them through successful fitting with single type of STDP, let alone models to integrate various kinds of STDP responses. A unifying model, if exists, is an indication of common biochemical reactions underlying different kinds of STDP responses. Such model is needed both for understanding the fundamental reaction pathways that lead to STDP. Also it is required for testing whether associative learning behavior arises after incorporation of physiology-based synaptic model into neural network.

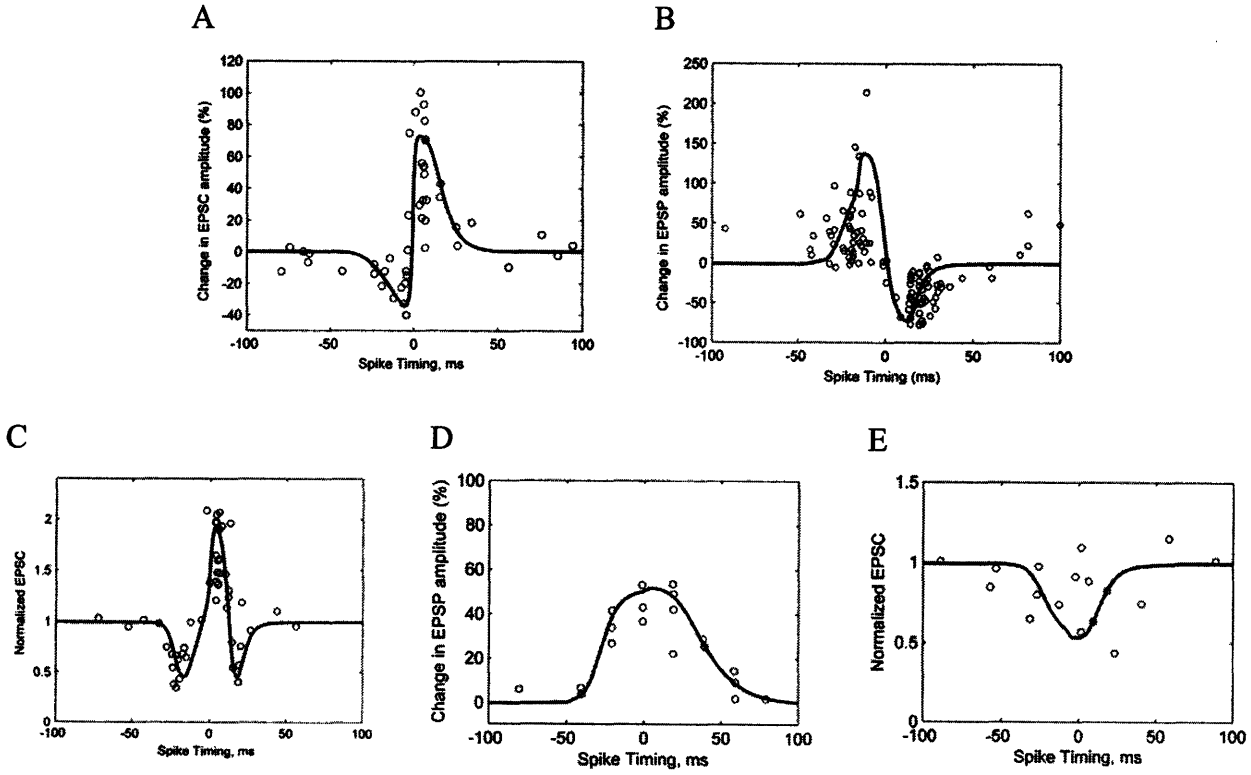

Figure 1-3 STDP responses of different synapses.
(A) Asymmetric STDP following Hebbian rule [16]. (B) Asymmetric STDP following anti-Hebbian rule [9]. (C) Symmetric STDP with mixed LTP and LTD [118]. (D) Symmetric STDP with only LTP [57]. (E) Symmetric STDP with only LTD [172].

1.3 Thesis objectives

Based on the motivation and background information given above regarding mechanisms of memory formation and causes of memory loss, the objectives of the thesis include the following points:

- To develop a kinetic model of amyloid fibrillation to explain the experimental measurements *in vitro*.
- Develop a unified model to explain responses of short term and long term plasticity.
- Integrate essential synaptic signal transduction pathways and propose a unified theory for spike timing dependent plasticity.

Corresponding to the objectives proposed, the main contributions of this thesis are:

- A three-stage kinetic model has been developed for elucidating the mechanisms of amyloid fibrillation *in vitro*.
- A unified model has been built for explaining both short-term facilitation and depression.
- A calcium entrapment model was proposed to fit long-term potentiation responses. Model discrimination work has also been done by using the graded experimental responses of long-term potentiation caused by multiple trains of stimulation. The results demonstrate better performance of the calcium entrapment model than that of the bistable model.
- A NMDA receptor model coupled with calcium dependent plasticity has been developed to well explain various kinds of spike timing dependent plasticity.
- The relationship between calcium signaling and amyloid fibrillation has been hypothesized. Future work is also suggested to confirm how the accumulation of amyloid plaques may disrupt the balance of calcium and disable long-term potentiation.

1.4 Thesis outline

The thesis is organized according to the diagram in Figure 1-4.

First of all, Chapter 1 provides the motivations behind studying the memory formation mechanism and memory loss pathology. It also summarizes the objectives and main contributions of the thesis.

Chapter 2 covers the general methodology we take for modeling biological systems. It covers the procedure for setting up reaction schemes, converting them into ordinary differential equations accordingly as well as linear and nonlinear parameter estimation, etc.

Chapter 3 gives the background information regarding amyloid fibrillation and reviews the modeling work that has been done in this area. Afterwards, our model showing better agreement with experimental data of fibrillation is presented.

Chapter 4 and 5 deal with short-term and long-term synaptic plasticity, respectively. The mechanism for short-term plasticity agrees with the literature while that for long-term plasticity is still controversial. Model discrimination is done to determine the more reasonable model compared to experimental data.

Chapter 6 includes the previous experimental work of spike timing dependent plasticity (STDP) as well as our modeling work to elucidate its underlying mechanisms. A unified model was developed for explaining quite a variety of experimental data belonging to different types of STDP.

Chapter 7 integrates the findings from amyloid fibrillation model and synaptic plasticity model. We summarize the hypotheses for causes of memory loss and suggest possible interactions between calcium signaling and amyloid fibrillation.

Finally, Chapter 8 and Chapter 9 discuss the direction of future work and conclusion, respectively.

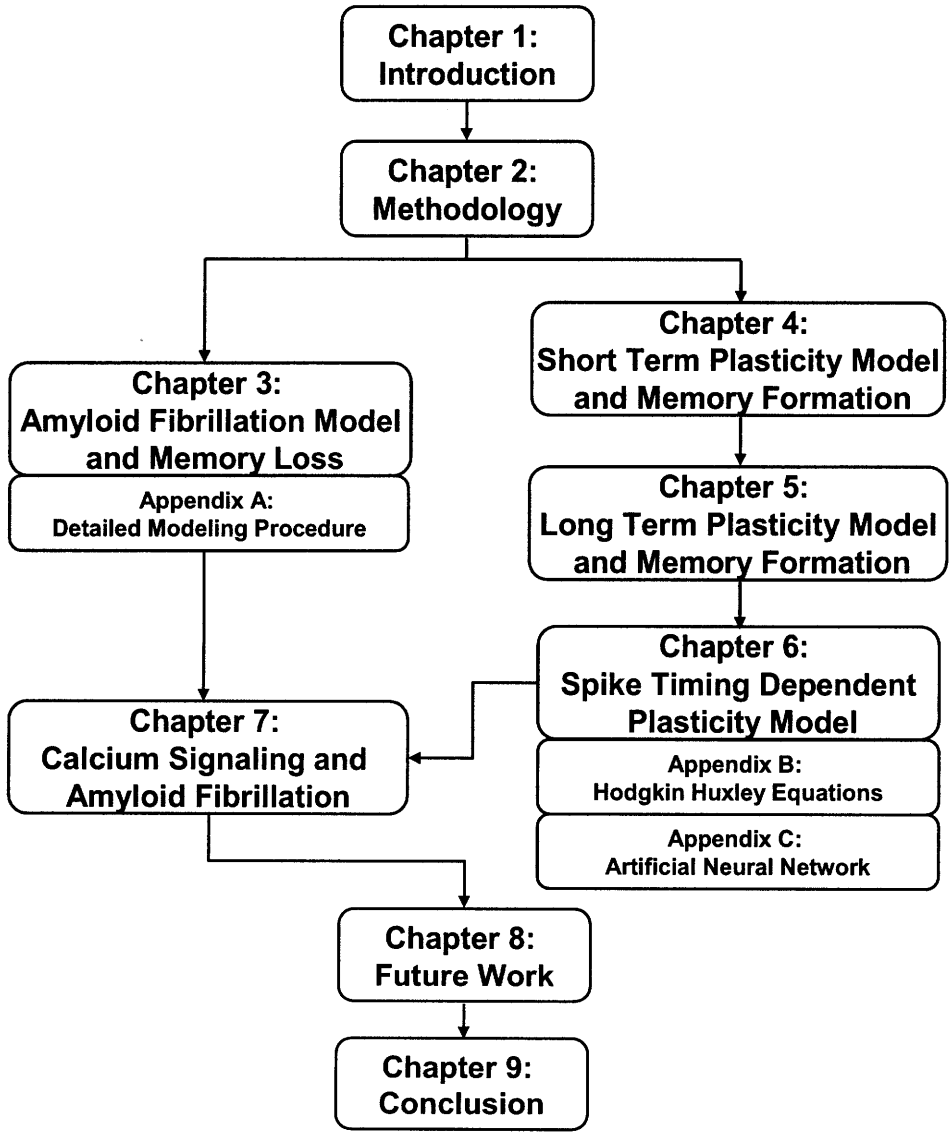

Figure 1-4 The organization diagram of chapters in the thesis.

2 Methodology of Model Development

Mathematical models have been developed to explain biological phenomena for centuries. Most classical interest areas modeled by continuous equations are related to population dynamics [42]. For instance, predator-prey models were proposed based on population balance to predict the species population in ecology. Similar ideas were further applied to describe the dynamic relationship between patients and carriers to estimate the outburst of infectious diseases in epidemiology. It was after the development of Michaelis-Menten equations that mathematical models begin to be widely applied to microscopic biological system. As a breakthrough in enzymology, Michaelis-Menten kinetic model precisely described enzyme-substrate interaction and successfully matched the enzymatic experimental data [110]. It is still commonly used today to describe enzymatic reactions and other biological reactions at a molecular level [14].

Molecular scale biological sciences involve studies of complex living systems with difficulty in measuring arrays of interacting species. The sizes of most biomolecules are smaller than the resolution of common microscopes. Electrophysiological procedure measuring the signal response of neuronal tissues requires multi-step treatment and instrumentation before experiment. Also quantification of common molecules depend on complicated assays usually involve multiple experimental steps such as cell culturing, purification, and staining. Thus, mathematical modeling provides valuable theoretical hypothesis to guide the experimental study and maximize the value of each experiment. Successful examples include theoretical models to explain molecular events such as signal transduction, neuronal spiking, and gene expression, etc. It is through systematic modeling that the hierarchical structure and subsystem interactions in biological systems can be unraveled and understood.

2.1 Recognize biological systems of interest

The methodology listed here is applicable to different kinds of biological systems. Yet the systems of interest in this thesis are related to memory pathology and memory formation mechanisms. The most serious causes of senile dementia and memory loss are Alzheimer's disease and Parkinson's disease both of which are found to be related to amyloid fibril formation.

2.2 Propose biochemical reaction mechanisms

Depending of the types of systems being studied, the biochemical reactions involved differ. Yet the chances are that for most biological systems having been studies previously, some relevant reaction pathways can be recognized. By cross referencing literature, doing experiments, or drawing influence diagram, it is possible to propose the principal reaction mechanisms.

It is likely that the biological system of interests involve a number of subsystems. The boundaries of different subsystems and hierarchical structure need to be well defined. Ideally each of the subsystem should be individually analyzed to ensure the validity or the proposed model and the robustness of the overall system.

2.3 Convert reactions into differential equations

Material balance and reaction kinetics are the two principal guidelines in converting chemical reactions into differential equations. The variables involved can be classified into input variables, state variables, and response variables. The response variable can take the form of algebraic equation:

$$\bar{Y} = \bar{F}(\bar{X}, \bar{\theta}) \tag{1.1}$$

It can also be expressed as ordinary differential equations:

$$\frac{d\bar{X}}{dt} = \bar{f}(\bar{X}, \bar{\theta}) \tag{1.2}$$

The number of sate variables has to be equal to the number of independent differential equations. In addition, the initial conditions of all the state variables need to be specified.

$$@t = 0 \qquad \bar{X} = \bar{X}_{initial} \tag{1.3}$$

2.4 Least square parameter estimation

There are usually parameters embedded in the model such as reaction rate constants, physical or chemical properties, etc. Parameter estimation is therefore necessary to determine the values of those parameters. Parameter estimation is more straightforward for linear models [136] but require iteration processes for nonlinear ones [137].

2.4.1 Linear least square regression (LLSR)

Least squared errors are usually adopted for estimating parameters. Other methods include maximum likelihood estimation, Bayesian estimator, etc. For linear models, the minimization of sum of squared errors only involves solving sets of linear equations.

$$\bar{Y} = X\bar{\beta} + \bar{\varepsilon} \tag{1.4}$$

Or the expanded version assuming there are n experimental data points and p parameters:

$$\begin{bmatrix} y_1 \\ y_2 \\ \vdots \\ y_n \end{bmatrix} = \begin{bmatrix} 1 & x_{12} & x_{13} & \cdots & x_{1p} \\ 1 & x_{22} & x_{23} & \cdots & x_{2p} \\ \vdots & \vdots & \vdots & \ddots & \vdots \\ 1 & x_{n2} & x_{n3} & \cdots & x_{np} \end{bmatrix} \begin{bmatrix} \beta_1 \\ \beta_2 \\ \vdots \\ \beta_p \end{bmatrix} + \begin{bmatrix} \varepsilon_1 \\ \varepsilon_2 \\ \vdots \\ \varepsilon_n \end{bmatrix} \tag{1.5}$$

The prerequisite conditions for using linear least square regression are called Gauss-Markov assumptions which are listed below.

- The random error terms have expected value of zero
- The random error terms are uncorrelated
- The random error terms have the same variance

That is, the distribution of error can be written as: $\varepsilon \sim N_n(0, \sigma^2 I_n)$

One of the tasks included in linear least square regression is to find the best estimate of parameter vector $\hat{\beta}$. The geometric analysis shown in Fig helps visualize the algorithms while algebraic argument can also be done to reach the same results. The objective is to minimize the sum of squared errors ($\varepsilon^T\varepsilon$) with respect to vector β. The projection of vector β onto Ω, the column space of matrix X, is called θ. That is, $\theta = X\beta$. Now the sum of squared error becomes the square of the length of error vector Y- θ since $\varepsilon^T\varepsilon = (Y-\theta)^T(Y-\theta) = \| Y-\theta \|^2$. If we let θ vary in Ω, the optimal $\hat{\theta}$ would be the one that makes (Y- θ) perpendicular to surface Ω, according to Fig. Therefore $X^T(Y-\hat{\theta}) = 0$ which is the same as the following equation:

$$X^T\hat{\theta} = X^TY \tag{1.6}$$

Once the optimal vector $\hat{\theta}$ on space Ω is found, it can be converted back to vector $\hat{\beta}$ given the columns of matrix X are linearly independent. This becomes the normal equations of linear least square regression.

$$X^TX\hat{\beta} = X^TY \tag{1.7}$$

The best estimate of parameter vector $\hat{\beta}$ can now be found by simply multiplying the reverse matrix of (X^TX) to both sides of the normal equations.

$$\hat{\beta} = \left(X^TX\right)^{-1}X^TY \tag{1.8}$$

Then the error terms can be calculated by taking the difference between experimental data and predicted values:

$$\varepsilon = Y - \hat{Y} = Y - X\hat{\beta} \tag{1.9}$$

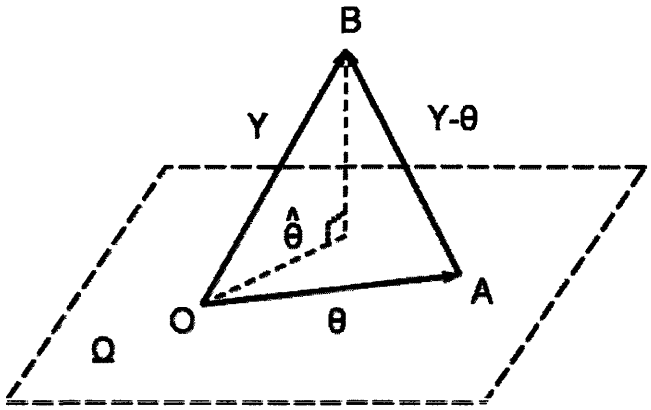

Figure 2-1 The geometrical scheme used to find the optimal vector that minimizes the sum of squared errors (SSE).

Under Gauss-Markov assumption, the measurement vector Y follows the n×n normal distribution: $Y \sim N_n(X\beta, \sigma^2 I_n)$. As a result, the distribution of estimated parameter vector $\hat{\beta}$ follows $\hat{\beta} \sim N_p(\beta, \sigma^2 (X^T X)^{-1})$ and normalized sum of squared errors follows χ^2 distribution: $SSE / \sigma^2 \sim \chi^2_{n-p}$ where S^2 is the unbiased estimator of σ^2:

$$S^2 = \frac{SSE}{n-p} = \frac{(Y - X\hat{\beta})^T (Y - X\hat{\beta})}{n-p} \tag{1.10}$$

Finally, the 100(1- α)% confidence interval of parameter β_i can be computed using the following equation where t stands for t-distribution with n-p degrees of freedom at the α level of significance. The proofs in details can be found in Seber and Lee, 2003 [136].

$$\hat{\beta}_i \pm t_{\alpha/2, n-p} S \sqrt{(X^T X)^{-1}_{ii}} \tag{1.11}$$

2.4.2 Nonlinear least square regression (NLSR)

The least square regression for nonlinear model does not have straightforward formula just as linear regression does. Instead solving NLSR problems requires optimization algorithms. The general form of nonlinear model can be expressed as the following:

$$y_i = f(x_i; \overline{\theta}) + \varepsilon_i \quad (i = 1, 2, ..., n) \tag{1.12}$$

The sum of squared errors is the sum of the squared differences between experimental data and the model.

$$S(\bar{\theta}) = \sum_{i=1}^{n} \left[y_i - f(x_i; \bar{\theta}) \right]^2 \tag{1.13}$$

In order to find the minimum of the sum of squared errors, we need to differentiate $f(x_i; \bar{\theta})$ with each parameter θ_r for r from 1 to p.

$$\left. \frac{\partial S(\theta)}{\partial \theta_r} \right|_{\hat{\theta}} = 0 \quad (r = 1, 2, ..., p) \tag{1.14}$$

If we denote $f_i(\bar{\theta}) = f(x_i; \bar{\theta})$, we can use the define F(θ) as the design matrix for nonlinear model:

$$F(\bar{\theta}) = \left[\left(\frac{\partial f_i(\bar{\theta})}{\partial \theta_j} \right) \right] \tag{1.15}$$

Then Eq. (1.14) can be rewritten as:

$$\sum_i \left\{ y_i - f_i(\bar{\theta}) \right\} \left. \frac{\partial f_i(\bar{\theta})}{\partial \theta_r} \right|_{\theta = \hat{\theta}} = 0 \tag{1.16}$$

or

$$0 = \hat{F}^T \left\{ y - f(\hat{\theta}) \right\} = \hat{F}^T \hat{\varepsilon} \tag{1.17}$$

The geometrical meaning of Eqs. (1.17) is that the optimal error vector should be perpendicular to the column space of design matrix F. Therefore, they are called normal equations for nonlinear model. The subsequent algorithms for parameter estimation and model prediction become similar to those of linear least square regression.

2.5 Summary chart of model development method

The standard procedure of model development is illustrated in Figure 1-4. Once the system of interest has been identified, the next step in divided into two pathways: the performance of experiments and development of theoretical models. Eventually the model outputs the results of goodness-of-fit, parameter estimation, and model prediction. Yet experiments and models should not be independent of one another. Instead, it is through the interaction between these two that the mechanisms underlying specific biological phenomena can be unraveled efficiently. For instance, model-based experimental design potentially lowers the number of experiments and increases the accuracy of measurements [11]. That is, more information can be extracted from one single set of experiment.

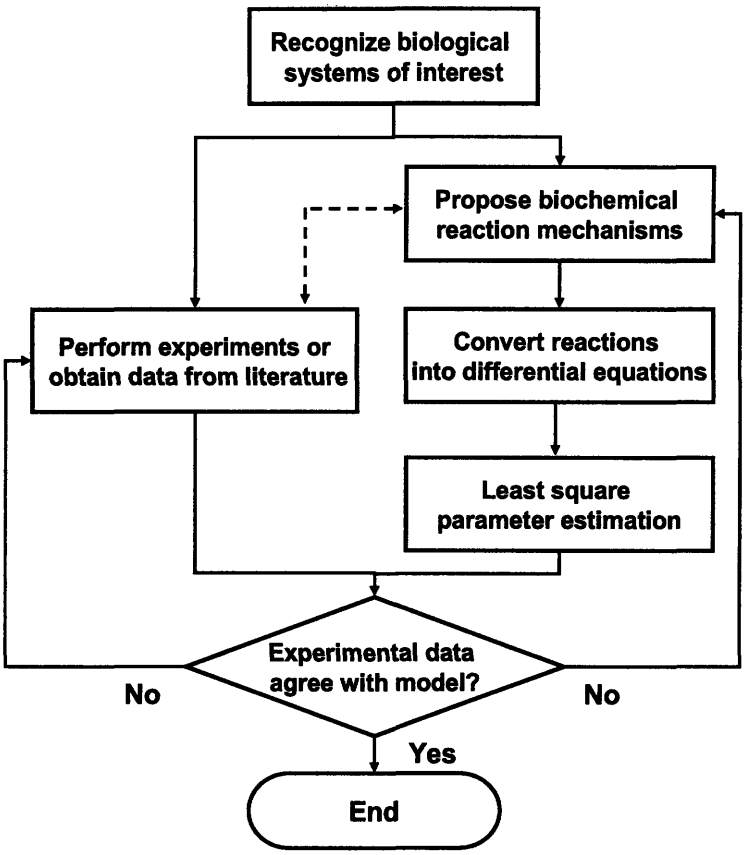

Figure 2-2 The summary chart of model development process. The model is developed together with execution of experiments.

Lastly, one essential statistical concept is worth clarifying. The agreement between the experimental data and model is the necessary but not sufficient condition to confirm the validity of the model. That is, the satisfactory goodness-of-fit between one set of data and the model means the specific data cannot reject the proposed model. Yet it does not exclude the possibility that alternative models can explain the same set of data equally well or the possibility that other sets of data can refute the model. Therefore, cautions need to be taken when asserting the validity of the model. That is, models that have only been tested against certain sets of data are not universally true; instead, each model usually has its own limitations.

3 Modeling Amyloid Fibrillation

Amyloid fibrillation has been intensively studied because of its association with various neurological disorders. While extensive time-dependent fibrillation experimental data are available and appear similar, few mechanistic models have been developed to unify those results. The aim of this work was to interpret these experimental results via a rigorous mathematical model that incorporates the physical chemistry of nucleation and fibril growth dynamics. A three-stage mechanism consisting of protein misfolding, nucleation, and fibril elongation is proposed and supported by the features of homogeneous fibrillation responses. Estimated by nonlinear least squares algorithms, the rate constants for nucleation were about ten million times smaller than those for fibril growth. These results, coupled with the positive feedback characteristics of the elongation process, account for the typical sigmoidal behavior during fibrillation. In addition, experiments with different proteins, various initial concentrations, seeding versus non-seeding, and several agitation rates were analyzed with respect to fibrillation using our new model. The wide applicability of the model confirms that fibrillation kinetics may be fairly similar among amyloid proteins and for different environmental factors. Recommendations on further experiments and on the possible use of molecular simulations to determine the desired properties of potential fibrillation inhibitors are offered.

3.1 Introduction of amyloid fibrillation

Amyloid fibrillation is the process of native soluble proteins misfolding into insoluble fibrils comprising cross-β-sheets. More than 20 amyloidogenic diseases such as Alzheimer's disease, Parkinson's disease, and prion–associated encephalopathies have been found to share fibril formation as the a common symptom [146]. While the presence of amyloid plaques correlates with disease, whether fibrils themselves, misfolded oligomers, or other factors are the causal agents of diseases remains unclear [19, 32, 89]. Although the proteins associated with each disease do not share sequence homology, they exhibit similar insoluble filaments and fibrillation responses [81, 141]. This suggests that the underlying fibril formation mechanisms may be common [9].

The typical fibril formation process starts with a lag phase in which the amount of amyloid proteins turned into of fibrils is not significant enough to be detected. Afterwards, a drastic elongation phase follows and fibril concentration increases rapidly [122]. Eventually, the process reaches equilibrium when most soluble proteins are converted into fibrils. The length of lag times and fibril growth rates depend upon factors like the initial concentration and pH, both of which affect the degree of super-saturation in solution. The presence of seeded molecules and foreign surfaces can influence the kinetics of fibrillation, because of the ability to catalyze the reactions at these interfaces [148]. Other factors include the ionic strength of the solution and the intensity of agitation [117]. Although experimental data covering these many different conditions have been reported in the literature, there is a noticeable lack of quantitative mechanistic models to provide insight into the process and directions for further research.

Because of the commonly observed sigmoidal-shaped fibrillation response reported in the literature [45, 117], fibrillation processes have been modeled as a number of reactions in series covering the assembly of oligomers, the formation of nuclei as well as the growth and the breakage of fibrils [32, 47, 100]. Moreover, the two-stage mechanism of yeast prion fibrillation, in which fibrils act as enzymes to trigger nucleated conformational conversion by Michaelis-Menten kinetics, provides another valuable perspective [132]. Empirical or semi-empirical exponential functions are popular choices to fit the data since they are computationally simple and match the observed data well [117, 125]. While suggestive, some of these models only depicted the sigmoidal trend without rigorous quantitative arguments; others have not provided details on how the nuclei form or explained the shortened lag-time resulting from seeding and an increase in the initial protein concentration.

The lag-time prior to fibril growth has been noted in numerous publications and resembles an incubation period [45, 117]. Explaining its existence is one of the key scientific challenges. The problem was approached by Shoghi-Jadid et al. [143] with introduction of the Heaviside function to force the separation of nucleation and fibrillation processes, while Uversky et al [117] used an empirical exponential model with adjustable parameters. We suggest that nucleation theory and growth models could be valuable in describing the fibrillation process. Furthermore, the drastic rate increase in the fibrillar growth phase after the lag phase indicates that cooperativity or positive feedback mechanisms are involved.

Another critical but missing piece of information is the relationship between the observable response and the degree of fibrillation. Even though histological dyes like thioflavin T (ThT) and Congo Red have been the commonly used as indicators of the presence of amyloid fibrils, the relationship between fluorescence intensity and amount of amyloid fibril remain unclear [96, 97]. There are also physical property methods for measuring fibril formation like turbidity, absorbance and sedimentation [45, 142]. Here, we assumed linearity between ThT fluorescence and fibril concentrations based on Beer-Lambert law as a measure of fibril content, and use ultraviolet-visible (UV-vis) absorbance at 280 nm as a quantitative measure of dissolved total protein.

Insulin (51 aa; 6 kDa) was chosen as the model protein for the measurements in this study because it (i) is a well-studied fibril-forming protein and has recently been studied in our laboratory [90], (ii) has been crystallized in the native state at high resolution, (iii) is known to develop structurally similar cross-β-sheet plaques to those formed by other amyloids, and is deposited in arterial walls of type II diabetes patients [167], and (iv) is available in large quantities at reasonable price. Native insulin is well-folded and in stable hexamer state associated with Zn^{2+} molecule under physiological conditions. Yet it can be readily unfolded to form fibrils in solution by both increasing the temperature to 65^0C and by reducing the pH to 1.6. Jiménez et al. proposed that the α-helical structure (58%) of native insulin becomes unfolded to expose the β-sheet region (6%) which is the major component of the amyloid cross-β ribbon [75].

In the next section, we describe the proposed kinetic model for insulin fibrillation including the parameter estimation procedure. Since experimental protocols and responses of fibrillation are similar among amyloid proteins, the modeling approach presented here is also applicable to the fibrillation of other proteins. Afterwards, our model is compared

with an empirical fitting function. A general description of the Experimental Materials and Methods follows. Then, in the Results and Discussion section, the new model is fitted to our insulin fibrillation data, to fibrillation of Aβ-40 and prion-like NM fragment of Sup-35 [45, 87], and to data conducted under various conditions (i.e. increasing initial insulin concentration, effect of seeding, stirring effects).

3.1.1 A kinetic model for insulin fibrillation

Three standard analytical steps were chosen to model insulin fibrillation: formulation of the appropriate kinetic reactions based on the polymerization and nucleation theories, conversions of the reaction set into a system of differential equations, and parameter estimation by nonlinear least square algorithms to optimize the fit between simulation results and the experimental measurements.

Initially four species of insulin were considered during fibrillation: original hexamer, monomer, cluster, and fibril [123, 142]. While the original hexamer is composed of six monomers stabilized by Zn^{2+}, an insulin monomer refers to two chains of polypeptides connected with disulfide bonds (the A- and B-chains comprising 21 and 30 amino acids, respectively). For systems other than insulin, different morphologies may be involved such as those for β_2-microglobulin [56]. By incorporating the four insulin species into the reaction scheme, the proposed kinetic mechanism for this study consists of three distinct stages: decomposition of hexamers, nucleation process, and fibrillation stage as summarized in
Figure 3-1 and Table 3-1. All the reactions listed are elementary reactions so the fluxes can be easily expressed as the products of reactant concentrations and the rate constant. Regarding notations, A_{hex} and A_i denote the concentration of original insulin hexamers and oligomers containing i monomers, respectively. All fibrils are abbreviated as F, regardless of their length. Even though physical reactions contributing to larger-size cluster formation and the entanglement between strands of fibrils have been reported [75, 104], the actual active chemical reaction sites are assumed to be restricted to the fibril ends [142]. Therefore, fibrils of different sizes can be considered as the same species.

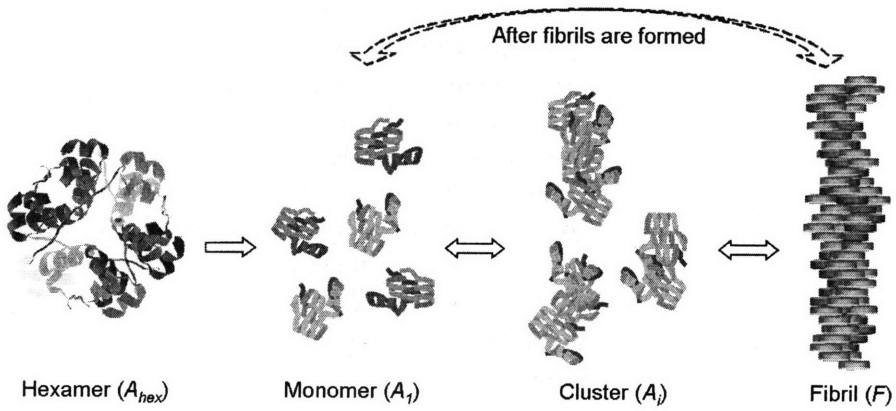

Figure 3-1 The key species in the proposed three stage reaction mechanism of insulin. The images of the hexamer and fibril were redrawn based on the literature [54, 75].

Key reaction species interact with one another and reactions proceed as summarized in Table 3-1. A nomenclature table that summarizes the meanings of symbols is attached at the end (Table 3-4). First, the zinc-stabilized hexamers are assumed to irreversibly misfold and dissociate into monomers containing cross β-sheets under stringent conditions like low pH and high temperature [121]. Since the dissociated form of insulin has been reported to readily misfold into reactive monomers [75], the misfolding step is assumed to occur very fast. In this case, the dissociation step is rate limiting with the rate constant k_d. Second, the mechanism of nucleation is based on the Becker-Döring nucleation model from the field of atmospheric science [138]. Accordingly the newly formed monomers react with one another as well as with different size oligomers so as to become larger clusters. The reactions between larger oligomers are negligible because their early concentrations and diffusivities are relatively low and small, respectively, as compared with the monomers. As oligomers grow, their chemical potentials drop, yet the surface tension to form new phases rises. Hence, there should exist a condition with minimum Gibbs free energy corresponding to the size of a cluster (or nuclei), *(n–1)*-mer [138]. Any aggregates larger than the cluster would convert into fibrils. Once the fibrils are formed, their ends serve as nuclei and undergo self catalytic reactions to become longer fibrils with $k_{fb,i}$ and $k_{fb,-i}$ as the forward and reverse rate constants [60]. At this stage, reactions between fibrils and all sizes of oligomers need to be taken into account since the reactive nature of fibril ends greatly accelerates the process. Finally, the reactions of *i*-mer addition and detachment proceed until the clusters are depleted and reach equilibrium with fibrils.

After the kinetic schemes are established, the concentrations of various species are expressed as functions of time. The temporal change of these species can be derived from material balances and reaction kinetics. The first specie to be considered is the original insulin hexamer whose rate of change is expressed as the disappearance by dissociation (Eq. (3.1)).

$$\frac{dA_{hex}}{dt} = -J_d \tag{3.1}$$

The rate of monomer concentration change can be calculated by taking into account all the reactions involving monomers in Table 3-1. As a result, the time derivative of A_1 equals the generation rate from the hexamer dissociation reaction minus the consumption rate due to all nucleation reactions, and the first elongation reaction (Eq. (3.2)). The constants before J_d and $J_{nu,1}$ are the stoichiometric coefficients.

$$\frac{dA_1}{dt} = 6J_d - 2J_{nu,1} - \sum_{i=2}^{n-1} J_{nu,i} - J_{fb,1} \tag{3.2}$$

Then the concentration change of *i*-mer clusters is equal to its formation rate from the (*i–1*)-th nucleation reaction minus the consumption rate due to the *i*-th nucleation reaction and the *i*-th elongation reaction (Eq. (3.3)).

$$\frac{dA_i}{dt} = J_{nu,(i-1)} - J_{nu,i} - J_{fb,i} \qquad for \;\; i = 2,3,...,n-1 \tag{3.3}$$

The addition of monomer to the largest possible cluster (A_{n-1}) results into fibril formation as the last reaction at the nucleation stage suggests. Hence, the time derivative of fibril concentration is equal to the fibril generation rate subtracted by its consumption rate, i.e., the net flux of last nucleation reaction (Eq. (3.4)). Note that the fibril elongation process actually does not affect fibril concentration since no additional fibrils are formed or consumed at that stage.

$$\frac{dF}{dt} = k_{nu,(n-1)} A_1 A_{n-1} - k_{nu,-(n-1)} F \tag{3.4}$$

The initial concentration of insulin hexamers is equal to the amount of insulin added initially and is the main driving force for the downstream reactions (i.e., $A_{hex}=A_{hex0}$). The concentrations of the other species are assumed to be zero at the start (i.e., $A_i=0$, $F=0$). Eqs. (3.1)-(3.4) contain totally $n+1$ variables with equal number of corresponding differential equations and initial conditions. Thus, the system of differential equations is properly defined and ready to be solved once the values of all parameters are specified.

Even though the model contains quite a few parameters, some of them are physically related to one another; others can be found from the literature. Three assumptions were made to reduce the total number of parameters.

1. The value of n, the critical number of monomers needed to form a nucleus, has been reported as six [143], so initially we have set n equal to six. However, we also discuss the sensitivity of this parameter on the model fit in the section "*In vitro* fibrillation kinetics". The dissociation rate constant of insulin k_d can be estimated from the insulin dissociation time of about one hour [62]. Assuming that one hour is approximately the time to reach 95% conversion of exponential decay, k_d is ~3 h^{-1}.

2. Since agitation has been found to drastically shorten the delay time [148], the reaction rates of forward nucleation and fibrillation ($k_{nu,i}$ and $k_{fb,i}$) are assumed to be diffusion limited [142]. Apparent rate constants of diffusion controlled reactions take the form of Eq. (3.5) [48], in which $\tilde{N}$ is Avogadro's number, d_{AF} is the mean free path of the complex molecule, and D_A+D_F is the sum of diffusivities of the reactants. The values of diffusivities are proportional to the inverse of the characteristic length R_{Ai}, following Stokes-Eistein equation as in Eq. (3.6) [18]. The volume of i-mer is equal to i times the volume of the monomer (V_1) and is also related to its own characteristic radius (R_{Ai}) through volumetric formula. Thus, the diffusivity is roughly proportional to the inverted cubic root of i, which equals the size of the cluster.

$$k_D = \tilde{N} 4\pi (D_A + D_F) d_{AF} \tag{3.5}$$

$$D_{A_i} \propto \frac{1}{R_{A_i}} = \frac{1}{\sqrt[3]{\frac{3}{4\pi} i V_1}} \propto \frac{1}{\sqrt[3]{i}} \tag{3.6}$$

In Eqs. (3.5) & (3.6), nucleation and fibrillation forward rate constants regarding different sizes of oligomer can be approximated by Eq. (3.7) and Eq.(3.8). Because the

sizes of oligomers are comparable and thus their diffusivities are similar, both diffusivities need to be taken into account in the nucleation process. On the other hand, in the case of fibrillation, since the sizes of fibrils are much larger than those of oligomers, D_F is negligible compared to D_{Ai} and therefore, the diffusivity of the oligomer is the dominant term.

$$k_{nu,i} = \frac{1}{2} k_{nu,1} (1 + \frac{1}{\sqrt[3]{i}}) \propto 4\pi (D_{A_i} + D_{A_1}) \tag{3.7}$$

$$k_{fb,i} \approx k_{fb,1} \frac{1}{\sqrt[3]{i}} \propto 4\pi D_{A_i} \tag{3.8}$$

3. The values of $k_{nu,-i}$ and $k_{fb,-i}$ are assumed to be independent of size i, and are abbreviated as k_{nu-} and k_{fb-} respectively. Serio et al. showed that sonicated seeding provided a larger amount of fibril ends as reactive sites and demonstrated higher reaction rate [142]. This suggested that under normal condition, the detachment of oligomers often occurs at the terminal rather than in the internal segment. Hence, for this study, the number of monomers within a chain or oligomer does not affect the reverse rate significantly.

3.1.2 Parameter estimation and model comparison

The predictions of Eqs.(3.1)-(3.4) were compared with the experimental data (i.e. values of the species concentrations) in order to estimate the rate constants. There were four kinds of observable data considered: ThT fluorescence, UV-Vis absorbance at 600 nm (A_{600}), turbidity, and dissolved insulin concentrations (absorbance at 280 nm, A_{280}). The first three measures were assumed to be roughly proportional to the insulin fibril concentrations by Beer-Lambert law [97], and denoted as $Y = b \cdot F$. The last measure was simulated by counting total number of i-mers in the unit of monomer concentration, which could be expressed as $Y = \Sigma_i A_i \cdot i$. Nonlinear least square regression was adopted to minimize the sum of squared errors between experimental data and those predicted by the model; parameter estimation procedures were carried out in Matlab®. Detailed algorithms are given in the Supplemental Materials [136].

Table 3-1. The proposed three-stage model including reaction fluxes and rate constants

Description of Processes	Reaction Schemes	Reaction Fluxes
Hexamer Decomposition	$A_{hex} \xrightarrow{k_d} 6A_1$	$J_d = k_d A_{hex}$
Nucleation Stage	$A_1 + A_1 \underset{k_{nu,-1}}{\overset{k_{nu,1}}{\rightleftarrows}} A_2$	$J_{nu,i} = k_{nu,i} A_1 A_i - k_{nu,-i} A_{i+1}$
	$A_1 + A_2 \underset{k_{nu,-2}}{\overset{k_{nu,2}}{\rightleftarrows}} A_3$	
	$A_1 + A_{n-2} \underset{k_{nu,-(n-2)}}{\overset{k_{nu,(n-2)}}{\rightleftarrows}} A_{n-1}$	
	$A_1 + A_{n-1} \underset{k_{nu,-(n-1)}}{\overset{k_{nu,(n-1)}}{\rightleftarrows}} F$	
Elongation Stage	$F + A_1 \underset{k_{fb,-1}}{\overset{k_{fb,1}}{\rightleftarrows}} F$	$J_{fb,i} = k_{fb,i} A_i F - k_{fb,-i} F$
	$F + A_2 \underset{k_{fb,-2}}{\overset{k_{fb,2}}{\rightleftarrows}} F$	
	$F + A_{n-1} \underset{k_{fb,-(n-1)}}{\overset{k_{fb,(n-1)}}{\rightleftarrows}} F$	

In the past, an empirical function like Eq. has been used in the literature to fit the fluorescent ThT data with time data [117]. Independent of the amyloid protein type, Eq. (3.9) fits the fibrillation data reasonable well. This again suggests that the fibril formation process is similar for these different proteins. It is a specialized form of the logistic function which has been frequently used in the field of population biology [83]. The parameters from this model include the apparent rate constant for the growth of fibril (k_{app}), and the lag time which are equal to $1/\tau$ and t_0–2τ, respectively.

$$Y = y_i + \frac{y_f}{1 + e^{-(t-t_0)/\tau}} \tag{3.9}$$

In the Supplemental Materials, it is shown how to relate the parameters in this empirical model to the kinetic rate constants in Eqs. (3.1)-(3.4) under simplifying assumptions. That is, when the critical size of a nucleus (n) is equal to 2, there is an analytical solution for the only two species, A_1 and F. By mass balance, $A_1 = A_0 - F \cdot N$ (where A_0 is initial concentration and N is the average fibril size). The time derivative for the fibril concentration can be reduced to a quadratic differential equation (Eq. (3.10)).

The two roots of the equation, r_1 and r_2, are obtained from the quadratic formula and correspond to the steady state fibril concentrations. Eq. (3.11) is the solution of Eq. (3.10) by integration. It expresses the temporal evolution of the fibril concentration, and has the equivalent functional form of Eq. (3.9). The observable delay lag and growth rates can be related to the kinetic constants by Eq. (3.12).

$$\frac{dF}{dt} = k_{nu,1}A_1^2 + k_{fb,1}FA_1 - k_{fb-}F \propto -(F - r_1)(F - r_2) \tag{3.10}$$

$$F = r_1 + \frac{r_2 - r_1}{1 + e^{-(t-t_0)/\tau}} \tag{3.11}$$

$$\frac{1}{\tau} = (Nk_{fb,1} - N^2 k_{nu,1})(r_2 - r_1) \quad and \quad t_0 = \tau \ln(-r_2 / r_1) \tag{3.12}$$

3.2 Experimental Procedures

All chemicals were obtained from Sigma Chemical Co. (St. Louis, MO). Recombinant human insulin was generously donated by Novo Nordisk A/B, Denmark. All insulin solutions used for the *in vitro* fibril formation experiments were freshly prepared prior to each experiment in 0.025 M HCl, 0.1 M NaCl and adjusted to pH 1.6. Each sample for the kinetic experiments contained 1 ml of 2 mg/ml insulin in glass vials and was incubated at 65°C. At appropriate time intervals, the sample was removed from the incubator for analysis.

UV-Vis absorbance assay: *In vitro* insulin fibril formation has been shown to result in the formation of insoluble aggregates which are β-sheet rich structures [117]. The UV-visible absorbance assay at 600 nm wavelength (A_{600}) has been extensively used to quantify insoluble aggregates like inclusion bodies and cell debris from cell culture and is also used frequently molecular biology studies. Here, we quantify the amount of insoluble protein (fibrils) and soluble protein by measuring the absorbance of the solutions at 600 nm and 280 nm, respectively. The absorbance was measured on a Hitachi U 2000 Double-Beam UV/VIS spectrophotometer (Hitachi Instruments Inc., Danbury, CT). Spin-x centrifuge tube filters (Corning Inc., NY) of 2 ml total volume with 0.22 μm pore size cellulose acetate membranes were used for separating the fibrils from the soluble protein. Centrifugation was conducted at 10,000g for 10 min to separate the fibrils from the supernatant. Then, the protein concentration in the supernatant was measured at 280 nm using a calibration curve.

3.3 Results and discussion

The model is first fitted to the data from our laboratory for the fibrillation of human recombinant insulin. We then tested the model with the experimental dataset from the literature, including fibrillation data of other proteins, at different initial concentrations, with and without seeding, and at different stirring rates. In addition, the kinetic rate

3.3.1 *In vitro* fibrillation kinetics

Two experimental assays were followed during the *in vitro* insulin fibrillation process. The UV-visible absorbance assay at 600 nm wavelength (A_{600}) was used to follow the formation of fibrils and A_{280} was used to track total protein after removing the fibrils with microfiltration. As seen in Figure 3-2A, the two sets of data closely followed each other with a sigmoidal and inverse sigmoidal curve. This result demonstrates that mass from the dissolved protein was used to form the fibrils and that the mass balance closed fairly well. To test the validity of the first assumption regarding n, the critical size of nucleus, the data in Figure 3-2A was fit with different values of n (results not shown). The R^2 value was the highest for n equal to six and dropped below 0.9 for n smaller than four or larger than nine. While nucleus sizes may take different values, statistically six was the least-squares estimator that minimized the sum of squared errors. Thus, the assumption of n~6 is reasonable for this study. Further experiments that measure fibril size distribution with time are clearly needed.

Since two independent measurements, A_{600}, and A_{280}, were used to follow the gain in fibrils and loss in protein with time, respectively, the model was first fit to each separate set of data and then to both sets of data simultaneously to obtain the values of the rate constants listed in Table 3-1 together with the goodness-of-fit estimates. First, the values of $k_{nu,1}$ are about 8 order of magnitude smaller than those of $k_{fb,1}$, which confirms the widely held view that the nucleation rate was rate limiting and that fibrillation was extremely fast. For fits of both sets simultaneously (combined), the rate constants were $k_{nu,1} = 3.74 \times 10^{-2}$ ($h^{-1}mM^{-1}$), $k_{nu-} = 1.01 \times 10^{-3}$ (h^{-1}), $k_{fb,1} = 2.75 \times 10^{6}$ ($h^{-1}mM^{-1}$), and $k_{fb-} = 1.84 \times 10^{3}$ (h^{-1}). This set of rate constants was then chosen for the sensitivity analysis reported in the Supplemental Materials to evaluate the impact of each parameter. Since several folds of change in k_{nu-} barely altered the fibrillation profile, k_{nu-} was not further considered for the parameter optimization (Supplemental Material Figure S1).

Thermodynamically, the rate constants are related to the Gibbs free energy of transition from the monomer to the nuclei, (*n–1*)-mer. By summing up all the reactions except the last one in the nucleation process in Table 3-1, we obtain Eq. (3.13) below. The standard Gibbs free energy can be calculated from equilibrium constants with Eq. (3.14) [138], where $\Delta G°$ denotes the free energy difference between monomers and (*n–1*)-mer clusters. The higher the ratio of the forward to the reverse rate constant, the more likely will the monomers convert to nuclei. Our calculated value of $\Delta G°$ is 42.6±12.2 kJ/mol, which is of the same order of magnitude as that reported for amyloid fibers, 33.4 kJ/mol [115]. Further, since the values of $k_{nu,i}$ are larger than k_{nu-}, the free energy should be negative and the nucleation process is spontaneous.

$$(n-1)A_1 \rightleftarrows A_{n-1} \tag{3.13}$$

$$\Delta G^{\circ} = -RT \ln K_c = -RT \ln \prod_{i=1}^{n-1} \frac{k_{nu,i}}{k_{nu-}} \tag{3.14}$$

The model is also able to track various insulin species such as initial hexamers, monomers, dimers, other oligomers and fibrils. It can be seen from Figure 3-2B&C that (i) all the initial zinc stabilized hexamer had disappeared by ~2 h, (ii) monomer reached a maximum at ~1 h and disappeared by 6 h, (iii) very little dimer was present, (iv) significant fibril formation occurred at about 3.5 h and saturated at ~5.5 h, and (v) formation and growth of trimers was faster than 4- and 5-mers and all three saturated at ~5.5 h. The experiment starts off with the rapid breaking down of original insulin hexamers, which gives rise to a drastic increase of monomer concentration. During the second stage (1-4 h), a quasi steady-state of cluster distribution appears and the oligomer concentrations rise slowly at the expense of disappearing monomers [10]. After the wave front reaches a certain critical condition, sufficient fibril ends are formed to serve as active sites for further elongation. The autocatalytic nature of the newly formed fibrils ignites the creation of clusters rapidly through a positive feedback loop until the monomers are depleted and oligomers reach their steady state concentrations. These simulation results clearly describe the sigmoidal curves shown in Figure 3-2A. for the formation and disappearance of fibrils and proteins, respectively.

Since sigmoidal behavior for most amyloidogenic proteins has been observed, this similarity in the response of many proteins suggests a common mechanism [80, 81, 132]. We decided to test our model with fibril formation data from the literature for several other such proteins. First, Sup35 is a yeast translation termination factor known to assemble in a prion-like form with its N and M segments governing prion formation [87]. Likewise, Aβ-40 is a protein fragment that aggregates into amyloid plaques and has been found in the brains of Alzheimer's disease patients [45]. However, for proteins other than insulin we needed to replace the hexamer dissociation step with a fast misfolding reaction. Shown in **Fig. 3** are the fibrillation data for a NM amyloid fragment of Sup35 at 2.5 μM and the Aβ-40 segment at 80 μM as well as the best fits (solid lines) [45, 87]. The coefficients of determination and kinetic rate parameters are listed in Table 3-2. The large R^2 values indicate the model fits the data well. For both NM and Aβ-40, the values of the nucleation rates ($k_{nu,1}$) are several orders of magnitude faster than those for insulin. This result is consistent with reports in the literature that indicate the ease of forming fibrils with NM and Aβ-40 [45, 87]. This demonstrates the flexibility of the model and suggests that the mechanism among amyloid proteins may be similar. More importantly, this model can potentially serve as the template for comparing and unifying data sets across different protein experiments carried out under various operational conditions such as changing initial concentrations, seeding and stirring. These effects are addressed next.

Table 3-2. Rate constants obtained by fitting the kinetic model to various experimental conditions (with ± one standard deviation)

Factors	Figure #	Exp. notes & Ref.	$k_{nu,1}$ ($h^{-1}mM^{-1}$)	$k_{fb,1}$ ($h^{-1}mM^{-1}$)	k_{fb-} (h^{-1})	R^2
Solution	Fig. 2A	Insulin, abs@600nm	$3.54 \pm 2.12 \times 10^{-2}$	$2.73 \pm 0.66 \times 10^{6}$	$1.93 \pm 1.87 \times 10^{3}$	0.94
		Insulin, conc.	$4.72 \pm 1.60 \times 10^{-2}$	$3.85 \pm 3.59 \times 10^{6}$	$1.30 \pm 0.66 \times 10^{3}$	0.98
		Insulin, combined	$3.74 \pm 1.13 \times 10^{-2}$	$2.75 \pm 0.48 \times 10^{6}$	$1.84 \pm 0.42 \times 10^{3}$	0.95
	Fig. 3	Prion [87]	$7.10 \pm 6.73 \times 10^{2}$	$1.51 \pm 1.22 \times 10^{4}$	$1.26 \pm 2.04 \times 10^{-1}$	0.99
		Aβ1-40 [45]	$1.38 \pm 0.53 \times 10^{0}$	$1.37 \pm 0.89 \times 10^{6}$	$3.02 \pm 2.64 \times 10^{2}$	0.99
Initial conc	Fig. 4A	Insulin, all concs [117]	$3.20 \pm 0.42 \times 10^{-1}$	$4.50 \pm 0.50 \times 10^{5}$	$4.00 \pm 0.88 \times 10^{1}$	0.92
Seeding	Fig. 5	Insulin, 0 & 10% [70]	$7.90 \pm 1.40 \times 10^{-2}$	$1.52 \pm 4.17 \times 10^{6}$	$1.99 \pm 1.16 \times 10^{1}$	0.87
Stirring	Fig. 6	Insulin, 80 rpm [148]	$1.43 \pm 0.75 \times 10^{-1}$	$4.20 \pm 1.15 \times 10^{6}$	$7.14 \pm 2.47 \times 10^{0}$	0.99
		Insulin, 160 rpm [148]	$2.68 \pm 4.12 \times 10^{-1}$	$1.27 \pm 5.27 \times 10^{7}$	$5.19 \pm 3.60 \times 10^{1}$	0.99

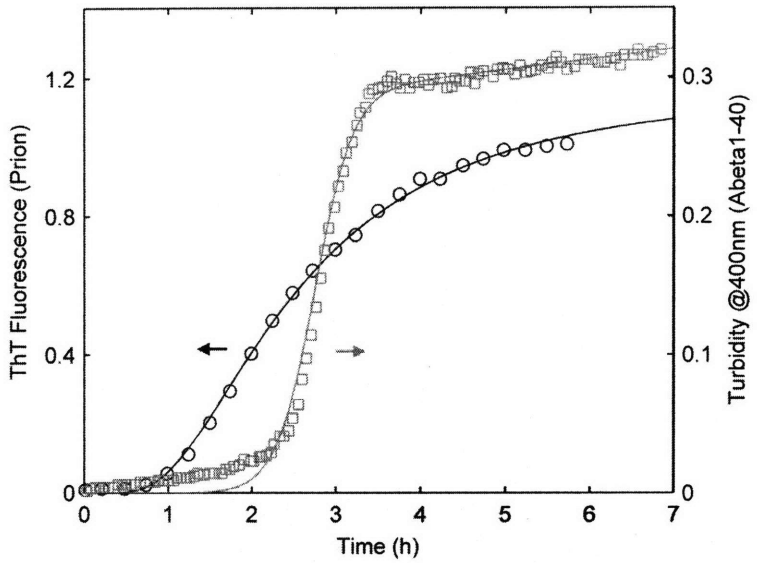

Figure 3-3 Fibrillation responses from other types of amyloid proteins.
The fibrillation responses for a 2.5 μM NM amyloid fragment of Sup35 from yeast monitored by ThT fluorescence (open circles). Data source: Krishnan et al. [87]. The fibrillation responses for 80 μM Aβ1-40 measured by turbidity assay (open squares). Data source: Evans et al. [45]. The solid lines are the optimal nonlinear least square fit.

3.3.2 *In vivo* fibrillation kinetics

Most of the in vitro fibrillation experiments only last for a few hours which is short compared to the disease progression of senile dementia. Modeling fibrillation *in vivo* is much more complex than that *in vitro* because of several practical reasons. First of all, there are potential interactions between fibrils and neurons. There are upstream reactions that lead to generation of amyloid monomers as well as down stream ones that decompose amyloid oligomers and fibrils. Also the transportation of biomolecules in living systems is hard to track and model. Second, the *in vivo* measurement itself is harder to perform as metabolism may interfere with chemical or immunoassaying. Therefore, the quality and quantity of the data are not as good as those *in vivo*. Finally, the physiological conditions *in vivo* are more difficult to control such as pH values, temperature, and ionic strength, etc.

Yet we adopted the same *in vitro* kinetic model of amyloid fibrillation for *in vivo* experimental data as a preliminary step toward full scale modeling. Cortical neurons of APP transgenic mice were observed by the multiphoton microscope which is a breakthrough technique for monitoring newly formed amyloid plaques. *In vivo* imaging of amyloid pathology was recorded after the addition of blue methoxy-XO4, the staining specific for amyloid deposition. As shown in Figure 3-4, the sizes of the plaques increased rapidly within the first day of experiment and stayed at about the same level afterwards. We used the same values of reaction rate constants yet changed the initial amyloid protein concentration. The initial concentration we used for this case was 0.7 mg/mL compared to the value 2 mg/mL we used for matching Figure 3-2. Granted that other physiological factors may affect the rate at which amyloid proteins fibrillate, the time it took for significant amount of fibrils to form is roughly inversely proportional to the initial concentration of amyloid proteins. The following section discusses the concentration effects in details.

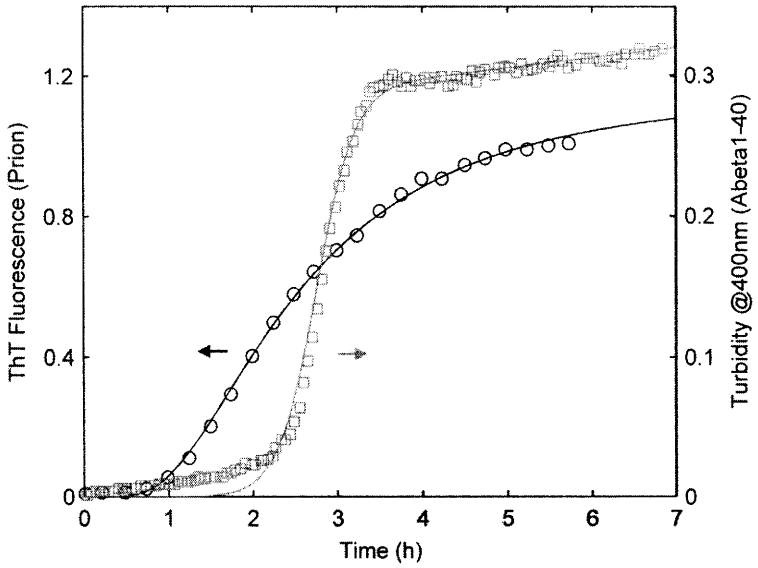

Figure 3-3 Fibrillation responses from other types of amyloid proteins.
The fibrillation responses for a 2.5 μM NM amyloid fragment of Sup35 from yeast monitored by ThT fluorescence (open circles). Data source: Krishnan et al. [87]. The fibrillation responses for 80 μM Aβ1-40 measured by turbidity assay (open squares). Data source: Evans et al. [45]. The solid lines are the optimal nonlinear least square fit.

3.3.2 *In vivo* fibrillation kinetics

Most of the in vitro fibrillation experiments only last for a few hours which is short compared to the disease progression of senile dementia. Modeling fibrillation *in vivo* is much more complex than that *in vitro* because of several practical reasons. First of all, there are potential interactions between fibrils and neurons. There are upstream reactions that lead to generation of amyloid monomers as well as down stream ones that decompose amyloid oligomers and fibrils. Also the transportation of biomolecules in living systems is hard to track and model. Second, the *in vivo* measurement itself is harder to perform as metabolism may interfere with chemical or immunoassaying. Therefore, the quality and quantity of the data are not as good as those *in vivo*. Finally, the physiological conditions *in vivo* are more difficult to control such as pH values, temperature, and ionic strength, etc.

Yet we adopted the same *in vitro* kinetic model of amyloid fibrillation for *in vivo* experimental data as a preliminary step toward full scale modeling. Cortical neurons of APP transgenic mice were observed by the multiphoton microscope which is a breakthrough technique for monitoring newly formed amyloid plaques. *In vivo* imaging of amyloid pathology was recorded after the addition of blue methoxy-XO4, the staining specific for amyloid deposition. As shown in Figure 3-4, the sizes of the plaques increased rapidly within the first day of experiment and stayed at about the same level afterwards. We used the same values of reaction rate constants yet changed the initial amyloid protein concentration. The initial concentration we used for this case was 0.7 mg/mL compared to the value 2 mg/mL we used for matching Figure 3-2. Granted that other physiological factors may affect the rate at which amyloid proteins fibrillate, the time it took for significant amount of fibrils to form is roughly inversely proportional to the initial concentration of amyloid proteins. The following section discusses the concentration effects in details.

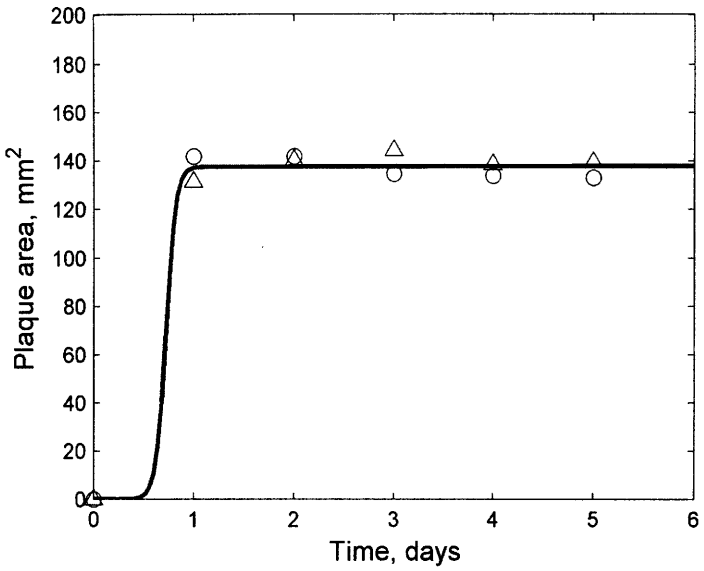

Figure 3-4 *In vivo* fibrillation responses in cortical neurons of APP transgenic mice. Multiphoton Imaging techniques were used to track the size of amyloid beta plaque since its formation [109]. The experiment continued for about one week (open triangles and circles) with the simulation results by our model (solid line).

3.3.3 Initial concentration effects

Data from Fink's group [117] showing the effect of varying initial concentration (0.2 to 20 mg/mL) of human recombinant insulin on the fibrillation are reproduced in Error! Reference source not found.A. Clearly, the higher the initial concentration of insulin, the shorter the lag-time and the steeper the growth curve. However, as can be seen from the figure, the ThT intensity asymptotes for long times are not proportional to the initial amount of protein in the feed. This result coincides with other results in our group (unpublished). Thus, ThT fluorescence does not grow linearly with respect to the amount of fibers present. By applying a single set of kinetic rate constants for seven different initial concentrations, our initial simulations did show consistent trends. However, at first the simulated asymptote of each individual concentration could not match the experimental results.

In order to quantify the concentration results better, nonlinear effects from at least two possible sources should be considered; the non-ideal behavior of proteins at high concentrations and a possible artifact from the fluorescence ThT assay. The activity coefficients of proteins at high concentrations are typically not constants and should be considered in the model [4]. Second, as mentioned above, nonlinearity with the ThT signal exists perhaps because ThT measurements depends on the ThT:fibril formation which involves stoichiometric binding of both compounds [97]. This nonlinear relationship is unknown so the proportionality constants based on each curve was estimated. The first step was to estimate the activity of insulin at each concentration based on the experimental data given a set of kinetic rate constants. Afterwards, the activity coefficients were computed by dividing the activity values by the original concentrations. Finally, the concentration of ThT:fibril complex was the product of proportional constant and asymptotic fibril concentration. The values of the activity coefficient and ThT:fibril

complex concentration are summarized in Error! Reference source not found.B. As expected from estimates using the equation of state, it can be seen from Error! Reference source not found.B that the calculated activity coefficients decreased with an increase in the initial insulin concentration. On the other hand, since the amount of ThT added in each run was fixed regardless of the initial amount of insulin added, it became the limiting agent at high insulin concentration. Thus, ThT:fibril complex concentration did not rise linearly with increasing initial insulin concentration, but appeared to reach an asymptote.

After the adjustment regarding the nonlinearity, the simulated results by our model match the experimental data better. Yet additional experiments that measure the actual protein quantities by osmotic pressure, for example, and determine the multivariate relationship between ThT concentration, amyloid fibrils, and fluorescence signal would be useful in testing our hypothesis.

A

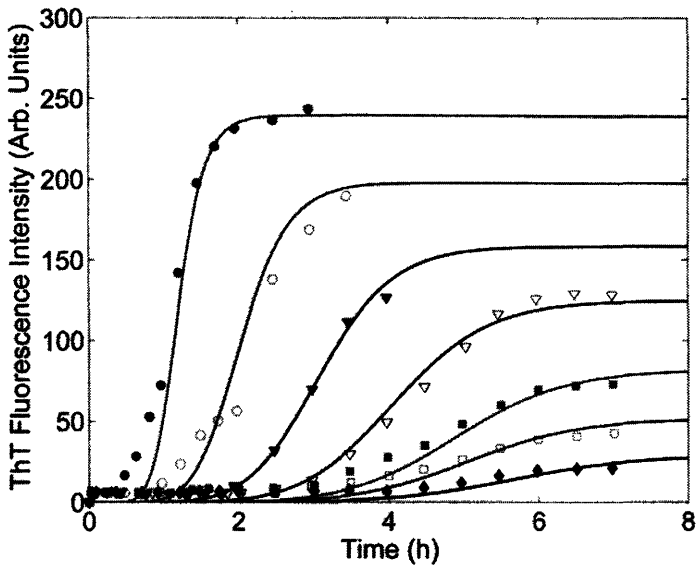

B

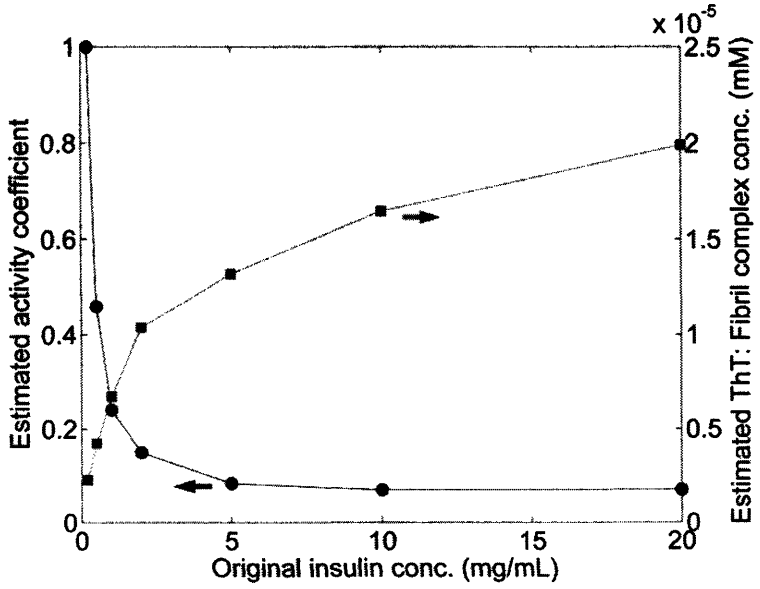

Figure 3-5 Initial concentration effects on insulin fibrillation were monitored by ThT fluorescence.
(A) The experimental measurements and simulations of fibrillation responses starting at seven initial insulin concentrations: 20 mg/ml (solid circles), 10 mg/ml (open circles), 5.0 mg/ml (solid triangles), 2.0 mg/ml (open triangles), 1.0 mg/ml (solid squares), 0.5 mg/ml (open squares), and 0.2 mg/ml (solid diamonds). The solid lines are the optimal nonlinear least square fit. Data source: Nielsen, 2001 [117]. (B) The estimated activity coefficients (solid circles) and equilibrated ThT:fibril complex concentrations (solid squares) as functions of initial insulin concentrations. The lines are used to connect the calculated points and do not represent a fit.

3.3.4 Effects of seeding

The addition of fibril seeds to a solution that is in the process of forming fibrils shortens the lag time. This effect has been termed a "nucleation-dependent" phenomenon by Wood et al. [174]. They explained that the added seeds act as catalytic sites that induce conformational changes in the protein (α-synuclein) and accelerate the reaction rates; also Scheibel et al. [132] have termed this "nucleated conformational conversion". In Figure 3-6 both the effect of adding seeds to the initial insulin solution (2 mg/ml) and our simulation results are shown [70]. For the simulations, a single set of rate constant values was used for both curves because seeding only increases the likelihood of collision but not the probability of the corresponding reaction actually taking place. Since only the weight of the added fibril seeds was reported, the number of reactive ends was not known (nor details about the length distribution of fibrils). Thus, the estimated initial fibril concentration was obtained by minimizing the total sum of squared errors from both data sets with and without seeding. The best estimate for the initial concentration of fibril was 2.53×10^{-7} mM for a 10 wt% addition of seeds. This low value supports the hypothesis that fibril ends were the reactive sites although fibrils were composed of a large number of monomers [142]. As can be seen from the fit of the model to the data in Figure 3-6, the model does not capture the effect of the shortened lag-time very accurately. A possible reason was that there exists size distribution of the added seeds and clusters. Unfortunately, without knowledge of this distribution, an estimate of the total added number of fibril ends was made. This likely oversimplified the seeding processes.

The explanation of the seeding effect from this analysis is based on the fact that the rate constants for fibril growth were orders of magnitude larger than those for the nucleation process. Hence fibril growth could not take place unless sufficient amounts of nuclei were present. Therefore, the addition of seeded fibrils allows the system to by-pass the slow nucleation phase and reach the growth phase much faster and earlier.

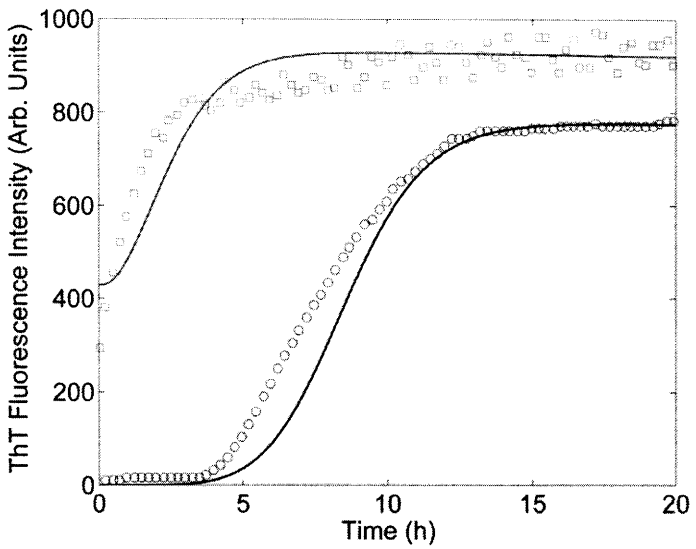

Figure 3-6 The fibrillation responses reflecting effects of seeding.
The measured and simulated fibrillation responses without seeding (open circles) and with 10 wt% seeding (open squares) were monitored by ThT fluorescence. The solid lines are the simulated responses with initial insulin concentration equal to 2 mg/ml. Data source: Hong and Fink [70].

3.3.5 Stirring effects

It has been reported that stirring or shaking can shorten the lag phase and speed up fibrillation process. One proposed reason for these effects was that agitation would increase the air-water interface and the presence of additional hydrophobic interfaces (air) would accelerate nucleation [148]. Other possible explanations include that additional mixing accelerates polymerization by breaking up large complexes and increasing the collision of reactive complexes with each other and with fiber ends [142]. Figure 3-7 contains the transient responses of measured as well as simulated dissolved insulin concentrations under different rotational speeds for an initial concentration of 0.6 mg/ml [148]. Both demonstrate that higher rotational speed results into faster fibrillation and shorter lag times. From Table 3-2, the rate constants increase for nucleation and for fibril formation with increased mixing. That is, the values of $k_{nu,1}$ and $k_{fb,1}$ roughly doubled and tripled, which suggest an increase in the mass transfer coefficients caused by a higher collision rate between monomers and oligomers as well as between monomers and fibrils. The nearly four fold increase in k_{fb-} indicates that the fibers were losing oligomers from the end of the fibrils to create new nuclei.

A simple film theory can be adopted to predict the apparent rate constants under the influence of both transport and reaction [94]. According to this theory, transport and reaction resistances are in parallel and additive. Hence, being limited by diffusion at first, the rate of stationary process may increase and become reaction-controlled under stirring. The faster rotation initially results in larger apparent rate constants but the process may eventually become reaction controlled. Beyond that point, even more vigorous stirring and hence convection would not speed up the reaction any longer. Measuring fibrillation responses under different rotational speed can help estimating the amount of kinetic energy needed to overcome the diffusion barrier.

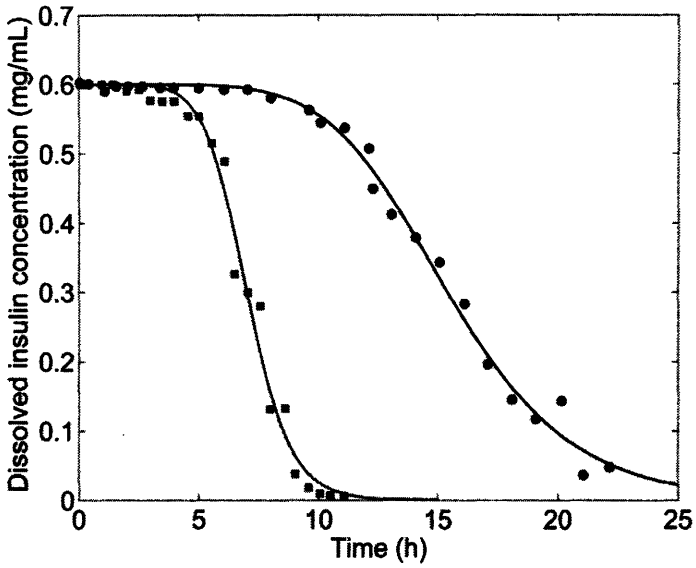

Figure 3-7 The dissolved insulin concentrations measured by UV absorbance.
The concentration is 0.6 mg/mL under different speeds of stirring: 80 revolutions per minute (rpm) (solid circles), and 160 rpm (solid squares). The solid lines are the optimal nonlinear least square fit. Data source: Slusky, 1991 [148].

3.3.6 Effects of adding stabilizing and destabilizing osmolytes

To investigate the role of osmolytes during nucleation and fibril formation, 300 mM osmolytes were added to the 2 mg/ml insulin solution at pH 1.6 and 65°C. The time course of fibrillation was followed by measuring A_{600}. To probe the effect of stabilizing osmolytes different sugars were chosen to reduce protein denaturation and aggregation in solution. Furthermore, sugars varying in chemical structure viz. monosaccharide (glucose, fructose), disaccharide (maltose, sucrose, trehalose) and trisaccharide (raffinose, melezitose) were used. Urea and guanidium hydrochloride were chosen as standard destabilizing osmolytes. The thermodynamic and structural properties of the osmolytes, their effect on the fibrillation process, the rate constants of nucleation and growth and the goodness-of-fit for the model are summarized in Table 3-3. For the fibrillation process, the osmolytes at 300 mM are compared to that without osmolyte at 2 mg/ml insulin (Table 3-3). Figure 3-8 illustrates the effect of the osmolytes on fibrillation kinetics. In the absence and presence of osmolytes, the nucleation and growth curves exhibit an initial lag phase followed by fibril growth and saturation or equilibrium. The lag-time changed substantially suggesting that the formation of a critical nucleus was dependent on the additives. From Figure 3-8, it can be clearly seen that stabilizing osmolytes (sugars) and destabilizing osmolytes (urea and guanidium hydrochloride) delay and speed-up the nucleation process, respectively.

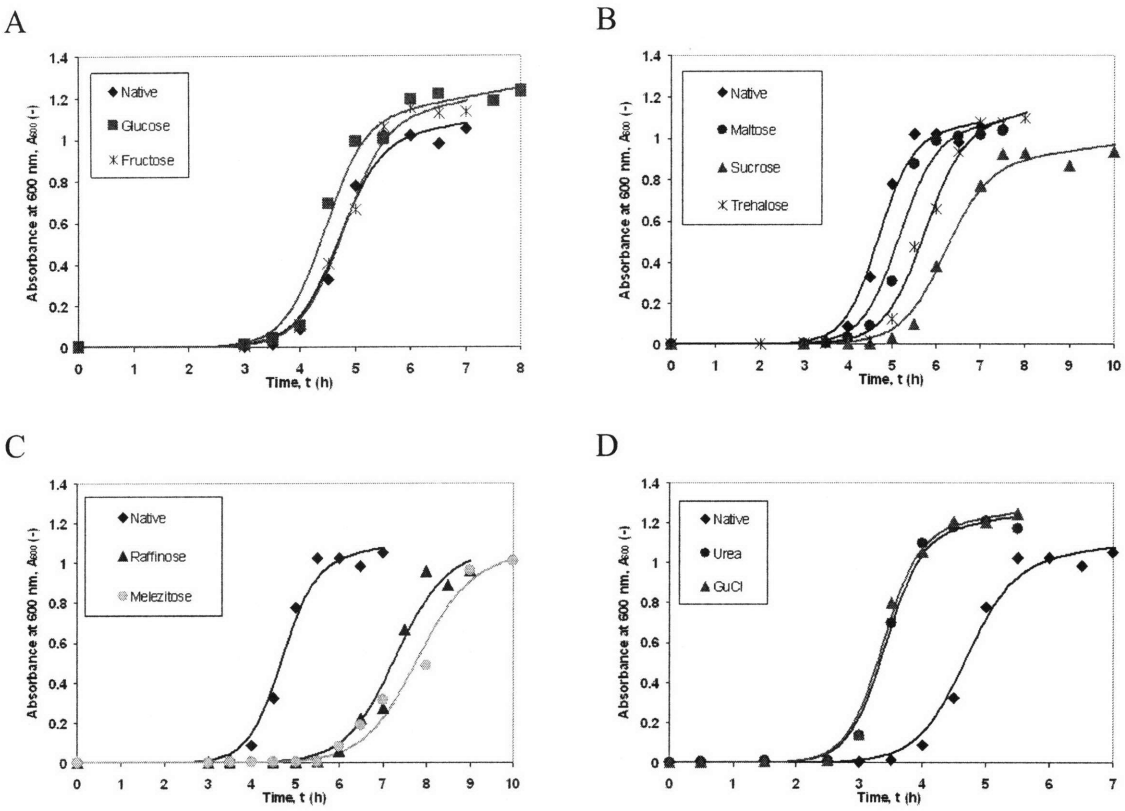

Figure 3-8 Fibrillation kinetics of 2 mg/ml human insulin at pH 1.6, T = 65°C.
300 mM osmolytes was added to the insulin solution at t = 0 in all cases. Effect of (A) monosaccharides – glucose and fructose. (B) disaccharides – maltose, sucrose and trehalose. (C) trisaccharides – raffinose and melezitose. (D) Effect of destabilizers – urea and guanidium hydrochloride. Symbols are experimental data and solid lines are best model fit. Absorbance at 600 nm (A600) is a measure of the suspended solids (fibrils).

Table 3-3 Osmolytes and their properties together with their influence on fibrillation kinetics

	Osmolyte	Heat of solution [111], ΔH_s (kJ/mol)	Neutral molecular surface area[c], A_0 ($Å^2$)	Nucleation rate constant, k_{nu+} (h^{-1} mM^{-1})	Fibrillation rate constant, k_{fb+} (h^{-1} mM^{-1})	Lag-time, t_{lag} (h)	Goodness of fit, R^2 (-)
	Native	-	-	2.09×10^{-2}	4.67×10^{6}	3.30	0.978
Mono-saccharide	Glucose	-5.67	80.2	2.33×10^{-2}	4.48×10^{6}	3.12	0.974
	Fructose	N/A	88.9	2.05×10^{-2}	4.21×10^{6}	3.36	0.985
Di-saccharide	Maltose	-19.4	113.7	1.78×10^{-2}	4.27×10^{6}	3.66	0.970
	Sucrose	-16.3	137.3	1.26×10^{-2}	4.18×10^{6}	4.38	0.983
	Trehalose	-27.2	145.2	1.48×10^{-2}	3.75×10^{6}	4.08	0.990
Tri-saccharide	Raffinose	-38.3	N/A	9.80×10^{-3}	3.20×10^{6}	5.16	0.971
	Melezitose	N/A	N/A	8.66×10^{-3}	3.08×10^{6}	5.52	0.970
Destabilizing	Urea	-	11.6	3.71×10^{-2}	5.46×10^{6}	2.40	0.990
	Guanidium chloride	-	11.6	3.80×10^{-2}	5.45×10^{6}	2.40	0.990

3.4 Conclusion and further development

A three-stage model of fibrillation developed here was able to simulate the experimental data measured by us and by others. Hence, it provides a physical rational for the generic sigmoidal (formation of fibrils) and inverse sigmoidal (loss of protein) fibrillation responses. In addition to the autocatalytic nature of fibril growth, the large difference between nucleation and growth rate constants lead to ultra-fast growth of fibrils after the lag period. Estimated from the ratio of the forward and backward nucleation rate constants, the Gibbs free energy change ($\Delta G°$) of spontaneous reaction involving insulin monomers converted into nuclei was as large as 42.6 kJ/mol. In comparison with the logistic equation used by Nielsen et al. [117] and others, the computational model presented here can be simplified into the same functional form to fit fibrillation responses. The physically meaningful rate constants in our model correspond to experimentally observable variables. Previous mechanistic models have provided insight, such as the enzymatic nature of the fibril ends [132], the critical size of nucleus [143], and detailed equations from population balances [123]. Yet most of these models do not explicitly predict the delay time and nor do they follow the sigmoidal behavior observed during experiments. For incorporating sets of nucleation and elongation reactions, the present model and the one proposed by Flyvbjerg et al. [47] both demonstrate better goodness-of-fit. Yet of these two models the detailed reactions schemes and predicted asymptotic oligomer concentration are different. It will take further work to differentiate these two models to determine the applicability of each one.

Based upon the profiles of insulin fibrillation, the values of the same rate constant ($k_{nu,1}$, $k_{fb,1}$ or k_{fb-}) estimated under different conditions of initial insulin concentration, seeding, or mixing effects were relatively close. On the contrary, prion and Aβ1-40 demonstrate nucleation rates several orders faster than those for insulin, because both proteins are known to form fibrils under mild conditions (physiological pH and room or physiological temperature). For the initial insulin concentration effects, the simulated responses starting at different initial concentrations show a consistent trend with the experiments. The seeding effects of shorter lag time and faster growth rate were reflected in the predicted results by introducing a hypothetical amount of additional initial fibrils. The stirring raised the nucleation and elongation rates, which could be due to higher collision rates and more rapid dissociation of oligomers possibly from the ends of fibrils. Consequently higher reaction rates result in the shorter lag time and the steeper concentration profile.

Based on the work reported here, the following experiments are suggested to help further confirm a physical basis of the model and possibly indicate the molecular conformational properties that would be needed for inhibitors to bind to the nucleus or other oligomers so as to reduce their toxic affects. First, it is critically important to quantify the relationship between the output variables with the state variables of interest; i.e., match the spectroscopic measurements with the actual concentrations of fibrils. Second, one needs to track the temporal evolution of the oligomers (dimers, trimers... nucleus) and fibrils (i.e. fibril lengths and their temporal distribution) possibly by AFM to verify the critical nucleus size. Larger-size clusters could be followed using dynamic light scattering and isolated using a fractionation procedure together with a toxicity assay to determine actual pathogenic species [19, 87, 100, 104]. Third and fourth, with respect to seeding and agitation effects, a series of carefully designed experiments are needed [142]. For example, the number and size distribution of seeded fibrils should be known and varied prior to seeding so as to confirm the importance of the amino acids at the end of the fibrils or the total number of amino acids within the fibrils as reactive sites. In all the mixing or agitation experiments reported to date in the literature, the fundamental fluid mechanical properties (shear rate and distribution, vorticity, etc.) of the mixing conditions have not been reported. Clearly, what is needed is a well-controlled mixing experiment in which the sigmoidal fibrillation run is conducted under different and well-designed fluid mechanical conditions. Fifth, it could be very important to vary the temperature, pH and ionic strength during fibrillation. One could then estimate the activation energy and activity coefficients for formation of oligomers and fibrils. Sixth, based on molecular structures of several amyloid peptides that have been previously simulated [115, 116], the aggregation rate constants among oligomers could be estimated. In brief, our model extracts rate constants from transient experiments and bridges the gap between experiments and molecular simulation. This methodology can be used to evaluate the potential of fibrillation inhibitors or enhancers by the decrease or increase in reaction rates they introduce [99].

In summary, amyloid proteins undergo three stages: misfolding, nucleation, and elongation, before turning into fibril aggregates. Validated by many experimental results, this mechanistic model is applicable for various types of proteins, and for fibrillation under different environmental conditions. Further experiments tracking oligomer concentrations and theoretical analysis of molecular simulations are promising for determining pathological species and the desired properties of fibrillation inhibitors.

Table 3-4. The summary of nomenclature in Chapter 3

Symbols	Units	Definitions
A_0	mM	Initial insulin concentration
A_1	mM	Insulin monomer or insulin monomer concentration
A_{hex}	mM	Original insulin hexamer or its concentration
A_i	mM	Insulin cluster consisting of i monomers or its concentration
b	mM^{-1}	Proportional constant relating fibril concentration to exp signal
d_{AF}	m	The mean free path between monomer and fibril
D_{Ai}	m^2s^{-1}	Diffusivity of oligomer A_i
D_F	m^2s^{-1}	Diffusivity of fibril
$\Delta G°$	kcal/mol	Gibbs free energy of the reaction of monomers becoming *(n–1)*-mers
f	-	Our fibrillation model expressed as a function
F	mM	Fibrils or fibril concentration
i	#	Index of nucleation or elongation reaction or the size of cluster
J_{hex}	$mM \cdot h^{-1}$	The reaction flux of original insulin decomposition
$J_{nu,i}$	$mM \cdot h^{-1}$	The flux of *i*-th nucleation reaction
$J_{fb,i}$	$mM \cdot h^{-1}$	The flux of *i*-th fibrillation reaction
k_{app}	h^{-1}	The apparent growth rate of fibril, which is equal to $1/\tau$
K_c	$mM^{-(n-2)}$	Equilibrium constant between monomers and *(n–1)*-mers
k_{hex}	h^{-1}	Reaction rate constant of original insulin decomposition
k_{fb-}	h^{-1}	General reverse rate constant of fibrillation reaction
$k_{fb,1}$	$h^{-1}mM^{-1}$	Forward rate constant of the first fibrillation reaction
$k_{fb,i}$	$h^{-1}mM^{-1}$	Forward rate constant of *i*-th fibrillation reaction
$k_{fb,-i}$	h^{-1}	Reverse rate constant of *i*-th fibrillation reaction
$k_{nu,1}$	$h^{-1}mM^{-1}$	Forward rate constant of the first nucleation reaction
k_{nu-}	h^{-1}	General reverse rate constant of nucleation reaction
$k_{nu,i}$	$h^{-1}mM^{-1}$	Forward rate constant of *i*-th nucleation reaction
$k_{nu,-i}$	h^{-1}	Reverse rate constant of *i*-th nucleation reaction
m_i, m_f	h^{-1}	The slope of initial and final fibrillation response curve, respectively
n	#	Critical number of monomers in a nucleus
n_{exp}	#	The number of experimental data points
N	#	The average size of fibrils in terms of number of monomer
$\tilde{N}$	mol^{-1}	Avogadro constant
$\Phi(\underline{\theta})$	-	The objective function to be optimized with respect to $\underline{\theta}$
R	J/molK	Ideal gas constant, 8.314
R^2	-	Coefficient of determination
R_{Ai}	m	Characteristic length of oligomer A_i
r_1, r_2	mM	The first and second roots of the fibril quadratic equation
t_0	h	The time to 50% of maximal signal or the time of inflection point
t_i	h	The time of *i*-th experimental data point
$t_{\nu,\alpha/2}$	-	Student's t-distribution with degree of freedom ν, significance level α
τ	h	The time constant of fibril growth and it is equal to $1/k_{app}$
$\underline{\theta}$	-	The vector of parameters to be estimated

4 Modeling Short Term Plasticity

Short-term facilitation and depression refer to the increase and decrease of synaptic strength under repetitive stimuli within a timescale of milliseconds to seconds. This phenomenon has been attributed to primarily presynaptic mechanisms such as calcium-dependent transmitter release and presynaptic vesicle depletion. Previous modeling studies that aimed to integrate the complex short-term facilitation and short-term depression data derived from varying synapses have relied on computer simulation or abstract mathematical approaches. Here, we propose a unified theory of synaptic short-term plasticity based on realistic yet tractable and testable model descriptions of the underlying intracellular biochemical processes. Analysis of the model equations leads to a closed-form solution of the resonance frequency, a function of several critical biophysical parameters, as the single key indicator of the propensity for synaptic facilitation or depression under repetitive stimuli. This integrative model is supported by a broad range of transient and frequency response experimental data including those from facilitating, depressing or mixed-mode synapses. Specifically, the theory predicts that high calcium initial concentration and large gain of calcium action result in low resonance frequency and hence depressing behavior. In contrast, for synapses that are less sensitive to calcium or have higher recovery rate, resonance frequency becomes higher and thus facilitation prevails. The notion of resonance frequency therefore allows valuable quantitative parametric assessment of the contributions of various presynaptic mechanisms to the directionality of synaptic short-term plasticity. Also the model provides the reasons behind the switching behavior between facilitation and depression observed in experiments.

4.1 Current understanding of short term plasticity

Homosynaptic short-term plasticity (facilitation or depression) which operates within the timescale of several seconds [183] is fundamental to some primary forms of nonassociative learning such as habituation and sensitization in invertebrates and in mammals [24, 145]. These stimulus frequency-dependent synaptic processes have been linked to certain brain calculus or dynamic filtering computations that underlie a variety of brain functions and abnormalities [49, 126]. In cortical neurons, short-term plasticity provides a dynamic gain control mechanism that recalibrates the synaptic efficacy specific to certain input firing rate for optimal transmission [3, 160].

Synapses at different locations may demonstrate distinct short-term plasticity responses appropriate for specific functional roles [21]. Also, parallel inputs to a target may express a balanced mixture of synaptic facilitation and depression such that a linear input-output relationship is maintained regardless of the input firing rate [102]. The relative balance between short-term facilitation and depression in some neural pathways may undergo developmental changes that alter the signal transfer characteristics of these pathways [35]. In some brain regions, neurons innervated by the same nerve bundle may express distinct short-term or long-term plasticity that is specific to the afferent inputs [181].

Although both pre- and postsynaptic mechanisms may contribute to short-term plasticity, the preponderance of evidence indicates that postsynaptic effects are typically minor compared to presynaptic ones [6, 61, 183]. In particular, presynaptic vesicle trafficking is generally considered crucial in explaining short-term plasticity. For instance, the classic presynaptic vesicle depletion model is often used to follow depression dynamics [157, 165, 175] whereas calcium-dependent transmitter release is usually invoked to model facilitation [12, 179]. These early studies considered facilitation and depression separately without integrating the common pathways they share. Yet more recent experimental data point out that these two phenomena are not completely independent [38, 102, 106, 152].

Recently, there have been increasing efforts to develop integrative models that can unify the synaptic depression and facilitation data [38, 106]. Markram et al. [16] introduced a phenomenological model in which they describe the effects of action potential on the utilization of synaptic efficacy and the subsequent recovery. Both depressing and facilitating responses can be explained by their model. Although mathematically simple, most of the model's abstract parameters such as absolute synaptic efficacy and utilization of synaptic efficacy are not experimentally measurable or physiologically well-defined. Dittman et al. [77] proposed a comprehensive depression-facilitation model which incorporated detailed descriptions of the calcium dynamics involved in the transmitter release process. Yet the overall model complexity makes it difficult to interpret the effect of each model parameter on the excitatory response. Therefore, without extensive sensitivity analysis of model parameters, it is not straightforward to use the model to predict changes in short-term plasticity in new experiments.

Here, we present a general mathematical framework for presynaptic facilitation and depression based on first principles and established experimental data, with a view to pinpointing how specific biochemical parameters may contribute to the up- or down-regulation of synaptic strength. The proposed unified theory leads to a closed-form formula that parsimoniously predicts various forms of short-term synaptic plasticity with facilitation, depression, or mixed effects.

4.2 Model Development

4.2.1 Higher structure of the kinetic model

Figure 4-1A illustrates the principal biochemical pathways for excitatory neural transmission at a glutamatergic synapse. Correspondingly, Figure 4-1B summarizes the model structure consisting of three parts: calcium buffering, vesicle trafficking, and postsynaptic first order delay. At first, presynaptic stimuli modulate calcium concentration through calcium buffering, which is represented by a first-order linear differential equation. Then neurotransmitter vesicle trafficking triggered by the surge of calcium concentration is modeled by a set of chemical kinetics nonlinear differential equations. Finally, a linear first-order delay equation is adopted to convert transmitter release to postsynaptic response. Corresponding model equations are presented in the following sections. All model equations and stimuli were implemented on Matlab® Simulink (The Mathworks, Natick, MA). Table 4-3 defines the nomenclature of symbols used.

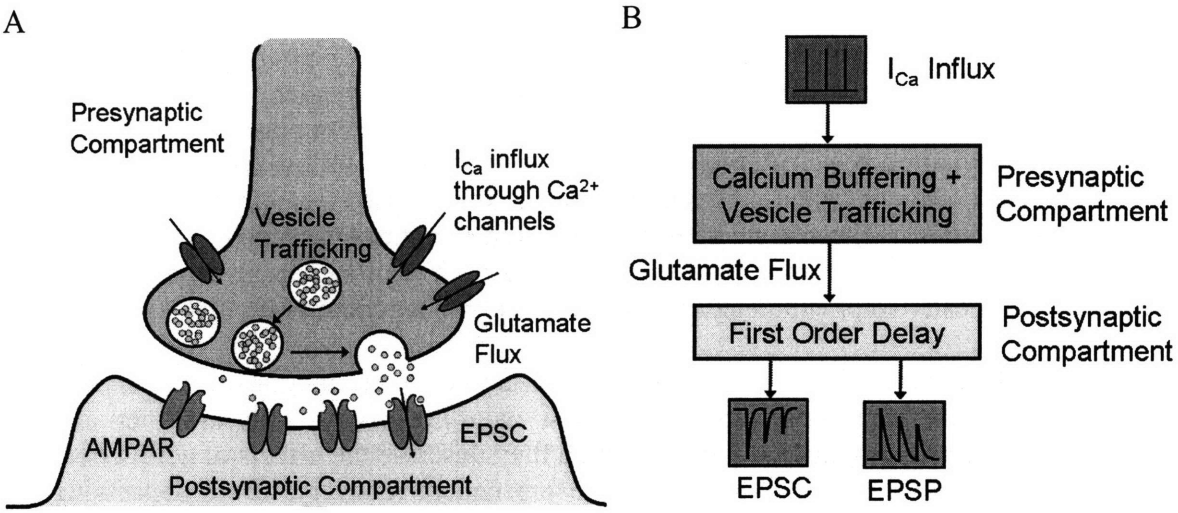

Figure 4-1 The diagram of cellular structure and signal process at synapse relevant to short-term plasticity.
A, The simplified structure of generic synaptic junctions and signal transmission pathways involved. AMPAR stands for α-amino-5-hydroxy-3-methyl-4-isoxazole propionic acid receptor; EPSC is excitatory postsynaptic current. B, The summary of the model structure with signals transduction from presynaptic compartment to postsynaptic compartment in series.

4.2.2 Presynaptic calcium buffering

A classic mechanism of short-term facilitation is the buildup of presynaptic residual calcium and the resultant increase in neurotransmitter release [6, 55, 79]. A first-order decay model is commonly used to relate calcium current I_{Ca} with intracellular calcium concentration Ca_i [39, 114]:

$$\tau_{Cai}\frac{dCa_i(t)}{dt} = \left(-Ca_i + Ca_{i0}\right) + K_{Ca}I_{Ca} \approx \left(-Ca_i + Ca_{i0}\right) + K_{Ca}\sum_{k=1}^{N_p}\delta(t-t_k) \qquad (4.1)$$

The intracellular calcium concentration starts at Ca_{i0} and is raised incrementally by each stimulus impulse, approximated herein by a Dirac Delta function δ(t) [38, 128]. The impact of each stimulus impulse to the intracellular calcium concentration is equal to the product of calcium gain and calcium current ($K_{Ca}I_{Ca}$). The calcium gain (K_{Ca}) is to convert the unit of charge to the unit of concentration. Once the stimulus sequence (k = 1, 2,…, N_p) ends, Ca_i decays with time constant τ_{Cai} toward Cai_0.

4.2.3 Presynaptic calcium-dependent vesicle trafficking

A vesicle depletion model with recovery has been variously proposed to describe the synaptic short-term depression process [13, 39]. According to this model, the active zone for transmitter release is either occupied by releasable vesicles (N_{rel}) or empty (N_{empty}):

$$\begin{aligned} &Exocytosis: \; N_{rel} \xrightarrow{P_{rel}I_{Ca}} N_{empty} + n \cdot Glu \\ &Recovery: \; N_{empty} \xrightarrow{k_{recov}} N_{rel} \end{aligned} \tag{4.2}$$

Upon stimulation, releasable vesicles discharge transmitters such as glutamate (Glu) and become empty after exocytosis. Calcium current (I_{Ca}) triggers swift and sharp increase of local calcium concentration which is necessary for inducing exocytosis. Therefore, exocytosis is assumed to occur only during each stimulus impulse with release probability P_{rel} [38, 84, 158]. The exocytosis process involves docking and priming of synaptic vesicle as well as fusion between the vesicle and membrane [170]. Several presynaptic protein molecules such as Munc13, Rab3, synaptotagmin, and kainate, have been suggested to mediate the calcium-dependent transmitter release [46, 130, 133, 156]. Meanwhile, empty vesicles are recycled and recover with rate constant k_{recov} [13, 107]. Synaptotagmin has also been found to facilitate vesicle recycling [170].

The flux of glutamate release ($Flux_{Glu}$) is equal to the stoichiometric coefficient (n) times the reaction flux of exocytosis. The latter is equal to the number of releasable vesicles (N_{rel}) multiplied by exocytosis rate constant ($P_{rel}I_{Ca}$). Even though some studies suggested higher order dependence of exocytosis rate on calcium current, the release probability has been assumed to be proportional to the first order of calcium current (I_{Ca}) or Dirac delta function for simplicity [38, 106]. For experiments with constant calcium current triggered by each stimulus, such simplification can be justified as the trend of the response will not be influenced by the constants being raised to higher power. Further, N_{rel} is the product of two factors: the dimensionless ratio of releasable vesicles (R_{rel}) and the sum of empty and releasable vesicles (N_{total}). Hence,

$$Flux_{Glu} = \frac{dGlu(t)}{dt} = nN_{rel}P_{rel}I_{Ca} = nN_{total}R_{rel}P_{rel}I_{Ca} \tag{4.3}$$

Since N_{total} remains roughly constant within the timeframe of a few seconds [77], Eq. (4.3) shows that $Flux_{Glu}$ is determined by two key variables: R_{rel} and P_{rel}. Initially, R_{rel} = 1 under the assumption that all vesicles are fully refilled at first. From Eq. (4.2), the time course of R_{rel} during stimulation depends on the difference between the recovery and exocytosis rates. The former term is equal to the fraction of empty vesicles ($1-R_{rel}$) multiplied by k_{recov} while the latter is the ratio of releasable vesicles (R_{rel}) times the exocytosis rate constant. Thus, the rate of change in R_{rel} can be expressed as:

$$\frac{dR_{rel}(t)}{dt} = k_{recov}(1 - R_{rel}) - P_{rel}I_{Ca}R_{rel} \tag{4.4}$$

As shown in Fig. 2B, R_{rel} starting from an initial value of unity decreases with time because of vesicle depletion caused by repetitive stimuli. It continues to fall until reaching the level where consumption is balanced by recovery.

The other variable, release probability P_{rel}, is dependent upon intracellular calcium concentration [7]. Evidence suggests that the binding of calcium ion to its sensor, synaptotagmin-1, is cooperative and obeys the Hill equation [40, 124]:

$$P_{rel} = P_{rel,max} \frac{Ca_i^{n_{Hill}}}{Ca_i^{n_{Hill}} + K_{rel,1/2}^{n_{Hill}}} \tag{4.5}$$

The value of Hill coefficient (n_{Hill}) was reported to be four on average which coincides with the number of binding sites of calcium on calmodulin [79, 131]. The parameter $P_{rel,max}$ denotes maximum release probability while $K_{rel,1/2}$ is the $[Ca_i]$ at half occupation.

Repetitive stimulation of presynaptic neurons was found to elicit steady-state excitatory postsynaptic current (EPSC) larger than those expected from the above depletion model [24, 88, 165]. To rectify this discrepancy, the idea of calcium-dependent recovery was proposed (Dittman et al., 2000). We used ligand binding kinetics to describe the dependence of recovery rate constant on residual calcium. As shown in Eq. (4.6), the value of rate constant k_{recov} drops to $k_{recov,min}$ when Ca_i is small, and approaches $k_{recov,max}$ when Ca_i greatly exceeds the affinity constant $K_{recov,1/2}$:

$$k_{recov} = k_{recov,min} + (k_{recov,max} - k_{recov,min}) \frac{Ca_i}{Ca_i + K_{recov,1/2}} \tag{4.6}$$

4.2.4 Postsynaptic response

EPSC responses to presynaptic transmitter release are commonly modeled by a first-order decay equation [37, 38]:

$$\tau_{EPSC} \frac{dEPSC(t)}{dt} = -EPSC - K_{Glu} Flux_{Glu} \tag{4.7}$$

where K_{Glu} is the gain of EPSC per unit glutamate flux and τ_{EPSC} is the EPSC decay time constant.

4.3 Modeling Results

Based on the above dynamic model of synaptic transmission, we derived an analytical solution to predict the postsynaptic plasticity response with respect to varying frequency of stimulation. The experimental data for model validation came from the calyx of Held in brainstem, parallel fibers to cerebellar Purkinje cells, and neocortical pyramidal cells.

4.3.1 Analytical Solution of Stimulation Frequency-Dependent Plasticity

Stimulation frequency-dependent synaptic plasticity has long been recognized [157, 182]. Previous modeling studies have used physiologically complete but mathematically less intuitive expressions to describe this phenomenon [38]. A more tractable approach is to consider the impulse-by-impulse moving time-averaged (instead of instantaneous) values of all state variables and solve for the resultant steady-state EPSC as a function of stimulation frequency. This simplification allowed our derivation of a closed-form solution that clearly delineates the key determinants of short-term synaptic plasticity.

Steady-state EPSC as an explicit function of stimulation frequency

Since the EPSC caused by a stimulus impulse is proportional to the corresponding glutamate flux (Eq. (4.3)), the steady-state *EPSC* at any stimulation frequency r ($EPSC_{ss}(r)$) can be rewritten as:

$$EPSC_{ss}(r) \propto Flux_{Glu,ss}(r) \text{ per stimulus impulse} = nN_{total} \cdot P_{rel,ss}(r) R_{rel,ss}(r) \qquad (4.8)$$

where $P_{rel,ss}(r)$ and $R_{rel,ss}(r)$ are the steady-state values of P_{rel} and R_{rel} at stimulation frequency r and nN_{total} is the total number of releasable glutamate. Both $P_{rel,ss}$ and $R_{rel,ss}$ are functions of the steady-state moving-average intracellular calcium concentration $Ca_{i,ss}$. The value of $Ca_{i,ss}$ is derived by setting the left hand side of Eq. (4.1), i.e. time derivative of Ca_i, equal to zero and solving the remaining algebraic equation. Hence, from Eq. (4.1) and Eq. (4.5) we obtain $P_{rel,ss}(r)$ as:

$$\begin{aligned} Ca_{i,ss}(r) &= \bar{I}_{Ca} \cdot K_{Ca} + Ca_{i0} = r \cdot K_{Ca} + Ca_{i0} \\ P_{rel,ss}(r) &= \frac{P_{rel,max} \cdot Ca_{i,ss}(r)^{n_{Hill}}}{Ca_{i,ss}(r)^{n_{Hill}} + K_{rel,1/2}^{n_{Hill}}} = \frac{P_{rel,max} \cdot (r \cdot K_{Ca} + Ca_{i0})^{n_{Hill}}}{(r \cdot K_{Ca_i} + Ca_{i0})^{n_{Hill}} + K_{rel,1/2}^{n_{Hill}}} \end{aligned} \qquad (4.9)$$

where $\bar{I}_{Ca}$ (see Figure 4-2A) is the steady-state average calcium current influx, i.e., the steady-state moving time-average of the unitary current resulting from each stimulation impulse. Then $\bar{I}_{Ca}$ can be replaced by r since the average value is equal to one divided by the period.

Similarly, $R_{rel,ss}$ can be derived from Eq. (4.4) by setting its left hand side equal to zero at steady state as follows (see Figure 4-2B):

$$\begin{aligned} & k_{recov,ss}(r) \cdot (1 - R_{rel,ss}) - P_{rel} R_{rel} \bar{I}_{Ca} = 0 \\ \therefore \quad & R_{rel,ss}(r) = \frac{k_{recov,ss}(r)}{k_{recov,ss}(r) + P_{rel,ss}(r) \bar{I}_{Ca}} = \frac{k_{recov,ss}(r)}{k_{recov,ss}(r) + P_{rel,ss}(r) \cdot r} \end{aligned} \qquad (4.10)$$

where $k_{recov,ss}(r)$, the steady-state value of k_{recov}, is obtained by plugging $Ca_{i,ss}(r)$ into Eq. (6). The typical time course of R_{rel} is shown in Fig. 2B with steady state value labeled according to Eq. (10).

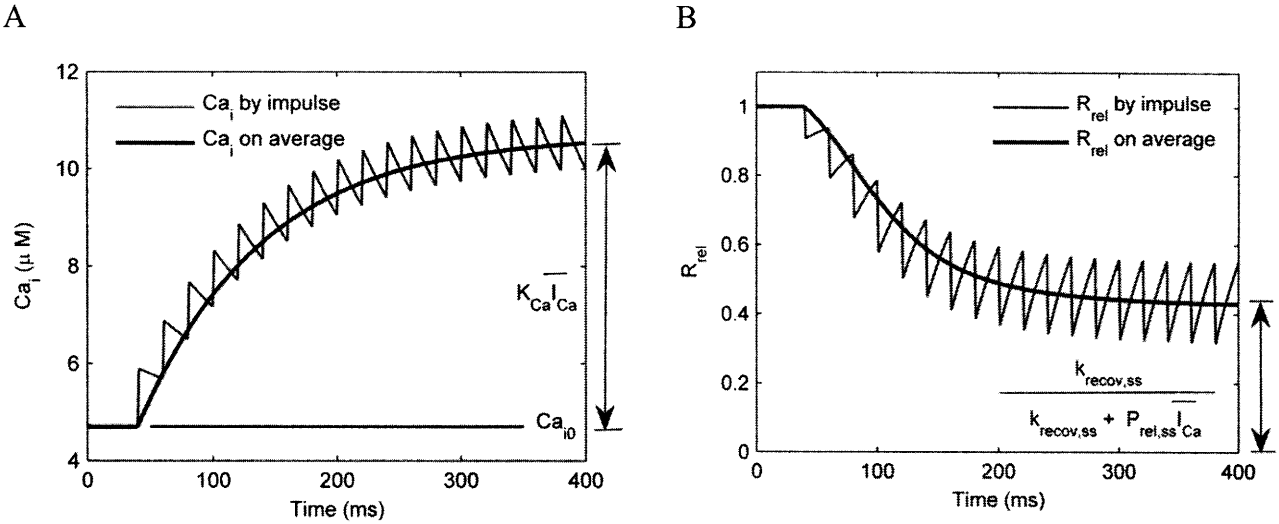

Figure 4-2 The instantaneous time courses of key biophysical variables. Those caused by impulses are drawn in zigzag lines. Also the average time courses are represented by the smooth curves. (A) An example of intracellular calcium concentration (Ca_i) time course. (B) An example of releasable vesicle ration (R_{rel}) time course.

By substituting Eqs. (9) and (10) into Eq. (8), we obtain the following closed-form expression for the steady-state EPSC as an explicit function of stimulation frequency r:

$$EPSC_{ss}(r) = \left(\frac{(r \cdot K_{Ca} + Ca_{i0})^{n_{Hill}} + K_{rel,1/2}^{n_{Hill}}}{P_{rel,max} \cdot (r \cdot K_{Ca} + Ca_{i0})^{n_{Hill}}} + \frac{r}{k_{recov,ss}(r)} \right)^{-1} \tag{4.11}$$

Resonance stimulation frequency as an explicit function of physiological parameters

The steady-state EPSC is proportional to the product of $P_{rel,ss}(r)$ and $R_{rel,ss}(r)$ as suggested in Eq. (8). In general, $P_{relss}(r)$ tends to increase with stimulation frequency whereas $R_{reslss}(r)$ decreases as a result of vesicle depletion. Therefore, the steady-state EPSC should exhibit a maximum at some resonance frequency $r_{resonance}$ like a bandpass filter [73]. This resonance frequency can be found by taking the derivative of $EPSC_{ss}(r)$ from Eq. (4.11) with respect to stimulation frequency and setting the resultant equal to zero:

$$\left. \frac{\partial EPSC_{ss}(r)}{\partial r} \right|_{r_{resonance}} = 0 \tag{4.12}$$

The detailed mathematical derivation was executed by using Symbolic Toolbox of Matlab®. The resultant closed-form solution is:

$$r_{resonance} = \frac{-Ca_{i0}}{K_{Ca}} + \left(\frac{n_{Hill} K_{rel,1/2}^{n_{Hill}} \cdot k_{recov}}{K_{Ca}^{n_{Hill}} \cdot P_{rel,max}} \right)^{\frac{1}{1+n_{Hill}}} \tag{4.13}$$

The above analytical formula is valuable in that though simple, it indicates whether a synapse tends to depress or facilitate at any stimulation frequency. The reason is that resonance frequency is the optimal stimulation frequency that elicits maximal excitatory response so a high resonance frequency indicates growing response with respect to frequency, i.e., facilitation while the opposite condition suggests depression. It also reveals the functional influences of various physiological parameters on short-term plasticity. The validity of Eqs. (4.11) and (4.13) is further tested in the following by comparison with experimental data for short-term facilitation, depression or mixed effects.

4.3.2 Facilitating synapses

A canonical experimental model of paired-pulse facilitation is found in the cerebellar parallel fiber (PF) connections to Purkinje cells [6]. Dittman et al. [77] applied stimuli of varying frequencies to the parallel fibers and recorded the resultant time- and frequency-dependent postsynaptic responses, both of which can be explained by our unified model.

Figure 4-3A demonstrates good agreement between experimental and simulated responses in normalized EPSC as a function of stimulation frequency. Figure 4-3B shows the corresponding frequency dependence of P_{rel} and R_{rel}. Note that for frequencies below 40 Hz, substantial growth in release probability with increasing residual calcium outweighs the loss of releasable vesicles as stimulation frequency is increased.

Figure 4-3C shows the transient EPSC caused by 10 presynaptic spikes delivered at 50 Hz as found experimentally and closely matched by the model. The growing EPSC amplitude is explained by the simulated P_{rel} and R_{rel} vs. time in Figure 4-3D. Specifically, rising calcium concentration during stimulation leads to increasing release probability, hence presynaptic facilitation. The upward trend continues until around 120 ms where this is offset by a concomitant decrease in releasable vesicle, and the EPSC levels off.

A single set of parameter values used in all four figures are summarized in Table 4-1. The initial recovery rate constant (2.2×10^{-2} ms^{-1}) and initial calcium concentration (4.7 μM) are in the same order of magnitude as those reported in the literature [7, 38]. The predicted low initial release probability (0.06) and high recovery rate contribute to the presynaptic facilitation of Purkinje cells under repeated stimuli.

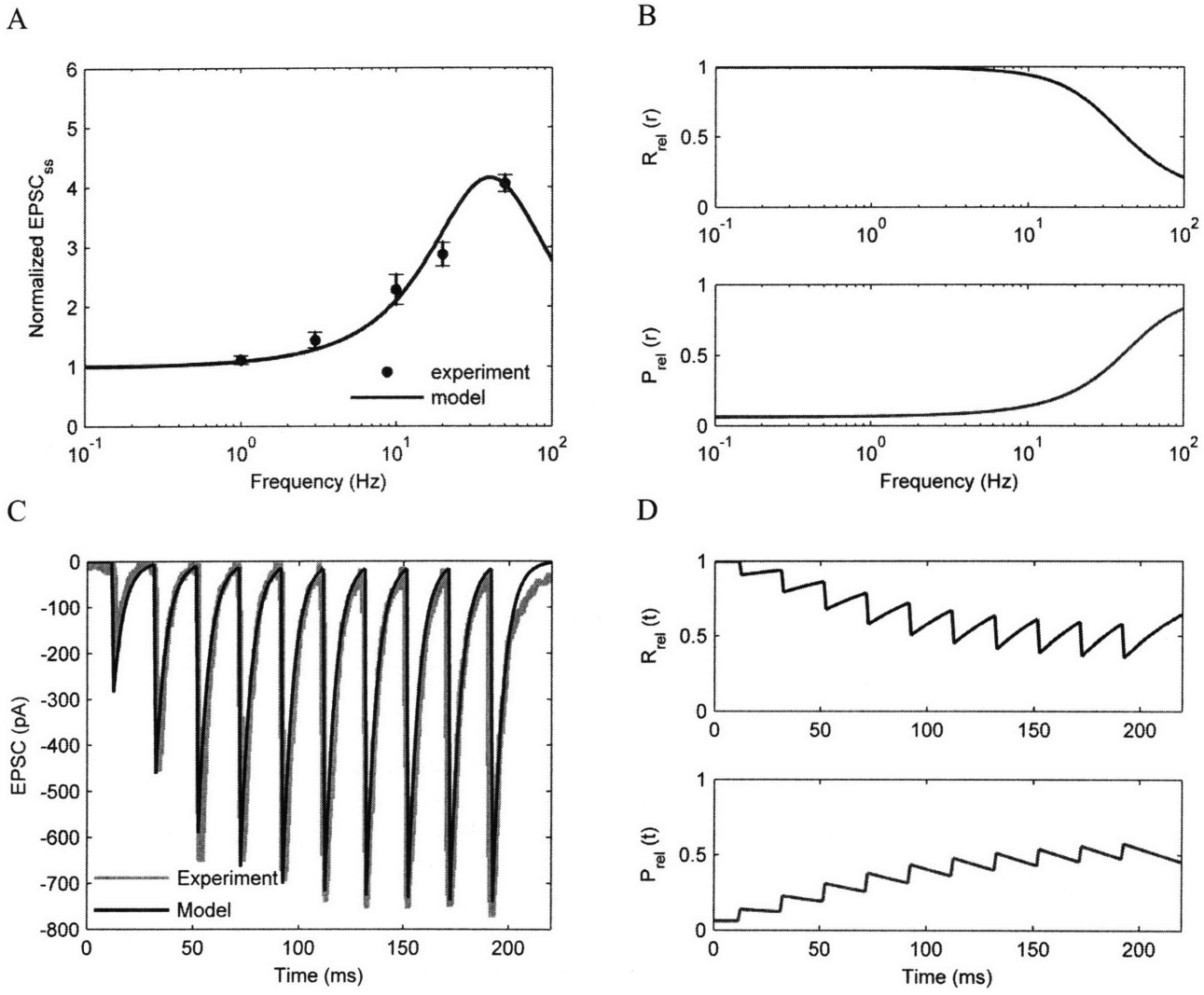

Figure 4-3 Facilitation in the rat parallel fiber to Purkinje cell synapse.
(A) The frequency response of EPSC. Data are shown as mean ± standard error of the mean (SEM). (B) The frequency response of vesicle ratio and release probability by model. (C) The transient EPSC caused by stimuli at 50 Hz. (D) The corresponding transient releasable vesicle ratio and release probability by model. Data source: [38].

4.3.3 Depressing synapses

The calyx of Held has been widely used for studying short-term depression [7]. In contrast to early experiments on neuromuscular junctions [36], calyx of Held synapses in rat brainstem slices showed higher steady-state EPSC responses than predicted by simple depletion models [165] – a phenomenon which has been attributed to calcium-dependent recovery [38]. With our unified model, both the transient and frequency responses can be explained with exactly the same set of parameter values as summarized in Table 4-1.

In Figure 4-4A, the steady-state EPSC decreases with frequency due to significant depletion of the pool of releasable vesicles with high-frequency stimuli, as demonstrated in Figure 4-4B. Even though the release probability grows with frequency, it is not significant enough to counteract the loss of releasable vesicles. In conclusion, the high release probability of the vesicle pool (0.46) and its slow recovery (1.0×10^{-4} ms^{-1}) contribute to the depression behavior in calyx of Held. To further demonstrate the applicability of this model, we show the frequency response of EPSC in the nucleus tractus solitarii (NTS) synapse in Fig 4E. The corresponding temporal profiles of P_{rel} and R_{rel} are plotted in Fig 4F [28]. This result suggests that this kinetic model is applicable throughout different types of depressing synapses, and the underlying mechanisms leading to depression may be similar.

Figure 4-4C shows the temporal synaptic depression of the calyx of Held from experiment and simulation for 30 impulses of 10 Hz. The temporal depression can be explained by Figure 4-4Dwhere the releasable pool is seen to decrease dramatically (from 1 to 0.2) during stimulation with little corresponding increases in release probability (from 0.44 to 0.6). The relatively high initial release probability reflects the high sensitivity of calcium sensor in the calyx of Held. In Table 4-1, our estimated value of $K_{rel,1/2}$ is as low as 4 μM which is close to the value (10 μM) reported previously [155].

While depletion of vesicle pools is considered as the principal mechanism, short-term depression at calyx of Held may be attributed to other reasons as well. According to the review of calyx of Held, other mechanisms include the inactivation of presynaptic calcium current and changes in action potential waveform [164]. The model proposed here can actually be applicable to accommodate these mechanisms as well. For instance, the calcium currents triggered by each stimulus in Eq. (4.3) and (4.4) have been considered constant. Yet it is possible to model time-varying calcium influx to take into account the waveform change in action potential. Also the dependence of release probability on calcium current can be modified into a time-dependent function as suggested in previous studies [178]. With calcium current measured at each stimulus, Eq. (4.14) as a more detailed version of depletion model can be built by coupling with I_{Ca} inhibition to cover broader range of experimental data. I_{Cai} is the calcium current elicited by the i-th stimulus while $Flux_{Glu1}$ is the flux of glutamate triggered by the first stimulus. Finally, n_F denotes the power order of calcium current influence on the flux of glutamate.

$$Flux_{Glui} = Flux_{Glu1}\left(I_{Cai}\right)^{n_F} \tag{4.14}$$

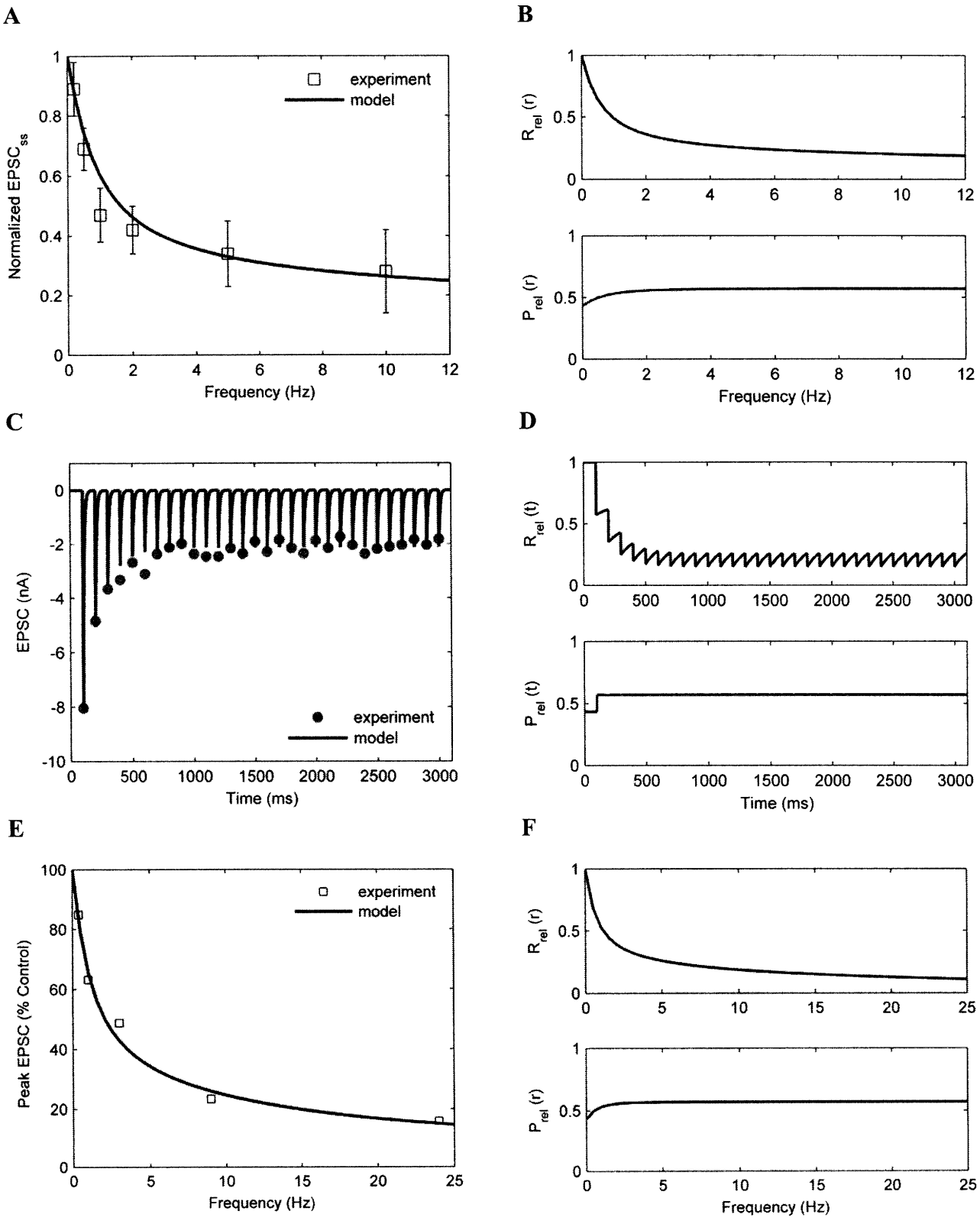

Figure 4-4 Responses of depressing synapses.
(A) The frequency response of EPSC in the rat calyx of Held synapse. Data are shown as mean ± standard error of the mean (SEM). (B) The frequency response of vesicle ratio and release probability by model. (C) The transient EPSC caused by stimuli at 10 Hz in the rat calyx of Held synapse. (D) The corresponding transient releasable vesicle ratio and release

probability by model. (E) The frequency response of EPSC in the nucleus tractus solitarii (NTS) synapse. (F) The frequency response of vesicle ratio and release probability by model. Data sources: [165] and [28].

4.3.4 Synapses with mixed facilitation-depression effects

The dendrites of neocortical pyramidal neurons receive excitatory and inhibitory synaptic inputs and play an important role in integrating the input signals selectively [161]. Many of these excitatory synapses demonstrate maximal excitatory postsynaptic potential (EPSP) at varying frequency ranges. Thus, each synapse of a single neuron behaves like a bandpass filter with its own natural resonance frequency so that presynaptic spikes of the same frequency may result in differing amplitude modulation via different synapses [73]. The mechanism underlying such a resonance effect may be related to frequency-dependent transition between facilitation and depression [106]. For this reason, pyramidal cells provide an excellent model system for studying mixed synaptic effects and signal filtering [69].

The experiment data were derived from sagittal slices containing pyramidal neurons in the somatosensory cortex of Wistar rats [106]. The experimental transient response and frequency response data were fit with the same set of parameter values summarized in Table 4-1. The frequency response of the steady-state EPSP in Figure 4-5A was plotted using the analytical solution given in Eq. (4.11) whereas the transient EPSP in Figure 4-5C was simulated by applying 16 Dirac delta functions at 30 Hz to the Matlab® Simulink model (Eqs. (4.3)-(4.7)). The corresponding releasable vesicle ratio (R_{rel}) and release probability (P_{rel}) are shown in Figure 4-5B and Figure 4-5D, respectively. The transient response demonstrates facilitation under stimulus frequency of 30Hz because of growing release probability shown in Figure 4-5D. Some parameter values listed in Table 2 such as the recovery rate constant and resonance frequency are in agreement with experimental values. First, the recovery rate constant k_{recov0} (7.5×10^{-3} ms^{-1}) is fairly close to the value of 7.7×10^{-3} ms^{-1} obtained by taking the inversion of recovery time constant of 130 ms reported by Markram et al. [106].

Then the corresponding frequency response of both experimental and simulated steady-state EPSP (Figure 4-5A) shows a resonance peak at ~25 Hz, in close agreement with that predicted by Eq. 13. The resonance effect is due to the opposing trends of the amount of available vesicles and the release probability with varying stimulation frequency. The resonance bandwidth is defined as the range of stimulation frequency where the EPSP amplitude is at least 71% (-3dB) of the maximum. Below this pass band, stimuli of low frequency do not cause sufficient calcium ion influx to maintain the initial release of neurotransmitters. At the high-frequency end, the repetitive stimuli further drain the vesicle pools without sufficiently enhancing release probability such that the EPSP amplitude decreases with stimulation frequency.

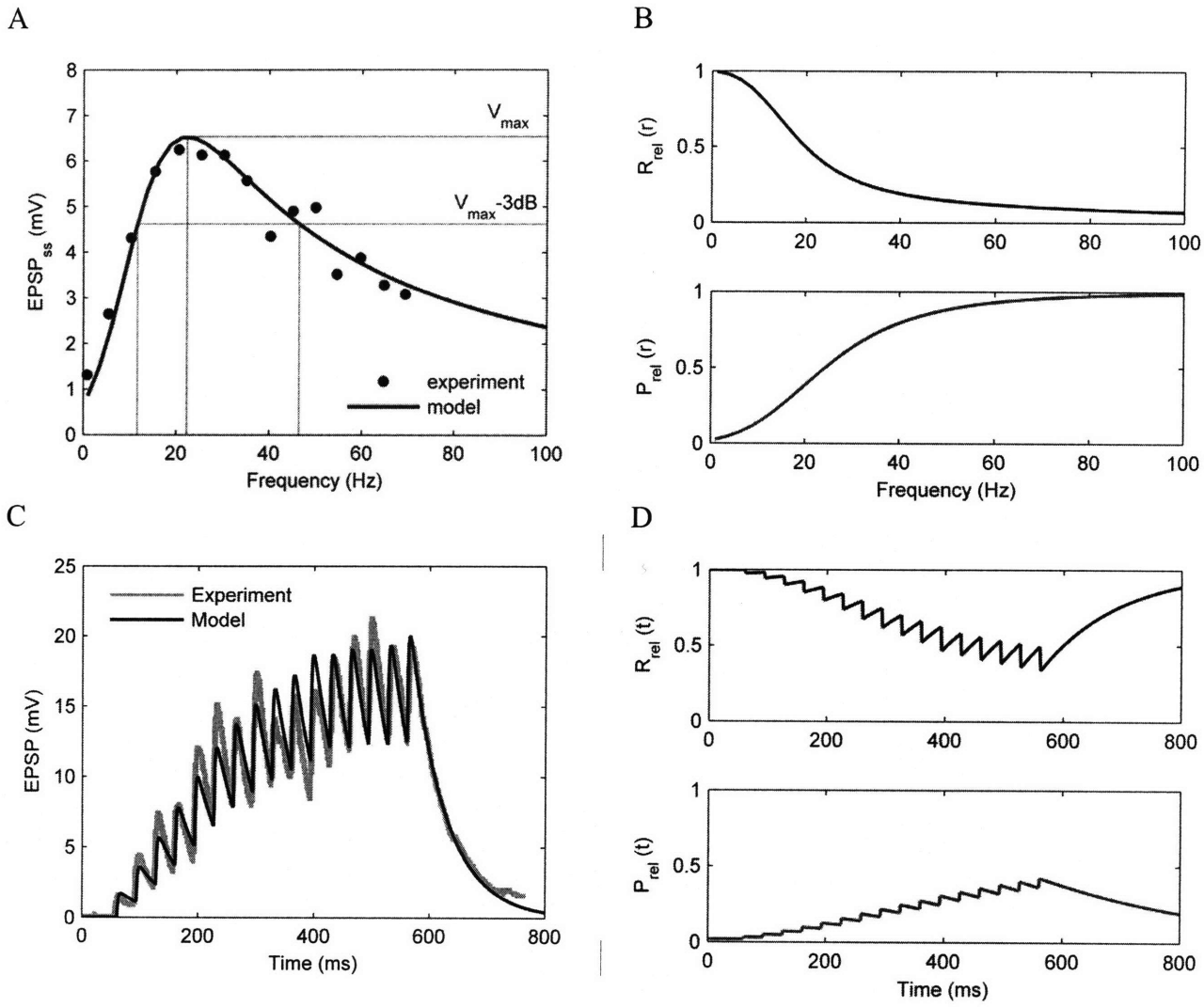

Figure 4-5 Synaptic plasticity in rat pyramidal neurons under mixed effects.
(A) The EPSP as a function of frequency, with maximum and bandwidth labeled. (B) The frequency response of releasable vesicle ratio and release probability by model. (C) The transient EPSP caused by stimuli at 30 Hz. (D) The corresponding transient releasable vesicle ratio and release probability by model. Data source: [106].

Table 4-1 Model parameters for different synapses

Parameters	Definitions	Units	PF to Purkinje (Facilitation)	Calyx of Held (Depression)	Pyramidal neurons (Mixed)
Ca_{i0}	Initial calcium concentration	μM	4.7	5.3	7.5
k_{recov0}	Initial recovery rate constant	ms^{-1}	2.2×10^{-2}	1.0×10^{-4}	7.5×10^{-3}
K_{Ca}	Gain of calcium	$\mu M ms^{-1}$	120	2130	515
$K_{rel,1/2}$	Calcium sensitivity of transmitter release	μM	9.0	4.0	20
$P_{rel,max}$	Maximum release probability	-	0.9	0.6	1
$^{\ddagger}P_{rel0}$	Initial release probability	-	0.06	0.46	0.02
$^{\dagger}r_{resonance}$	Resonance frequency	Hz	39.9	≤0	22.3

$^{\ddagger}P_{rel0}$ is the initial release probability from substituting estimated parameters into Eq. (4.5)
$^{\dagger}r_{resonance}$ is the resonance frequency calculated by using Eq. (4.13).

4.4 Discussion

4.4.1 Determinants of short-term plasticity

We have presented a unifying model that summarizes how some presynaptic factors independently and collectively influence the directionality of short-term plasticity. The resonance frequency, a function of several critical biophysical parameters, is the single key indicator of the propensity for synaptic facilitation or depression under repetitive stimuli. Since it is the optimal stimulation frequency that elicits maximal excitatory response, a high resonance frequency indicates facilitation whereas a low resonance frequency suggests depression in the normal range of stimulation frequencies as labeled in Fig. 6. Thus, our analytical solution of resonance frequency as shown in Eq. (4.13) is valuable in assessing the contributions of specific or multiple biophysical parameters to short-term synaptic plasticity.

The parameters influencing resonance frequency include initial calcium concentration (Ca_{i0}), gain of calcium (K_{Ca}), recovery rate constant (k_{recov}), and calcium sensitivity for release ($K_{rel,1/2}$). From Eq. (4.13), the resonance frequency decreases monotonously with Ca_{i0} and grows with $K_{rel,1/2}$ and k_{recov}. To better visualize the independent effect of each parameter on the resonance frequency, two 2-D perturbation plots are made by varying one independent variable at a time around the condition given in Figure 4-5. To demonstrate the combined effects of model parameters on the resonance frequency, two 3-D multivariate perturbation plots were also obtained by varying two parameters each time. As shown in Figure 4-6A and Figure 4-6B, high Ca_{i0} and high K_{Ca} result in low resonance frequency and a tendency for depression. The reason is that both these factors contribute to high initial release probability (P_{rel0}). This is consistent with the general consensus that high initial release probability predisposes to depression [13, 134]. Figure 4-6C and Figure 4-6D shows that facilitation prevails as the value of k_{recov} gets larger. Synapses with higher recovery rate constants are less likely to get depressed because their releasable vesicles are recycled quickly after stimuli. On the other hand, based on Figure 4-6B, depression arises at the low half occupancy concentration, $K_{rel,1/2}$, which indicates high calcium sensitivity of transmitter release. That is, synapses with releasable vesicles very sensitive to calcium tend to become saturated and depressed easily because further calcium inflow cannot elicit stronger transmitter release. The predicted trend agrees with previous finding that depressing calyx of Held is fairly sensitive to intracellular calcium [7].

Simply stated, the directionality of short-term plasticity depends on the amount of vesicle release caused by each action potential relative to the vesicle recovery rate. As a result, high initial release probability (P_{rel0}) and low recovery rate (k_{recov}) cause depression; opposite conditions may bring facilitation. The initial release probability itself is influenced by calcium concentration and calcium release sensitivity. The estimated parameter values (Table 4-1) from various depressing and facilitating synapses support the concept. First, comparing the initial release probability (P_{rel0}) indicates how rapidly vesicles are consumed. Depressing synapses (calyx of Held) have a much higher value (0.46) than facilitating synapses (PF to Purkinje). In addition, facilitating synapses with recovery rate constants as high as $0.022ms^{-1}$, refill their vesicle pools faster than depressing ones. For synapses demonstrating clear-cut short-term tendencies, this kind of direct comparison is straightforward. However, for synapses that are more ambivalent or those that express mixed-mode facilitation-depression depending on the stimulation frequency, integrative models incorporating critical biophysical parameters such as presently proposed are needed to quantitatively predict the tendency of synaptic plasticity.

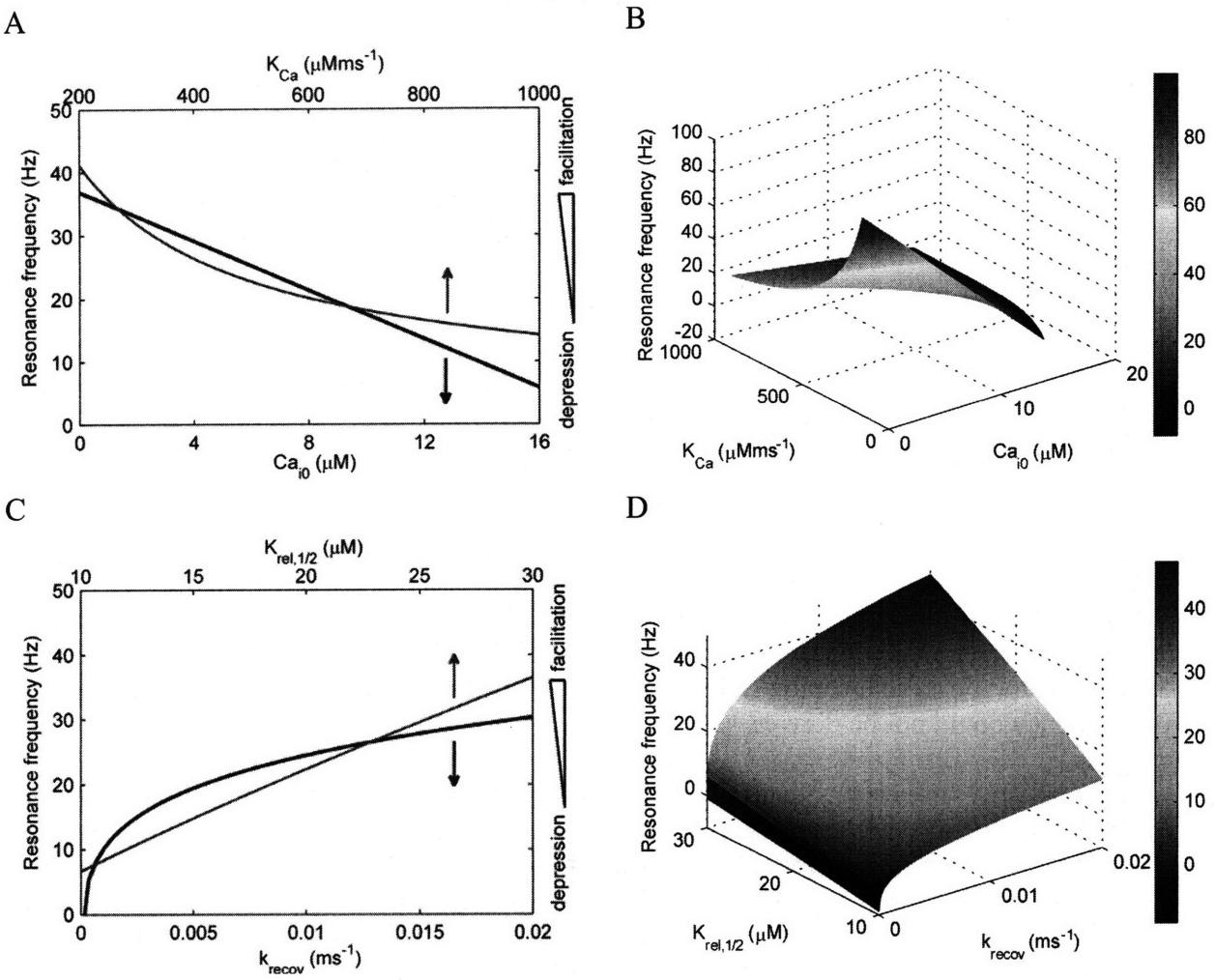

Figure 4-6 Perturbation analysis of resonance frequency as a function of various physiological parameters based on Eq. (4.13).
The vertical arrows indicate the x-axis that each curve belongs to. The color bars indicate the value of resonance frequency at the synapse. (A) The 2-D plot of resonance frequency against initial calcium concentration and gain of calcium current to concentration. (B) The 3-D plot of resonance frequency against initial calcium concentration and gain of calcium current to concentration. (C) The 2-D plot of resonance frequency against recovery rate constant and calcium sensitivity. (D) The 3-D plot of resonance frequency against recovery rate constant and calcium sensitivity.

4.4.2 New experiments suggested by the model for altering short-term plasticity

It is theoretically possible to alter tendency of short-term plasticity by adjusting the parameter values in the kinetic model. Recent studies have validated the possibility of reversing short-term facilitation and depression by manipulating the expression of some presynpatic proteins. For instance, Han et al. [35] compared the expression of hippocampal short-term plasticity in RGS2 (regulator of G protein signaling 2) knockout and wild-type mice. Since RGS2 downregulates presynaptic Ca^{2+} channel inhibition, RGS2 deprivation would leave less calcium flowing into the presynaptic terminal after

each impulse, i.e., smaller K_{Ca}. Our model predicts that synapses with smaller K_{Ca} tend to facilitate (Figure 4-6A), which coincides with the experimental trend [35]. Similarly, Sippy et al. [147] switched the rat hippocampal synapses from pair-pulse depression to facilitation by raising the level of neuronal calcium sensor-1 (NCS-1). Since more calcium sensors means a higher calcium concentration is required to saturate the calcium binding proteins, i.e., higher $K_{rel,1/2}$, our model predicts that the latter should lead to facilitation (Figure 4-6B), which matches the experimental findings.

4.4.3 Comparison with previous models

Table 4-3 summarizes the attributes of this kinetic model in comparison with previous ones. In early studies (listed in the bottom two rows of the table), the classic presynaptic vesicle depletion model was used to follow depression dynamics [157, 175] while calcium-dependent transmitter release was considered to model facilitation [12, 179]. Since these models treated facilitation and depression separately, the number of experimental data that can be fit by each model was limited and an expression of resonance frequency could not be derived.

Three important features distinguish our kinetic model from the other two facilitation-depression models [38, 106]. First, our model is based on biophysical descriptions with measurable physiologic parameters, as opposed to the phenomenological efficacy utilization model. Second, a systematic approach was taken to describe the underlying biochemical reactions in order to explain a broad range of experimental data. By combining previous work with new physiological insights, we were able to integrate more sets of experimental data (in both frequency and time domains of three different synapses) than any previous models. Third, mathematical simplicity was maintained throughout model development to keep the model tractable. The simple and tractable model description makes possible a comprehensive closed-form mathematical solution of the resonance frequency that allows multivariate prediction of short-term plasticity and its dependence on several key biophysical parameters, without the need for complex computer simulation.

In conclusion, compared to previous phenomenological and biophysical models that attempted to integrate experimental data of facilitation and depression, our model is based on essential physiological reaction schemes with closed-form mathematical expressions that are less complex and more tractable, intuitive and predictive than complex computer simulations or abstract phenomenological descriptions.

Table 4-2 Model comparison of this kinetic model with respect to previous ones in terms of several key attributes

	Model type	Underlying Mechanism	Model complexity	Data modeled	Expression of resonance frequency
Kinetic model unifying facilitation and depression	biophysical	calcium-dependent vesicle trafficking	moderate	Six data sets of facilitation, depression & mixed plasticity in time and freq.	available
Synaptic efficacy utilization model [106]	phenomeno-logical	utilization of synaptic efficacy	simple	Two data sets of mixed short-term plasticity in time and freq.	available
Facilitation, depression, and residual calcium model [38]	biophysical	calcium-dependent facilitation and depression	complex	Three data sets of facilitation & depression in freq.	unavailable
Facilitation model [12, 179]	biophysical	enhanced facilitation by residual calcium	simple	Several data sets of facilitation	unavailable
Depression model [157, 165, 175]	biophysical	vesicle depletion	simple	Several data sets of depression	unavailable

4.4.4 Limitations of the model

Model applicability is limited by several simplifying assumptions made. First, the model is deterministic and does not include the stochastic nature of the process. That is, the average profiles of the biochemical species are modeled instead of individual molecules. Since most of the species considered exist in large amount, this assumption is justified. Yet the downside of simple deterministic approach is that the probabilistic distribution of possible outcomes cannot be calculated. In order to estimate the range of possible responses, especially in cases with only small number of molecules, stochastic modeling is necessary.

Second, the assumption of spatially homogeneous intracellular calcium is apparently a simplification. In fact there are many intracellular organelles such as mitochondria and endoplasmic reticulum that can store and release calcium. In addition, the calcium concentration is highly localized and there can be signficant calcium concentration gradients within the cytoplasm [7, 129]. Yet within the time range of a few seconds, the release or storage of calcium by organelles is probably insignificant compared to the calcium influx due to stimuli. Besides, the first-order delay equation used to model calcium buffering effects does take into account the loss of calcium by diffusion and pumping. Therefore, it roughly describes the dynamics of intracellular calcium near release sites within a short period of time. In order to extend the model to address pre- or post-synaptic long-term potentiation and depression, it may be necessary to take into account the detailed spatiotemporal effects of calcium signal transduction and buffering.

Finally, we have mainly considered presynaptic vesicle depletion and residual calcium [177] yet postsynaptic reactions may also influence short-term plasticity. For instance, the desensitization of postsynaptic receptors causes depression [159] and activation of postsynaptic calcium channels might increase synaptic strength [5]. To distinguish the pre- and postsynaptic effects, in addition to tracking EPSC and EPSP, measuring the dynamic response of neurotransmitter release may be necessary.

Table 4-3 The summary of nomenclature in Chapter 4

Symbols	Units	Definitions
Ca_i	μM	Intracellular calcium concentration
Ca_{i0}	μM	Initial intracellular calcium concentration after resting
$Flux_{Glu}$	# ms^{-1}	The flux of glutamate release
Glu	#	The number of glutamate molecules as neurotransmitter
I_{Ca}	Hz	Inflow calcium current as Dirac Delta function
k_{recov}	ms^{-1}	Recovery rate from empty to releasable state
$k_{recov,min}$	ms^{-1}	Minimum recovery rate from empty to releasable state
$k_{recov,max}$	ms^{-1}	Maximum recovery rate from empty to releasable state
$k_{recov,ss}$	ms^{-1}	Steady state recovery rate from empty to releasable state
K_{Ca}	μMs^{-1}	Intracellular calcium gain caused by calcium current
K_{Glu}	μMs^{-1}	Glutamate concentration gain caused by influx of glutamate
$K_{rel,1/2}$	μM	Calcium sensitivity regarding transmitter release
$K_{recov,1/2}$	μM	Calcium concentration giving one half recovery rate
n	#	Number of glutamate released per vesicle
n_{Hill}	-	Hill coefficient of transmitter release caused by calcium
N_p	#	Number of stimulus impulses
N_{rel}	-	Number of vesicle releasable at active terminals
N_{empty}	-	Number of empty vesicle at active terminals
N_{total}	#	Total number of vesicle per synaptic terminal
P_{rel}	-	Probability of release
$P_{rel,0}$	-	Initial probability of release
$P_{rel,max}$	-	Maximum probability of release
$P_{rel,ss}$	-	Probability of release at steady state
r	Hz	Frequency of stimuli
$r_{resonance}$	Hz	Resonance frequency of stimuli that causes max responses
R_{rel}	-	Remaining ratio of vesicles releasable
$R_{rel,ss}$	-	Remaining ratio of vesicles releasable at steady state
τ_{Cai}	ms	Time constant of calcium buffering
τ_{EPSC}	ms	Time constant of EPSC decay

5 Modeling Long Term Plasticity

Long term synaptic plasticity refers to the modification of synaptic strength lasting longer than hours or days. It is generally accepted as the principal mechanism underlying learning and memory. Thus, its abnormality is suspected to cause dementia, and other memory-related neurological diseases. Bistable biomolecular switches have been proposed as the prerequisite conditions for inducing long lasting neuronal connectivity. We have developed a calcium entrapment model that includes the interacting dynamics of NMDA receptors, calmodulin kinase, and protein phosphotase. The model was sufficient to explain the induction of long term plasticity by tetanus stimuli without incorporating any bistability component. In addition, spike timing dependent and frequency dependent plasticity can be explained by the elevated level of calcium concentration in postsynaptic compartment.

Long term potentiation (LTP) and depression (LTD) are generally regarded as the principal mechanism underlying learning and memory. Most synapses show LTP or LTD which can last for more than hours after tetanus stimuli are applied and removed. They involve multiple pathways with different time scales so more complexity is included in the postsynaptic reaction schemes as shown in Figure 4-2A.

5.1 Current understanding of long term plasticity

There are hypotheses explaining the long lasting change in synaptic strength after high frequency stimuli. Most of these studies suggested that bistable switch is a necessary mechanism to long lasting change [14, 119, 176]. The reaction schemes proposed usually involve MAPK (mitogen-activated protein kinase) and PKC (protein kinase C) pathways. The bistable switches require precise tuning of the species concentrations. There exist only two levels of steady state response: one at the initial concentration and the other at an elevated level corresponding to another steady state. Yet this kind of response does not reflect the fact that many responses of the long term potentiation are graded.

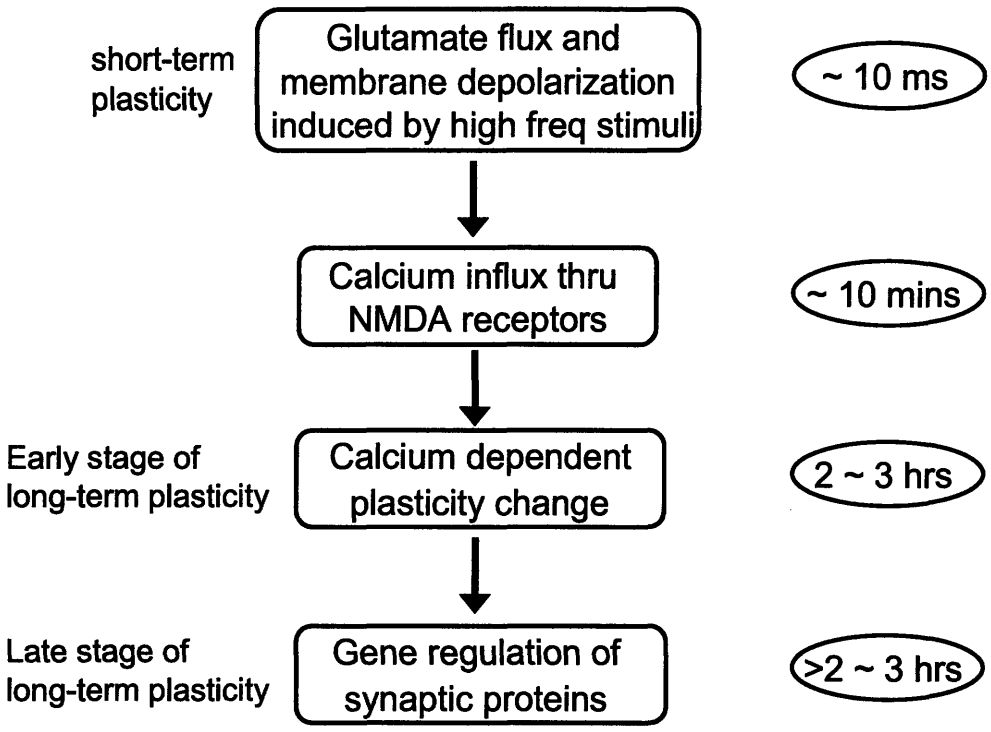

Figure 5-1 The overview diagram of short-term and long-term plasticity

5.2 Brief review on bistable models

Bistability in general indicates a phenomenon that something can rest stably in one of the two equilibrium states. An example graphical representation is shown in Figure 4-1A generated from a quadratic function: $V(x,y) = 1.5y^2 - 1.5x^2 + 0.1x^4$. At steady state, an object will be located in either one of the two concaves.

5.2.1 Bistability in mathematics

Mathematically a function is bistable if there exist two stable states (minimum points) separated by the energy barriers (saddle points). The general formula of ordinary differential equations is $\underline{x}' = f(\underline{x})$ on which steady state analysis can be performed to determine the stability. The initial conditions are crucial to determine the final resting state of the system. Also both the duration and amplitude of stimuli need to be considered in predicting the equilibrium state.

For instance, the following quadratic function demonstrates bistable behavior. $V(x)$ is the potential function and varies with position variable x as depicted in Figure 4-1B.

$$V(x) = -\frac{a}{2}x^2 + \frac{b}{4}x^4 \tag{5.1}$$

We can perform the steady state analysis by taking the derivative of Eq. (5.1) and factorizing the function. The location of the minimum points x_{min} can be found at $+\sqrt{a/b}$ and $-\sqrt{a/b}$ with the corresponding amplitude of the barrier ΔV equal to $a^2/4b$.

$$V'(x) = bx^3 - ax = b \cdot x \cdot \left(x^2 - \frac{a}{b} \right) = b \cdot x \cdot \left(x + \sqrt{\frac{a}{b}} \right) \cdot \left(x - \sqrt{\frac{a}{b}} \right) \tag{5.2}$$

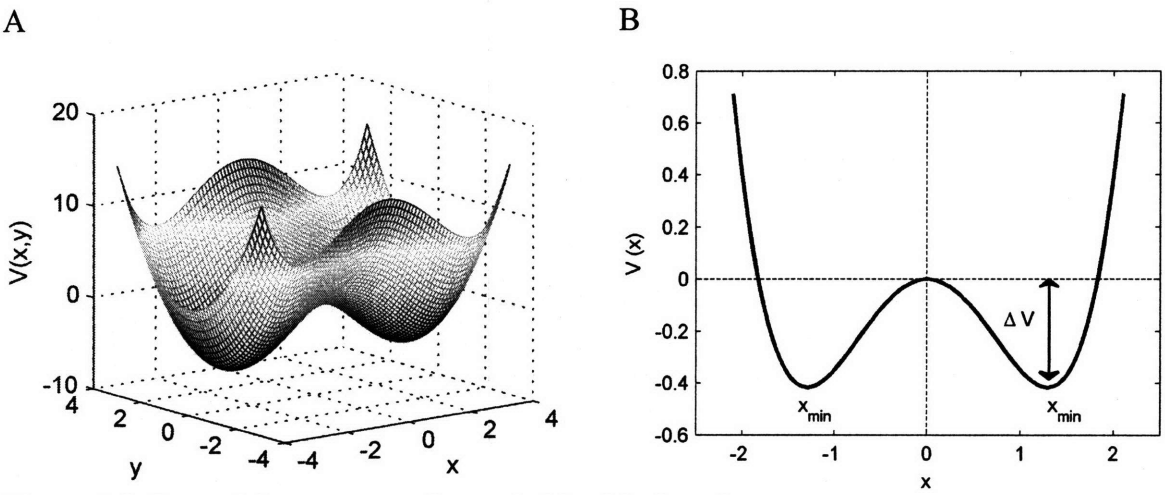

Figure 5-2 Potential responses of generic bistable functions.
(A) The 3-D plot of a quadratic bistable function: $V(x,y) = 1.5y^2 - 1.5x^2 + 0.1x^4$. (B) The 2-D plot of the function: $V(x) = -0.5x^2 + 0.15x^4$.

5.2.2 Bistability in biology

The bistable switch has been found in several biological systems and in most cases, positive feedback is the necessary condition. In this section, we include two example systems: one involves gene translation regulated by a DNA binding protein acting as activator [42] and the other is an example of signal transduction [176]. Yet the model expressions of these two systems eventually boil down to very similar mathematical formulation. First, as shown in Eq. (5.3) and Figure 5-3A, the activator is stimulated linearly by signal S and is degraded following first order reaction. Also it activates the gene translation through second order Hill equation where K_A is ligand concentration producing half occupation. The fixed values of parameters used in their research were: $k_1 = 1$, $k_2 = 1$, $k_3 = 1$, $n = 2$, $K_A = 1$, and $k_{inact} = 0.01$. With the differential equation defined and values of parameters fixed, can be integrated and analyzed later to get the bistable responses.

$$\frac{d[activator]}{dt} = k_1 S - k_2[activator] + \frac{k_3[activator]^n}{K_A{}^n + [activator]^n} \tag{5.3}$$

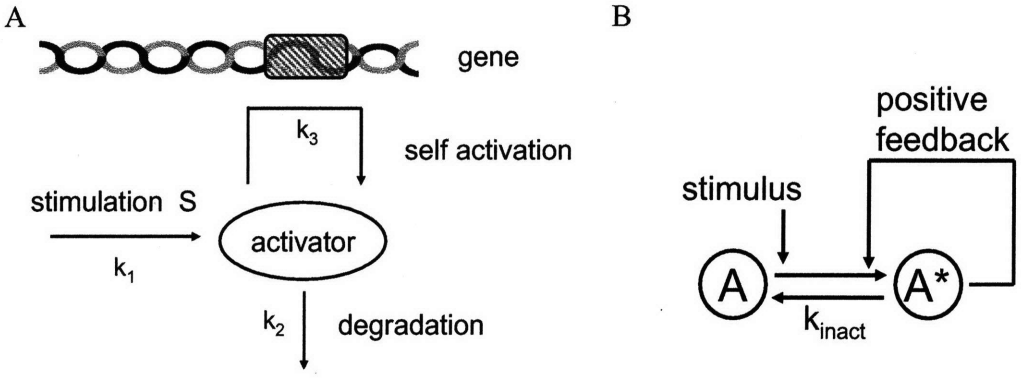

Figure 5-3 Examples of bistable systems in biology.
(A) The system of gene translation. (B) The system of molecular signaling.

The second example is the molecular signaling with positive feedback loop as in Figure 5-3. According to the model by Xiong and Ferrell, 2002, the enzyme A is assumed to exist in two forms: active (A^*) and inactive (A) with the total concentration equal to A_{total}. The external stimulus can trigger the conversion from A to A^*; also the active form of enzyme degrades back to inactive form following first order kinetics. There is also positive feedback action by A^* to trigger more of its own production which can be modeled by n-th order Hill equation. Overall the rate of change in A^* based on material balance is shown in Eq. (5.4).

$$\frac{dA^*}{dt} = stimulus \cdot (A_{total} - A^*) + V \cdot \frac{A^{*n}}{K_A{}^n + A^{*n}} - k_{inact} A^* \qquad (5.4)$$

After the rearrangement, the ordinary differential equation becomes Eq. (5.5) which is very similar in formulation with Eq. (5.3). Therefore, we use Eq. (5.3) only in analyzing the bistability response to avoid redundancy.

$$\frac{dA^*}{dt} = stimulus \cdot A_{total} - (k_{inact} + stimulus) \cdot A^* + V \cdot \frac{A^{*n}}{K_A{}^n + A^{*n}} \qquad (5.5)$$

Two kinds of analyses are usually done to check the bistability of a given system: one is the stimulus-response analysis and the other involves checking the steady state solution. To perform the stimulus-response analysis, the signal S term in Eq. (5.3) was represented by a signal train of stimuli to potentially switch the system from one state to the other (Figure 5-4A). The steady state level of activator concentration finally reached is as high as four, and this value agrees with the results of the steady state analysis. As shown in Figure 5-4B, there are three zero crossing points representing steady state solutions of the activator concentration. Yet only two of them are stable solutions: zero and four which correspond to the two steady levels in Figure 5-4A.

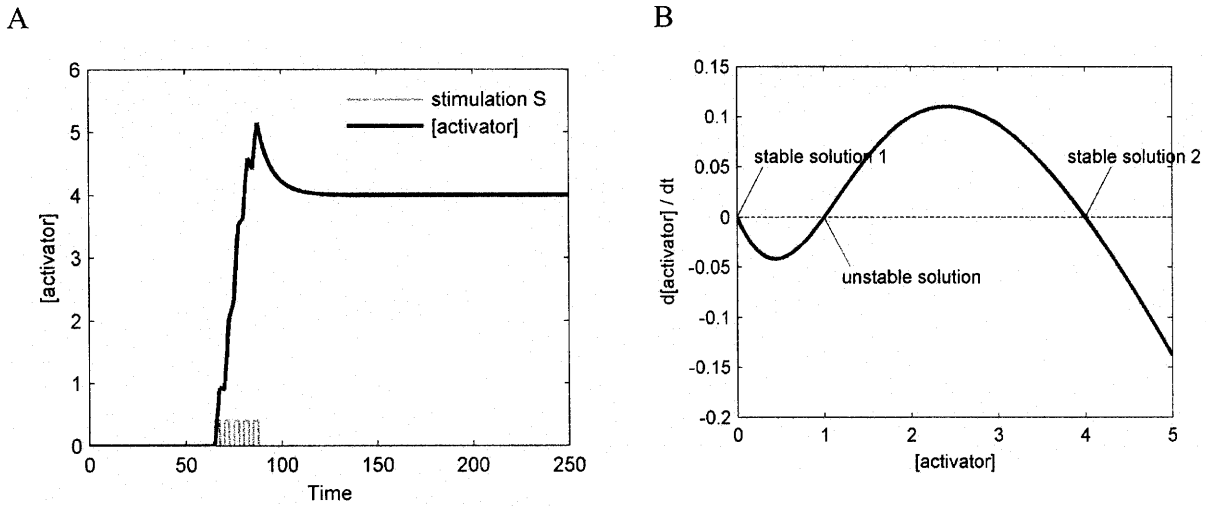

Figure 5-4 Output from a biological bistable switch.
(A) The transient response of the activator concentration given a single train of stimuli.
(B) The analysis plot of the system.

The special feature of bistable response is the long lasting change of response level. Given the values of parameters are tuned properly, the response can latch from one state to the other and stay there for long even after the stimuli no longer exist. Figure 5-4A does appear very similar to many long term potentiation (LTP) responses trigger by a single train of stimuli [20, 41]. It is this feather that makes bistability one of the leading hypotheses to explain long term change in synaptic plasticity.

Yet there is discrepancy between experimental results of LTP and modeling output of bistable systems in the case of multiple trains of stimuli [44]. As shown in Figure 5-5, two trains of stimuli are applied to the system. After the first train, the level of activator concentration latches to four, one of the stable equilibrium states. Yet even with the application of the second stimuli train, the final concentration level remains the same. This is another feature of the bistable system as its name implies. The number of stable steady states is just two. Therefore, even if the further stimulation is applied, the system still returns to the same steady state level. This feature, however, contradicts with many experimental results of LTP which show continuous and graded responses after application of multiple stimuli trains [44]. This discrepany will be discussed further in the later section of model development. There we consider calcium entrapment at postsynapse to better explain the physiology of long term potentiation and the measured responses triggered by multiple trains of stimuli.

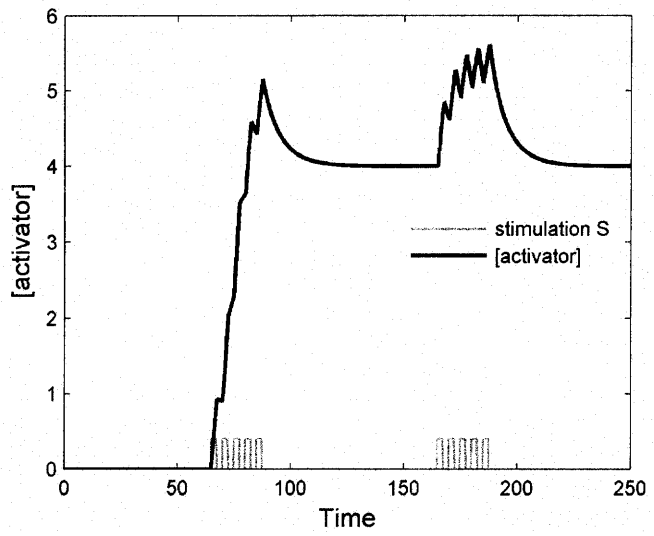

Figure 5-5 The transient response of the activator concentration triggered by two stimuli trains according to the bistable switch model.

5.2.3 Bistability in other systems

There are other systems that demonstrate bistability. The most recognized one is the bistable switch built from electrical circuits [166] and the one well known in chemical reaction engineering is the bistable behavior of exothermic reactions in mixed flow reactors [94]. Bistable switches, also called flip-flop and latches and are the basic memory units. Two inverter gates and OR gates are needed respectively to construct a simple bistable switch. Positive feedback is the key component for setting up the bistable circuit. There are two stable states that the system can take on and the exact final resting state depends on the history of the activities [166]. As for the chemical reactor systems, the operation conditions are determined by the analysis results of mass balance and energy balance. For exothermic reactions in mixed flow reactors, the material balance curve may appear S-shaped while the energy balance is a straight line on a conversion versus temperature plot. If there are three crossing points or solutions of mass and energy balances, bistable behavior will show. The three crossing points are called the unreacted state, the reacted state, and the ignition point. Under such circumstance, a small turbulence in feed condition may cause the reactor to jump between the two stable states [94]. Even though bistable behaviors appear in a number of systems, they share the same attribute which is the existence of two stable states. This attribute, however, does not match the response of long term plasticity well. Therefore, alternative reaction schemes need to be developed to resolve the discrepancy between experiments and models.

5.3 Model development of long term plasticity

To resolve the disagreement, we decided to reexamine the relevant reaction pathways at synapse. The systems of interest consist of presynaptic and postsynaptic compartments. Even though a few studies have found some contribution to LTP by presynapse, the mechanism of long term plasticity is generally attributed to postsynaptic reactions. Since

NMDA receptors gating calcium inflow at postsynaptic membranes can only be activated through substantial depolarization, we suspected calcium signaling is the most important factor in causing LTP. There were also studies suggesting intracellular calcium is sufficient and necessary to induce change in long term plasticity [29, 180]. Hence, we developed a calcium entrapment model to simulate the change in excitatory response after stimulation. The systematic model consists of equivalent electrical circuits as well as ligand- and voltage-gated NMDA receptors. This built model is supported by a broad range of experimental measurements. According to the result of model differentiation, we confirmed that calcium entrapment model explains graded response of synaptic LTP better than biostability mechanism.

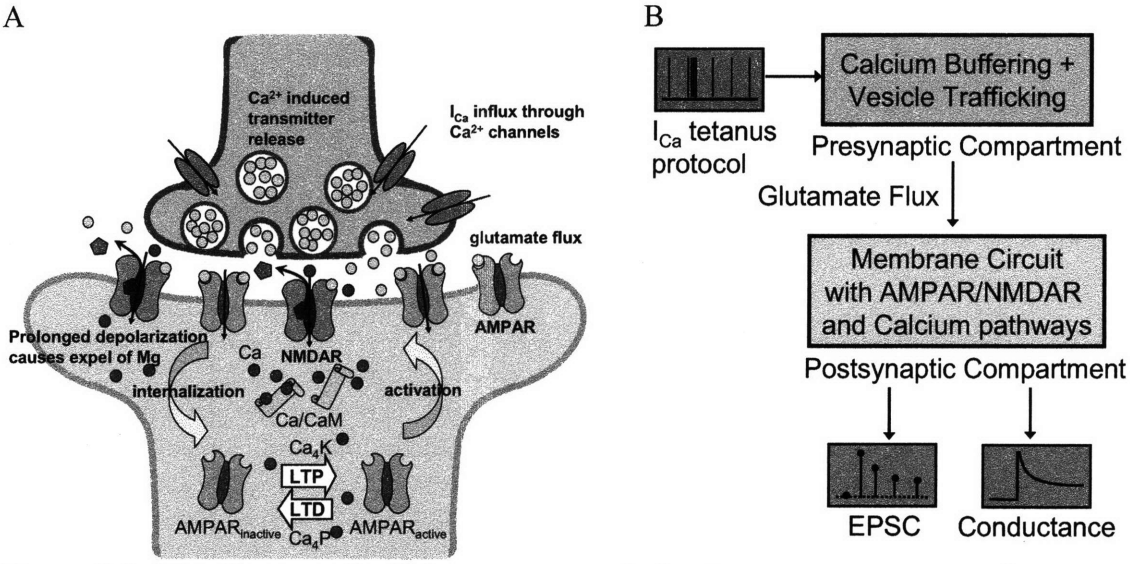

Figure 5-6 The diagram of cellular structure and signal process at synapse relevant to short-term plasticity.
(A) The signal transmission pathways of long-term plasticity at synapses. (B) The summary of corresponding systems and signals in our study.

5.3.1 Dual regulation of NMDA receptors by membrane potential and glutamate

Activities of NMDA receptors influence long term plasticity change through regulation of calcium inflow. The conductance of NMDA receptors (g_{NAMDAR}) depends not only on glutamate concentration (Glu) but also on membrane voltage (V_{dent}). The voltage dependence results into selective signal transmission and has been modeled with the logistic function as shown in Eq. (5.6) (Jahr, 1990) [74]. The voltage dependent activity function rises to a maximum ($g_{NMDARmax}$) following a sigmoidal curve with half way voltage equal to $V_{1/2}$ and slope as large as $0.5k_{NMDA}$ at that point. Then ligand-receptor model with association constant K_{Glu} is adopted to describe glutamate dependence. Glutamate concentration can be related back to the presynaptic stimuli (I_{pre}) by a simple two compartment model; the details are described in supplemental materials. Finally, the expression of g_{NMDAR} (V_{dent}, Glu) can be inserted into equivalent circuits to calculate EPSP.

$$g_{NMDAR}(V_{dent}, Glu) = \frac{g_{NMDARmax}}{1+e^{-k_{NMDA}(V_{dent}-V_{1/2})}} \cdot \frac{Glu}{Glu+K_{Glu}} \tag{5.6}$$

The total amount of calcium (CaT) flowing into postsynapse is proportional to the integration of current flow through NMDA receptors over the time of stimuli. Based on Ohm's Law, I_{NMDAR} can also be expressed as the product of conductance (g_{NMDAR}) and dendrite membrane potential (V_{dent}). Furthermore, depending on the total amount, calcium inflow may either up- or down-regulate signal transduction pathways and lead to synaptic plasticity change.

$$CaT \propto \int_{stimuli} I_{NMDAR} dt = \int_{stimuli} g_{NMDAR} V_{dent} dt \tag{5.7}$$

5.3.2 Calcium dependent plasticity regulated by kinase and phosphatase

It is likely that the temporary change in steady state level is due to the entrapment of intracellular calcium. As we proposed in Eq. (5.8), most calcium ions entering postsynapse through NMDAR which allows unidirectional flow. The entrapped calcium can exchange easily with that at intracellular store, mainly endoplasmic reticulum. Also calcium binds with calmodulin and tends not to leak out during typical experimental time. That is the inversion of rate constant k_{leak}, is much larger than hundreds of minutes.

$$\begin{aligned} &I_{NMDAR} \xrightarrow{K_{Ca}} Ca \underset{k_{out}}{\overset{k_{in}}{\rightleftharpoons}} Ca_{store} \\ &Ca \xrightarrow{k_{leak}} Ca_{out} \end{aligned} \tag{5.8}$$

Accordingly, the time derivative of calcium concentration and that at intracellular store can be represented in the following equation. We omit the effects of binding between calcium and proteins on total calcium concentration, because calcium concentration is much larger than that of further downstream proteins.

$$\frac{d}{dt}\begin{pmatrix} Ca \\ Ca_{store} \end{pmatrix} = \begin{pmatrix} -(k_{leak} + k_{in}) & k_{out} \\ k_{in} & -k_{out} \end{pmatrix} \cdot \begin{pmatrix} Ca \\ Ca_{store} \end{pmatrix} + K_{Ca} \begin{pmatrix} I_{NMDAR} \\ 0 \end{pmatrix} \tag{5.9}$$

Eq. (5.9) is a two-state system of linear ordinary differential equations (ODEs). The current through NMDA receptor (I_{NMDAR}) is the only source of input. This system of ODEs can be solved analytically and the solution of both state variables can be represented by the sum of two exponential functions [120].

The concentration of Ca is plotted as a function of time in Figure 5-7A while the analogy of simple plumbing system is drawn in Figure 5-7B to visualize the idea. Application of high frequency stimuli cause [Ca] to surge drastically. Then it decreases quickly due the rapid exchange with intracellular calcium store (Ca_{store}). Afterwards, the leakage causes calcium concentration to decrease but not very noticeable within tens of minutes. Overall the profile appears similar to that of typical LTP response.

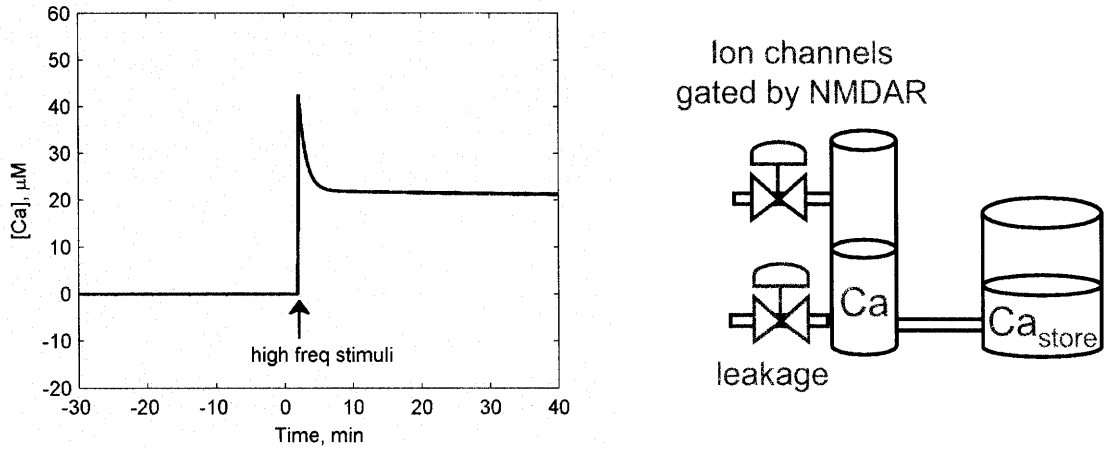

Figure 5-7 (A) The generic response of two-exponential decay. (B) The simple conceptual analogy plot of plumbing with valves to visualize the proposed calcium entrapment model.

After flowing into the postsynaptic compartment, calcium binds with calcium dependent kinase (K) and phosphatase (P), respectively. It has been found that four calcium ions are required to activate either K or P, and the binding is cooperative. The calcium dependent protein kinase (Ca_4K) once being activated can also phosphorylate other proteins. Meanwhile, binding to calcium activates protein phosphatase, which may dephosphorylate downstream enzymes [103].

$$\begin{aligned} 4Ca + K &\underset{k_{CaKb}}{\overset{k_{CaKf}}{\rightleftharpoons}} Ca_4K \\ 4Ca + P &\underset{k_{CaPb}}{\overset{k_{CaPf}}{\rightleftharpoons}} Ca_4P \end{aligned} \tag{5.10}$$

The dynamics of calcium, kinase, and phosphotase expressed in chemical reactions can be converted into a set of ordinary differential equations. The concepts of material balance and chemical reactions are used in conversion.

$$\begin{aligned} \frac{dCa_4K}{dt} &= k_{CaKf}\frac{Ca^4}{Ca^4 + K_{CaK}^4} - k_{CaKb}Ca_4K \\ \frac{dCa_4P}{dt} &= k_{CaPf}\frac{Ca^4}{Ca^4 + K_{CaP}^4} - k_{CaPb}Ca_4P \end{aligned} \tag{5.11}$$

The mobilization of AMPA receptors depend upon the concentrations of both activated kinase Ca_4K and protein phosphatase Ca_4P. Calcium kinase contributes to the insertion of more AMPA receptors to postsynaptic membrane, which was hypothesized as the mechanism of LTP. Other the other hand, calcium protein phosphatase may internalize AMPA receptors and cause long term depression (Bear, 1996).

$$AMPAR_{inactive} \underset{k_{AMPARb}+V_{CaP}CaP}{\overset{k_{AMPARf}+V_{CaK}CaK}{\rightleftharpoons}} AMPAR_{active} \tag{5.12}$$

5.3.3 The conceptual modeling of gene expression

The permanent change of synaptic plasticity can only be realized by protein synthesis regulated by gene expression. The protein that most directly contributes to the synaptic conductance is AMPA receptor. Yet due to the difficulty in quantifying the transcription and translation reactions, not many sets of experimental data are available that reveal step-by-step procedures of permanent plasticity formation. At this stage of research, it is known that calcium pathway, cAMP (Cyclic adenosine monophosphate) pathway, and CREB (cAMP response element-binding) are crucial in strengthening long term plasticity. Therefore, the strategy we took was to propose a general integration model. According to the model, new experiments are suggested as well. Afterwards, the validity of the model can be checked and details of it can be further expanded by the results of proposed experiments.

Figure 5-11A visualizes the proposed reaction schemes of long-term plasticity. Although two essential pathways, cAMP and calcium signaling cascades, contribute to the activation of CREB, we focus on the second one only for simplicity. In the beginning, the stimuli pass onto the calcium or calcium complex through the calcium entrapment model. Then the entrapped calcium leads to the transient increase in the concentration of CREB. At the end, the gene translation of synaptic protein, AMPA receptor, activated by CREB consolidates memory formation (Eq. (5.13)). The synthesis rate of AMPAR by translation ($AMPAR_{syn}$) is modeled by fourth order Hill equation as shown in Eq. (5.14) and Figure 5-11B.

$$I_{stimuli} \rightleftharpoons Ca \rightleftharpoons \ldots\ldots CREB \xrightarrow{k_{gene}} AMPAR_{syn} \tag{5.13}$$

$$\frac{dAMPAR_{syn}}{dt} = k_{gene}\frac{CREB^4}{CREB^4 + K_{Hill}^4} \tag{5.14}$$

Eventually, the total concentration of AMPAR would be equal to the original AMPAR plus the newly synthesized $AMPAR_{syn}$. The simulation results based on our proposed model are discussed in the following section.

$$AMPA_{total} = AMPA + AMPA_{syn} \tag{5.15}$$

5.4 Modeling results

The results from three protocols were modeled. The first one is applying multiple trains of high frequency tetanus stimuli and the second one is the frequency-dependent long-term plasticity. Then the third one is the prediction based on the gene expression model we proposed.

5.4.1 Applying trains of high frequency stimuli

Long term potentiation by single train tetanus stimuli can be fit by both bistable switch model and our calcium entrapment model. The reason is that for single train stimuli, the resultant response only demonstrates two levels of steady states. As the name of bistable model suggests, there exists two levels of steady states, which can match the LTP response by single train stimuli.

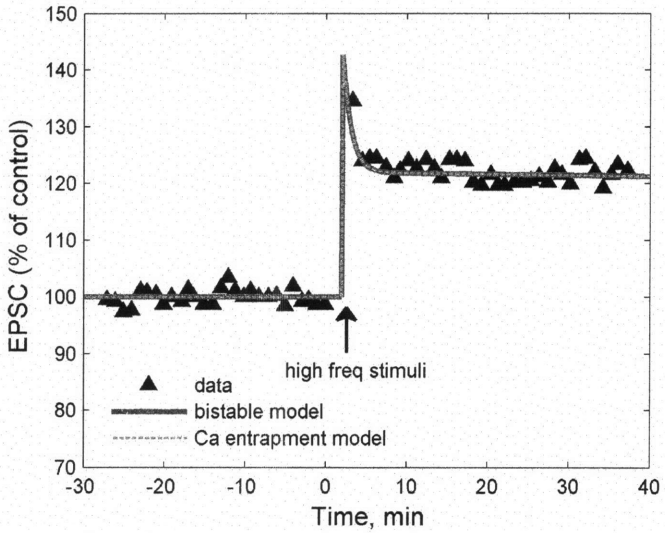

Figure 5-8 The comparison between LTP data and two competing models.
Only a single train of stimuli was applied. Data source: Dudek and Bear, 1992 [41].

However, the response caused by multiple trains of stimuli is graded and is applicable for model differentiation. As shown in Fig. 2, multiple train stimuli lead to further increase in the level of synaptic strength. The graded response cannot be explained by the zero or one bistable model but can be well matched by the continuous built up of calcium.

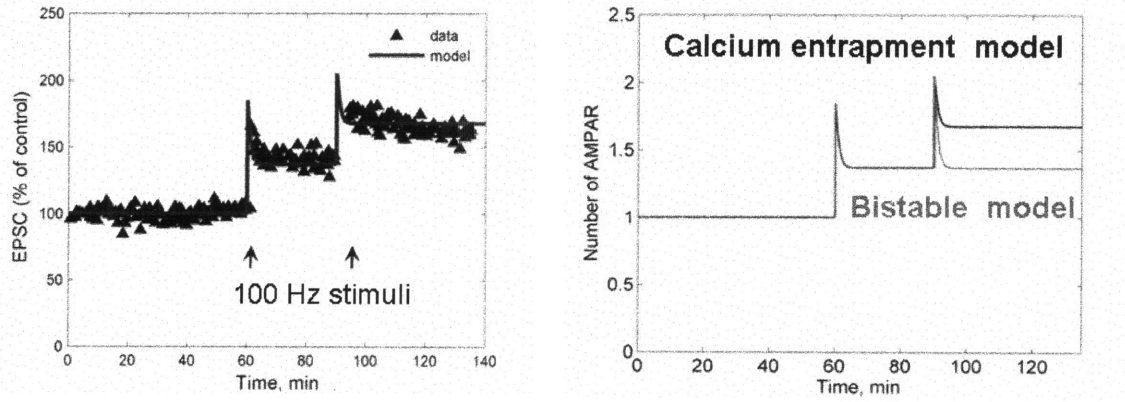

Figure 5-9 The model discrimination for long term plasticity based on graded LTP response.
(A) The fitting between experimental data and calcium entrapment model. Data source: English and Sweatt, 1997 [44]. (B) Comparison between responses of calcium entrapment model and bistable model.

5.4.2 Frequency-dependent plasticity

Most research has focused upon long term potentiation since Bliss and Lomo discovered the high tetanus stimuli experimental protocol. Yet neuroscientists had been speculating the existence of long term depression. It was not until the work by Dudek et al. [41] got published in 1992 that researches realized the determining effects of stimuli frequency on the directions of long term plasticity.

The typical response of rate dependent synaptic plasticity is as shown in Figure 5-10. If the synapses were to follow the bistability mechanism for retaining long lasting change in plasticity, the amplitude of the change in plasticity would only switch between two levels. By contrary, the experimental responses show multiple levels of steady state synaptic plasticity possible. This is another evidence that bistable model cannot match graded experimental responses.

According to calcium entrapment model, higher frequency stimuli cause more calcium influx to the postsynaptic compartment. The two-component model in the Chapter 6: Modeling Spike Timing Dependent Plasticity explains rate dependent plasticity as the result of calcium entrapped in postsynapse and the subsequent signaling trasduction. The results show different levels of calcium concentration can result into multiple values of post stimuli steady state synaptic plasticity. More specifically, low calcium concentration causes long-term depression. On the other hand, once the calcium concentration surpasses certain threshold, long-term potentiation will prevail as shown in Figure 5-10. Modeling algorithms and results are included in Section 6.3.1 and Section 6.3.1, respectively.

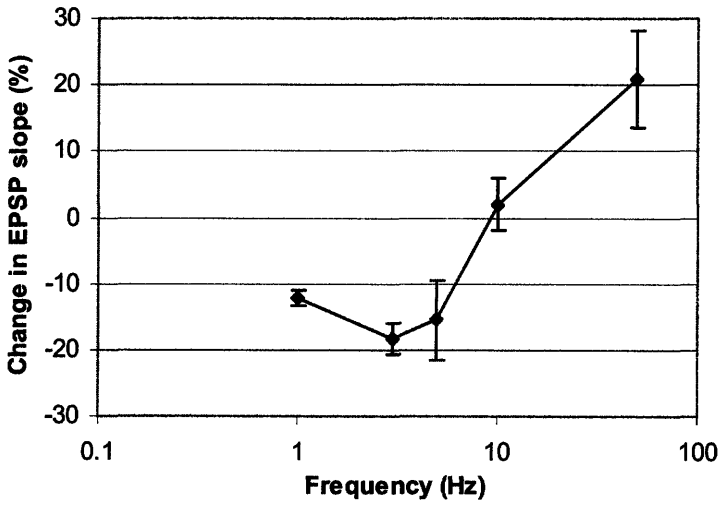

Figure 5-10 The typical response of rate dependent synaptic plasticity. Data source: Dudek et al., 1992 [41].

5.4.3 Results of gene expression modeling

As shown in Figure 5-11C, the signals of upstream species tend to last shorter while those of downstream species can sustain longer. It is likely that the intermediate reactions are to maintain the traces after stimulation so that further downstream gene expression can be initiated. According to the integration model proposed, if the concentration of CREB surpasses the threshold value, synaptic proteins will be synthesized. In addition, there is no consumption term for the synthesized AMPA receptors. This is the reason for long lasting change in synaptic plasticity even after the stimuli are removed. Original AMPA receptor concentrations rise due to stimuli but decay throughout the

As for further development, we suggest two new experiments. The first one is to track the concentrations of intermediates such as calcium kinase to determine the time span of their actions. With the results of the new experiments, more information regarding the subsystems can be obtained in additional to stimuli current as the only input and synaptic conductance as the only output. The second is to decide the quantitative relationship between CREB concentration and protein synthesis rate of AMPA receptors to test the applicability of Hill equation. Finally, detect the decomposition rate of synthesized proteins to examine the hypothesis of no significant consumption.

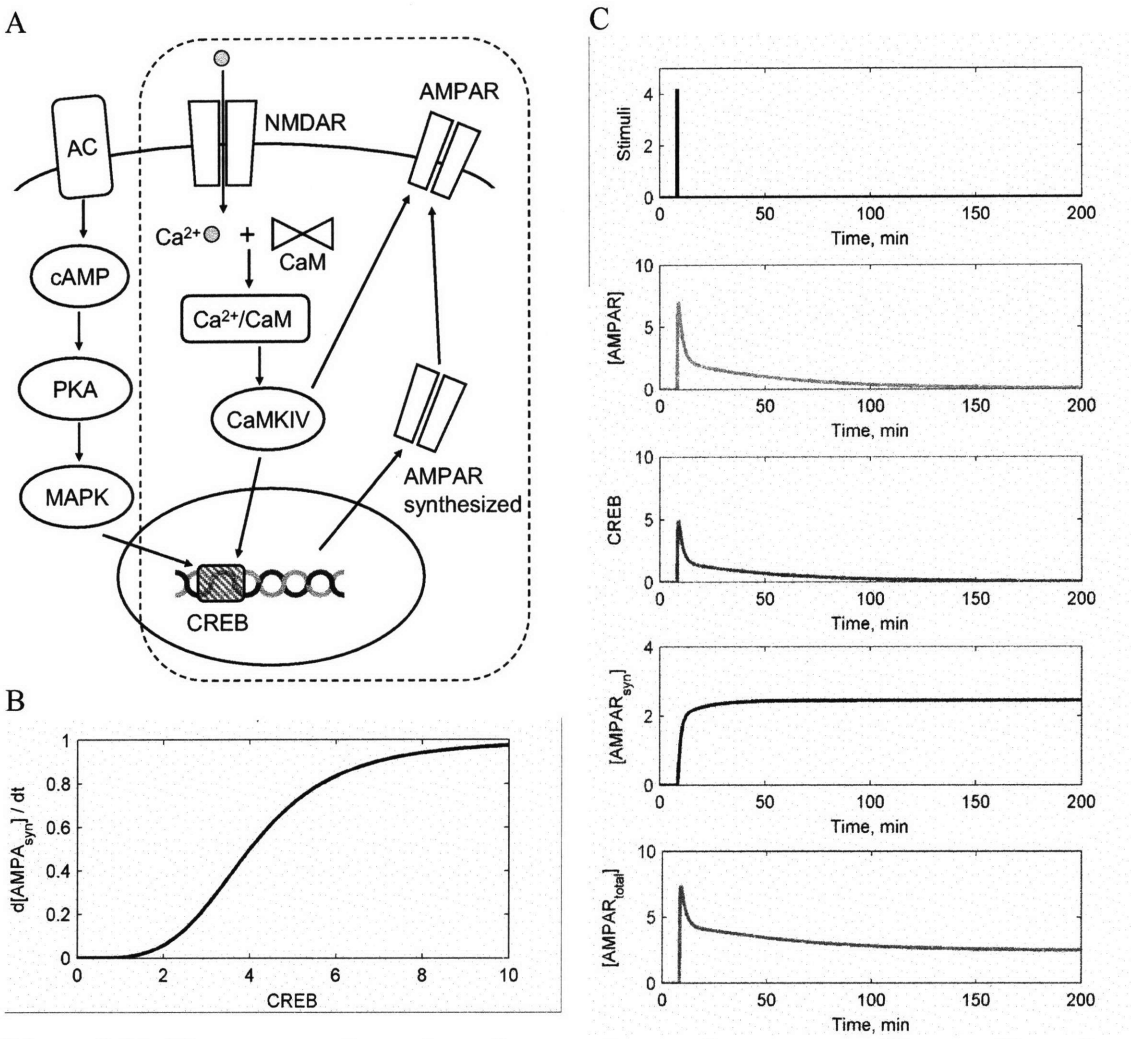

Figure 5-11 The conceptual reaction scheme and example responses of intermediates that lead to translation of synaptic protein.
(A) cAMP and calcium signaling pathways are the two major contributors to synaptic protein synthesis. We focus on calcium signaling pathway which is enclosed in dash line. CaMKIV: calmodulin kinase IV. AC: adenylate cyclase. PKA: protein kinase A. MAPK: mitogen-activated protein kinase. (B) The dependence of protein translation rate on CREB modeled by Hill equation. (C) The concentrations of intermediates belonging to calcium signaling pathways. Note that downstream intermediates tend to last longer.

5.5 Conclusion of long-term plasticity

The induction of long term potentiation by tetanus stimuli involves several subsystems interacting with one another. The frequency dependence is the result of cumulative calcium and calcium dependent synaptic plasticity. Even thought bistable models have been proven useful in explaining cell fate decision or cell differentiation, the memory formation process is unlikely to follow such mechanism. The main reason is bistable systems demonstrate discrete instead of continuous behavior which is contradictory to common memorization processes. The strength of macroscopic memory or microscopic synaptic plasticity varies with respect to the intensity and frequency of external stimuli. It is very likely that the final equilibrium state of biological memory can rest on continuous levels instead of just zero and one as bistable models suggest.

6 Modeling Spike Timing Dependent Plasticity

Spike timing dependent synaptic plasticity (STDP) refers to the general phenomenon that the efficacy of synaptic transmission is influenced by the relative timing between presynaptic and postsynaptic spikes. STDP is regarded crucial because it validates and expands Hebbian theory, the most influential neurological learning rule. It has also become a principal experimental protocol for inducing change in synaptic plasticity; hence, quite a variety of STDP responses were reported before and are classified in this study. By comparison, the theoretical work of STDP is underdeveloped since few biophysical models can reasonably answer why temporal asymmetry arises, let alone unify different subtypes of STDP reported. We propose a unified model consisting of three essential parts: backpropagation of action potentials, dual requirement of N-methyl-D-aspartate (NMDA) receptors, and calcium dependent plasticity. First, the shapes of action potentials at synapses are carefully modeled by the voltage responses of Hodgkin-Huxley equations propagated through axon and dendrite. The second part of the model incorporates the dual requirement of NMDA receptors for opening up calcium ionic channels. Third, to explain the calcium dependent plasticity, a two-component model consisting of calcium dependent protein kinase and phosphatase was built. This unified model with biophysical mechanisms embedded is validated by five different types of STDP responses. In brief, dual requirement of NMDA receptor activation and calcium dependent plasticity are the two key contributors of STDP. The shapes of action potentials coupled with calcium dependent plasticity give rise to different types of STDP responses. Finally, this study suggests further experiments involving modification of action potentials and calcium dependent plasticity to validate the model as well as computational work to explore the emerging properties from groups of Hebbian synapses.

6.1 Current understanding of spike timing dependent plasticity

Synaptic plasticity, the ability of connections between neurons to change in strength, has been intensively studied because it is widely viewed as the underlying mechanism of learning and memory. Spike timing dependent plasticity (STDP) refers to the phenomenon, in which the synaptic plasticity can either be long term potentiated (LTP) or depressed (LTD), depending on the relative timing between external stimuli. STDP has quickly become a popular research area since its discovery partly because it supports and refines Hebb's postulate, an influential activity-dependent learning rule proposed half century ago [65, 105]. Now the revised rule becomes: a Hebbian synapse becomes strengthened if the presynaptic neuron is repeatedly stimulated right before the activation of postsynaptic neuron. Furthermore, STDP has become a commonly used and more realistic experimental protocol for inducing long term depression or potentiation in addition to simple frequency-varying stimulation [20]. Thus, bountiful experimental results from various neuronal tissues are available.

Depending on the type of synapse and nervous system, the profiles of STDP as functions of time delays between pre- and postsynaptic spiking vary significantly [15].

The type of synapse with its specific time window for causing LTP or LTD are summarized in tables [15, 33]. Roughly speaking, two major types of STDP responses exist: temporally symmetric and asymmetric [58]. The former demonstrates no significant effects of temporal order between pre- and postsynaptic stimuli. By contrary, the later shows reverse direction of long-term plasticity under opposite temporal order. The asymmetric STDP can be further divided into two subtypes: Hebbian and anti-Hebbian. For Hebbian synapse, the synaptic strength gets potentiated when EPSPs induced by presynaptic stimuli precede postsynaptic action potentials. Synapses in rat hippocampal culture belong to this class [16]. By contrary, anti-Hebbian synapses show depression instead under the same pre-post temporal stimulation. Synapses linking parallel fiber to Purkinje-like cells in electric fish are good examples [9].

Since there are such various types of STDP, a consequent question to ask is whether a unified theory can be built to explain all scenarios. We hypothesize that such theory exists and can be built as long as we accurately model essential molecular mechanisms that contribute to the temporal dependence of synaptic plasticity. For instance, the back propagation of action potential to dendrites was viewed as important in transmitting postsynaptic signals. Also the dynamics of calcium current gated by N-methyl-D-aspartate (NMDA) receptors was proposed responsible for temporally linking pre- and postsynaptic stimuli. Yet since the phenomena involve multiple presynaptic and postsynaptic reaction pathways (Fig. 1a), modeling work is required to study such composite system.

Several models were developed to explain STDP and can be divided into two classes: phenomenological and mechanistic. Phenomenological models aim to reproduce the experimental responses with simpler mathematical expression from a macroscopic perspective. The simplest phenomenological model describes the STDP responses as two separate levels of synaptic plasticity subject to exponential decay, respectively [15]. Later on, a kinetic model describing change in synaptic plasticity as two-component processes was proposed by Abarbanel et al. [2]. They suggested a depression process activated by presynaptic activity and another potentiation process caused by postsynaptic action. The model successfully demonstrates the time-dependent bidirectionality of synaptic plasticity as a result of interacting depression and potentiation processes. Yet the biomolecules and reactions at cellular level responsible for STDP remain unclear. On the other hand, mechanistic models focus on deriving physiological mechanisms at biomolecular level to interpret experimental findings. Calcium control hypothesis proposed by Shouval et al. [144] suggested the dependence of synaptic plasticity on calcium which is often modeled with BCM rule suggested by Bienenstock et al. [17]. Consequently, NMDA receptors through which calcium ions flow into postsynaptic compartments are the centerpiece of many mechanistic models [1, 144]. They serve as the coincidence detector that relates glutamate release from presynapse and back propagation of postsynaptic action potentials as both are required for activating NMDA receptors. Though being able to explain synaptic plasticity with two LTD windows, these models are not validated by asymmetric STDP responses. To overcome this problem, models with two coincidence detectors were also proposed [78].

Some components of previous work such as calcium control hypothesis and dual requirement of NMDA receptor activation were incorporated in this study. Yet we differentiate our model by systematically assigning or developing biophysical models to a group of molecular reactions that give rise to STDP. First of all, Hodgkin-Huxley equations are adopted to model the shapes of action potentials [68]. The profiles of action

potential have crucial impact that on STDP responses but have been overlooked. The other example is the two-component model of calcium dependent plasticity we developed after extracting essential reactions from previous work [27, 98]. Our model is more biophysically based than empirical BCM rule [17]. It is also sufficient to interpret experimental results with principal underlying molecular mechanisms, granted more detailed biophysical models of BCM rule are also available [26, 27]. Two questions we intend to answer with the unified model are: first, what are the common cellular mechanisms across various types of STDP recorded? Second, what factors differentiate the critical windows and directions of STDP?

6.2 Model development of spike timing dependent plasticity

The spike timing dependent modification of synaptic plasticity requires a group of subsystems interacting with one another in a timely manner. Different from most previous simple models, we built a composite model consists of several subsystems according to the biophysical reality at synapse. The basic biomolecules and physiological reactions at synapses well as external stimuli applied experimentally are depicted in Figure 6-1A. The experimental pre- and postsynaptic stimuli immediately induce transmitter release and action potential, respectively. The reaction scheme of calcium signaling starts with the calcium influx through NMDA receptors activated by glutamate flux and prolonged membrane depolarization. Then calcium kinase (Ca_4K) catalyzes the activation of AMPA receptors while calcium phosphatase (Ca_4P) accelerates the internalization of AMPA receptors. According to the schemes outlined in Figure 6-1A, we developed a corresponding flow diagram of signal processing Figure 6-1B starting from external stimuli until STDP results.

The three components indispensable for STDP modeling are backpropagation of action potential, dual requirement of NMDA receptors, and calcium signaling pathways. Thus, the Model Development section is arranged accordingly. First, the presynaptic stimuli become glutamate flux and postsynaptic stimuli turn into back propogated action potential before they jointly affect NMDA receptors. Second, the influx of calcium enters postsynapse through NMDA receptors which are both ligand- and voltage-gated. Third, activated NMDA receptors allow calcium influx into postsynapse and accumulated calcium level determines the plasticity change by BCM rule. A two-component model was developed to model the calcium dependent plasticity and validated by experimental data of frequency-dependent plasticity. Summary of nomenclature in Table 6-3 lists the meanings of symbols.

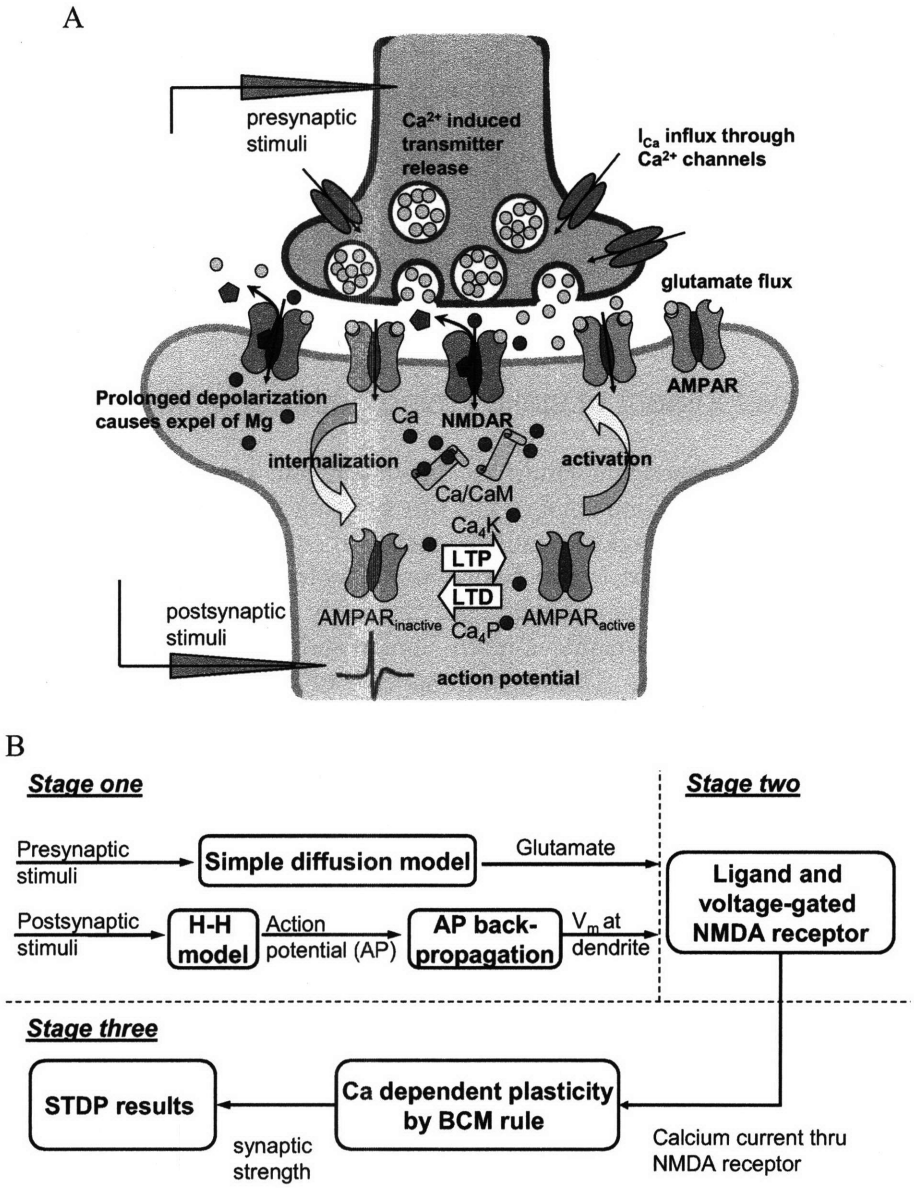

Figure 6-1 Signal transduction pathways related to spike timing dependent plasticity. (A) The presynaptic transmitter release and postsynaptic calcium signaling pathways are depicted. The reaction scheme of calcium signaling starts with the calcium influx through NMDA receptors activated by glutamate flux and prolonged membrane depolarization. Then calcium kinase (Ca_4K) catalyzes the activation of AMPA receptors while calcium phosphatase (Ca_4P) accelerates the internalization of AMPA receptors. The experimental pre- and postsynaptic stimuli immediately induce transmitter release and action potential, respectively. (B) The flow chart of signal processing in the unified model. The chart outlines the transfer functions required to convert pre- and postsynaptic stimuli to the final STDP results. The first stage involves the conversions of presynaptic stimuli to glutamate and postsynaptic stimuli to backpropagated action potential, respectively. The second stage models ligand and voltage-gated NMDA receptors. The third stage describes calcium dependent plasticity by BCM rule. The first and second stages contribute to spike timing dependent calcium current and the later is associated with calcium level controlled plasticity.

6.2.1 Stage one: Model action potential initiation and backpropagation

According to the standard experimental protocol of spike timing dependent plasticity, the postsynapse is repeatedly stimulated either milliseconds before or after the presynapse. The action potentials triggered at postsynapse get backpropagated to the dendrites. Yet most of the previous modeling work did not use the right shapes of action potential let alone the detailed consideration of backpropogation [78, 144]. For instance, action potentials in the NMDA receptor-dependent bidirectional model were depicted by two exponential functions [144]. The shapes of two exponential functions simply decay monotonously with two different slopes whereas those of action potentials recorded experimentally typically demonstrate depolarization, repolarization, and refractory phases.

The action potential is at first initiated at the axon hillock before getting back propagated to the dendrite. We used Hodgkin-Huxley equations to match the shapes of action potential at axon. Then backpropagation can be modeled by an equivalent circuit consisting of axon and dendrite compartments [34]; details can be found in supplemental materials. Compartment models have been commonly used for modeling membrane potentials, assuming the membrane as capacitor separating intra and extra cellular compartments and ion channels as conductors linking the two regions. Hodgkin-Huxley equations, also a compartment model, are suitable for modeling action potential at axon (V_{axon}). The ionic currents incorporated in classical H-H equations are sodium, potassium, and leakage (I_{Na}, I_K, and I_{Laxon}) [68] in additional to the current injected into postsynapse (I_{post}). We also add inter current flowing between axon and dendrite, I_{inter}, which can be calculated by multiplying the conductance (g_{inter}) with the potential difference between two compartments based on Ohm's law.

$$C_{axon}\frac{dV_{axon}}{dt} = -I_{Na} - I_K - I_{Laxon} + I_{post} + I_{inter} \tag{6.1}$$

$$I_{inter} = g_{inter}(V_{dent} - V_{axon}) \tag{6.2}$$

Inter current is introduced here because back-propagating action potentials (BPAPs) from axon to dendrite are crucial for spreading the effects of postsynaptic stimuli. Therefore, the membrane potential at dendrite (V_{dent}) may be influenced by EPSP due to presynaptic stimuli as well as by postsynaptic BPAPs. The time course of EPSP is governed by the binding of glutamate with NMDA and AMPA receptors which causes the ion channel to open or close. Current flow through the receptors further depends upon the conductance of channels (g_{NMDAR} and g_{AMPAR}).

$$\begin{aligned} C_{dent}\frac{dV_{dent}}{dt} &= -I_{NMDAR} - I_{AMPAR} - I_{Ldent} - I_{inter} \\ &= -g_{NMDAR}V_{dent} - g_{AMPAR}V_{dent} - I_{Ldent} - I_{inter} \end{aligned} \tag{6.3}$$

The shape of action potentials of each experiment was carefully examined to select appropriate theoretical models. Standard Hodgkin-Huxley (H-H) equations are sufficient for modeling (1) asymmetric STDP following Hebbian rule [68]. However, different from the output of the classical equations, the shapes of the action potentials in 6.3.2.2

asymmetric STDP following Hebbian rule and in 6.3.2.3, 6.3.2.4, and 6.3.2.5 symmetric STDP demonstrates depolarizating after potential (DAP) behavior. Thus, for these two cases we introduced DAP into H-H model by inverting the hyperpolarization part of action potentials. The model types of action potential are summarized in Table 6-1.

6.2.2 Stage two: Dual requirements for NMDA receptor activation

Postsynaptic calcium signaling plays an important role in regulating long term plasticity [29, 180] and NMDA receptor-gated ion channels serve as the main gateways through which calcium flows into postsynapse. For simplicity, we assume NMDA receptor-gated ion channels as the source of calcium inflow and the opening of NMDA-receptor channels is governed by the binding of glutamate and substantial degree of depolarization. Consequently, the conductance of NMDA receptors (g_{NAMDAR}) is assumed to be the product of two terms: the dependence function of glutamate concentration (Glu) and that of membrane voltage (V_{dent}). Note that glutamate flux mainly results from presynaptic stimuli while depolarization is caused by the back propagation of postsynaptic action potential.

The first term, glutamate dependence, is described by the ligand-receptor model with association constant K_{Glu}. Glutamate concentration can be related back to the presynaptic stimuli (I_{pre}) by a simple diffusion model with the details described in supplemental materials. Second, the voltage dependence has been modeled with the logistic function as shown in Eq.(6.4) [74] with the exponential term originated from the Arrhenius equation [34]. The voltage dependent activity function rises to a maximum ($g_{NMDARmax}$) following a sigmoidal curve with half way voltage equal to $V_{1/2}$ and slope as large as $0.5k_{NMDA}$ at that point. Finally, the expression of $g_{NMDAR}(V_{dent}, Glu)$ can be inserted back to Eq. (6.3) to simulate current flow and membrane voltage at dendrite.

$$g_{NMDAR}(Glu, V_{dent}) = \frac{Glu}{Glu + K_{Glu}} \times \frac{g_{NMDARmax}}{1 + e^{-k_{NMDAR}(V_{dent} - V_{1/2})}} \tag{6.4}$$

The conductance of NMDA receptor-gated ion channels dictates the amount of calcium flowing into postsynapse. Under the assumptions that the NMDA receptors are the major gateway of calcium inflow and the leakage rate of calcium is negligible, calcium concentration would be proportional to the integration of current flow through NMDA receptors over the time span of stimuli as in Eq. (6.5). I_{NMDAR} can also be expressed as the product of conductance (g_{NMDAR}) and dendrite membrane potential (V_{dent}). The total calcium concentration remains constant after the induction stimuli if we assume the loss of calcium ions through leakage is negligible throughout the experiment. Also the concentrations of calcium are much higher than those of calcium-dependent proteins, most of the total calcium concentration (CaT) is assumed to exist in ionic form (Ca).

$$Ca \propto \int_{t_{stimuli}} I_{NMDAR} dt = \int_{t_{stimuli}} g_{NMDAR} V_{dent} dt \tag{6.5}$$

The lag time between glutamate flux (presynaptic) and membrane depolarization (postsynaptic) influences the level of NMDA receptor activation and thus the amount of

calcium inflow. Since both transient signals only last for tens of milliseconds, such temporal proximity between pre- and postsynaptic stimuli is necessary to trigger interaction. Figure 6-2A and B show the transient profiles of glutamate from presynapse and membrane depolarization at postsynapse with lag time equal to positive or negative five milliseconds, respectively. When the glutamate profile overlaps mostly with positive portion of action potential (Figure 6-2A) in time, both requirements of NMDA receptor activation are met so more calcium flows into postsynapse. In contrast, if glutamate influx occurs at the same time as undershoot part of action potential instead (Figure 6-2B), it can only elicit partial opening of NMDA-receptor channels, which results into less calcium inflow. How calcium level influences the direction of synaptic plasticity is discussed in the following section.

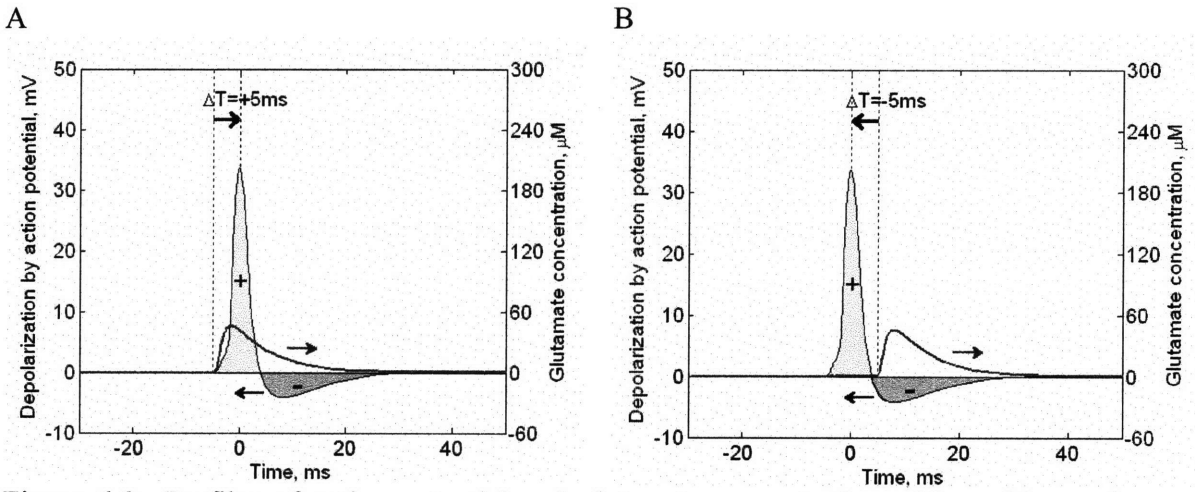

Figure 6-2 Profiles of action potential and glutamate concentration with positive and negative time differences in between. The responses are further used in modeling forward spike timing dependent plasticity.
(A) Onset of glutamate input precedes the peak of action potential by 5 ms. (B) Onset of glutamate input lags the peak of action potential by 5 ms.

6.2.3 Stage three: Two component model of calcium dependent plasticity

The level of calcium entering postsynaptic compartment through NMDA recptors was found to strongly influence synaptic plasticity [29, 180]. Furthermore, depending on the total amount of calcium inflow, postsynaptic calcium may either up- or down-regulate signal transduction pathways and lead to synaptic plasticity change. Long-term synaptic strength tends to depress at moderate level of Ca^{2+} elevation but gets potentiated at high level [25, 33]. The BCM rule is an omega-shaped function able to well describe the dependence of synaptic strength on postsynaptic activities [17]. It has actually been used in previous STDP models to relate synaptic strength to intracellular calcium concentration [144]. Both empirical and mechanistic models have been developed to reproduce BCM rules. Simple empirical models may not pinpoint physiological reactions responsible for the omega function of synaptic plasticity [171]; yet detailed mechanistic models involving complex multi-step calcium dependent enzyme activation are difficult to reproduce [26, 27]. After extracting essential reaction mechanisms, we developed a simple two

component calcium binding model with sufficient biophysical details to describe the phenomena.

Calcium dependent kinase and phosphatase have been suggested relevant in eliciting bidirectional synaptic plasticity [27, 29, 98]. Postsynaptic calcium influences the synaptic plasticity through two steps. First, intracellular calcium either binds with calcium-dependent protein kinases or phosphates. Afterwards, these calcium-bound enzymes insert active AMPA receptors to or remove them from postsynaptic membrane, respectively [91, 92]. The final number of active AMPA receptors remaining determines the synaptic conductance and thus plasticity.

The model development starts with the description of binding between calcium and two types of enzymes. The trapped calcium can either bind with calmodulin-dependent protein kinase II (K for short) or protein phosphatase 1 (P for short) as shown in Eq.(6.6). The binding between enzymes and calcium is assumed to be cooperative and four calcium ions are required to fully activate the kinase (Ca_4K) or protein phosphatase (Ca_4P).

$$\begin{aligned} 4Ca + K &\underset{k_{CaKb}}{\overset{k_{CaKf}}{\rightleftharpoons}} Ca_4K \\ 4Ca + P &\underset{k_{CaPb}}{\overset{k_{CaPf}}{\rightleftharpoons}} Ca_4P \end{aligned} \tag{6.6}$$

Consequently, the fourth order Hill equation can be used to model the formation of Ca_4K and Ca_4P [22] while the decomposition is modeled as first order reaction. The rates of change in Ca_4K and Ca_4P concentrations are equal to the formation rate minus consumption rate as summarized in Eq.(6.7). Since experimental results of STDP are usually summarized in terms of the final plasticity change, the concentrations after reaching steady state are of special interest. At steady state, the time derivatives in Eq.(6.7) are equal to zero so concentrations of Ca_4K and Ca_4P can be expressed in terms of Ca. The steady state values of Ca_4K and Ca_4P are plotted against Ca in Figure 6-3A.

$$\begin{aligned} \frac{dCa_4K}{dt} &= k_{CaKf}\frac{Ca^4}{Ca^4 + K_{CaK}^4} - k_{CaKb}Ca_4K = 0 \qquad \therefore\ Ca_4K = \frac{k_{CaKf}}{k_{CaKb}}\frac{Ca^4}{Ca^4 + K_{CaK}^4} \\ \frac{dCa_4P}{dt} &= k_{CaPf}\frac{Ca^4}{Ca^4 + K_{CaP}^4} - k_{CaPb}Ca_4P = 0 \qquad \therefore\ Ca_4P = \frac{k_{CaPf}}{k_{CaPb}}\frac{Ca^4}{Ca^4 + K_{CaP}^4} \end{aligned} \tag{6.7}$$

Afterwards, calmodulin-dependent protein kinase II bound by calcium (Ca_4K) can insert and activate AMPAR [64] whereas calcium-bound protein phosphatase 1 (Ca_4P) may internalize and deactivate AMPAR [113] as summarized in Eq.(6.8). In detail, k_{AMPARf} and k_{AMPAb} denote the forward and backward reaction rate constants of AMPAR activation. Furthermore, V_{CaK} and V_{CaP} are proportional constants that quantify the contributions of Ca_4K and Ca_4P to the rate constants, respectively.

$$AMPAR_{inactive} \underset{k_{AMPARb} + V_{CaP}Ca_4P}{\overset{k_{AMPARf} + V_{CaK}Ca_4K}{\rightleftharpoons}} AMPAR_{active} \tag{6.8}$$

Concentration change of Ca_4K and Ca_4P caused by calcium inflow would perturb the balance between active and inactive AMPA receptors. Under the assumptions that total number of AMPAR remains constant, difference between synaptic strength before and after stimuli (ΔW) is proportional to the change in normalized forward rate constants.

$$\Delta W \propto \frac{k_{AMPARf} + V_{CaK} Ca_4 K}{k_{AMPARb} + V_{CaP} Ca_4 P + k_{AMPARf} + V_{CaK} Ca_4 K} - \frac{k_{AMPARf}}{k_{AMPARb} + k_{AMPARf}} \tag{6.9}$$

Now we can map out the relationship between the change of synaptic strength (ΔW) and calcium concentration (Ca) in Eq.(6.9). The steady state concentration of Ca_4K and Ca_4P into Eq. (6.9) can be expressed as functions of Ca according to Eq.(6.7). Thus with other parameter values listed in Table 6-1, synaptic plasticity change as a function of calcium, $\Delta W(Ca)$, is plotted in Figure 6-3B.

6.3 Modeling Results

The model was utilized to explain experimental results of both frequency dependent and spike timing dependent synaptic plasticity (STDP). One experimental dataset of frequency-dependent plasticity was modeled first by using our two component model of calcium dependent plasticity. Afterwards, five scenarios of STDP experimental results were analyzed individually to demonstrate the applicability of the unified model.

6.3.1 Model frequency and calcium dependent plasticity

Directionality of long term plasticity in rat hippocampal slices was experimentally found to depend upon stimulus frequency by Bear et al. [41] Under low frequency stimuli the synapses get depressed while high frequency stimuli result into long term potentiation. The omega-shaped functional dependence of plasticity on frequency mimics the response predicted by BCM (Bienenstock–Cooper–Munro) rule. Castellani et al. suggested the frequency dependent plasticity is the joint consequence of frequency dependent calcium inflow and calcium dependent plasticity. They also built a model that reproduces BCM rule and asserted intracellular calcium concentration to be directly proportional to stimuli frequency [27]. Therefore, a conversion constant is sufficient to switch between calcium- and frequency-dependent plasticity.

There are two conditions that the profiles of kinase and phosphatase have to meet in order to match the omega-shaped response [27, 29, 98]. First, phosphatase gets activatived at low calcium concentration faster than kinase. Second, at high concentration, the activity of kinase surpasses that of phosphatase [27]. As shown in Figure 6-3A, given calcium-dependent phosphotase (CaP) is estimated to be more sensitive to calcium than kinase (CaK) is, it saturates at lower calcium concentration. Furthermore, since CaP may weaken synaptic strength by inactivating AMPA receptors, the change in synaptic strength (ΔW) dips at low total calcium concentration (CaT) as in Figure 6-3B. Yet the decrease is soon

counteracted by CaK which becomes more active at higher CaT and enhances synaptic connectivity. Also labeled is the CaT value corresponding to largest synaptic strength decrease (θ_{min}) as well as the threshold calcium concentrations (θ_d and θ_p) bordering the sign change of ΔW. Then according to Figure 6-3C, our calcium entrapment model is validated by the frequency-dependent "change in EPSP slope" which is an experimental metrics of ΔW. In conclusion, different sensitivities of kinase and phosphotase to calcium result into selective signaling and omega-shaped function.

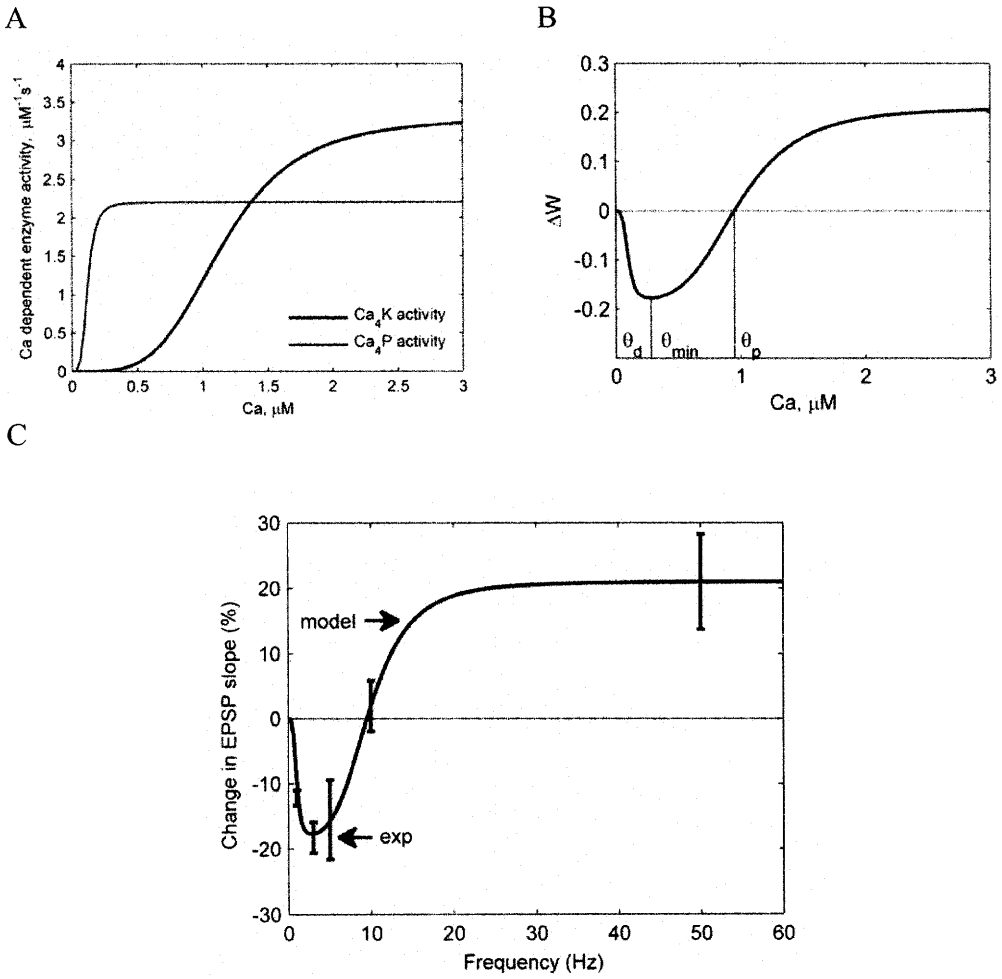

Figure 6-3 Total calcium concentration determines direction of plasticity. That is the output of two-component BCM model.
(A) Concentrations of Ca_4K and Ca_4P as functions of CaT. (B) Change in synaptic strength as a function of total calcium concentration. CaT values corresponding to three thresholds, θ_p and θ_d (thinner lines) are labeled. (C) The synaptic plasticity and EPSP slope as functions of frequency, respectively. The experiments were done on the Schaffer collateral projection to area CA1 in rat hippocampal slices by Dudek and Bear, 1992 [41].

6.3.2 Model spike timing dependent plasticity

Depending upon the type of synapse, the responses of spike timing dependency may differ. The commonly observed responses can be divided into three groups: forward STDP, backward STDP, and STDP with two LTD windows. The unified theory we proposed can explain all three cases.

6.3.2.1 Asymmetric STDP following Hebbian rule

Forward STDP refers to the type of spike timing dependent plasticity in which depression arises when repetitive presynaptic stimuli closely precede postsynaptic ones and potentiation occurs under the opposite condition. The change in synaptic plasticity as a function of spike timing was well recorded by Bi and Poo in rat hippocampal neurons [16]. According to their experimental protocol, transient responses of long term plasticity as results of different spike timing were measured at first. Afterwards, the steady state change of synaptic strength was plotted as a function of spike timing different between pre- and postsynaptic stimuli. Therefore, our modeling followed the same procedure of data processing.

Transient responses of positively correlated pre- and postsynaptic stimuli demonstrate positive steady state response (LTP) and those of negatively stimuli show negative response (LTD), instead [16]. As shown in Figure 6-4A, when EPSP caused by presynaptic stimulus precedes action potential by 5 ms, the normalized EPSC amplitude increases about 50%. In contrast, the opposite temporal order makes the EPSC amplitude decreases by 20% (Figure 6-4B). Considering the dynamics of NMDA receptors coupled with calcium two-component model, we simulated both the positive and negative spike timing in Figure 6-4. Even with the exactly same sets of parameters, the results clearly show distinct directions of synaptic plasticity as a result of temporal order. Also the rise time and steady-state EPSC amplitudes do match the experimental data. This indicates that our systematic model is likely to be the underlying mechanism of STDP given specific spike timing.

Furthermore, typical STDP experiments include measuring synaptic plasticity at various spike timing as shown in D. Apparently, the temporal order determines the polarity of the long term plasticity. To model the phenomena, we first generated action potential by Hodgkin-Huxley equations and plotted the backpropagated potential through postsynaptic equivalent circuit (Fig. 5A). Then 60 pulses of such action potential at 1 Hz along with glutamate input were applied to the systematic model built to calculate resultant total calcium concentration. As presented in Fig. 5B, fewer calcium flows into postsynapse in the case of negative spike timing in opposed to more two to three times more calcium at about spike timing of + 0~15 ms. Finally the calcium dependent plasticity function in Fig. 5C was used to convert calcium concentration into change in number of active AMPA receptors and thus, synaptic strength. Fig. 5D shows close match between experiments and model, which again validates the systematic approach that takes into account interacting components.

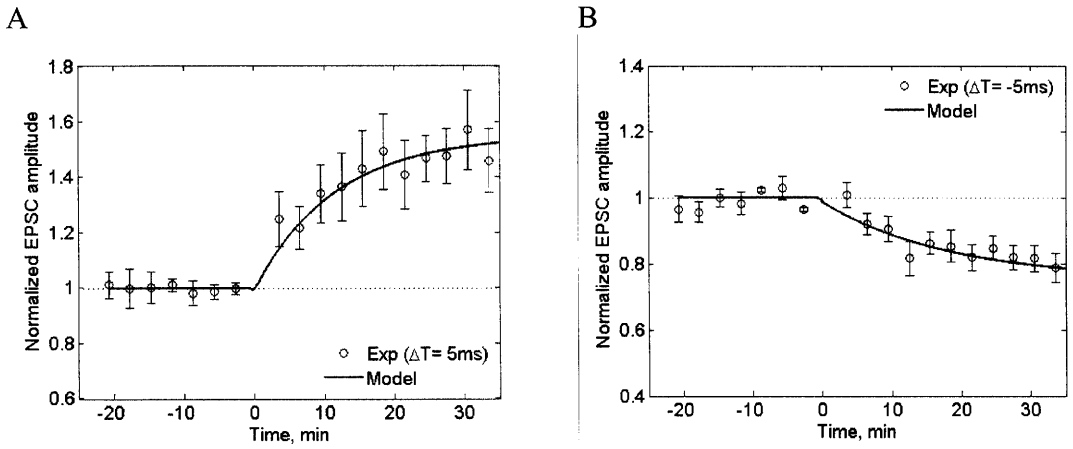

Figure 6-4 Transient EPSC responses due to 60 pulses of correlated pre- and post-synaptic stimuli at 1 Hz. The parameters used in modeling both data sets are the same. (A) Experimental data and model for positively correlated postsynaptic spiking in which each presynaptic stimulus precedes postsynaptic stimulus by five milliseconds. (B) Experimental data and model for negatively correlated postsynaptic spiking in which each postsynaptic stimulus precedes presynaptic stimulus by five milliseconds. Data source: Bi and Poo, 1998 [16].

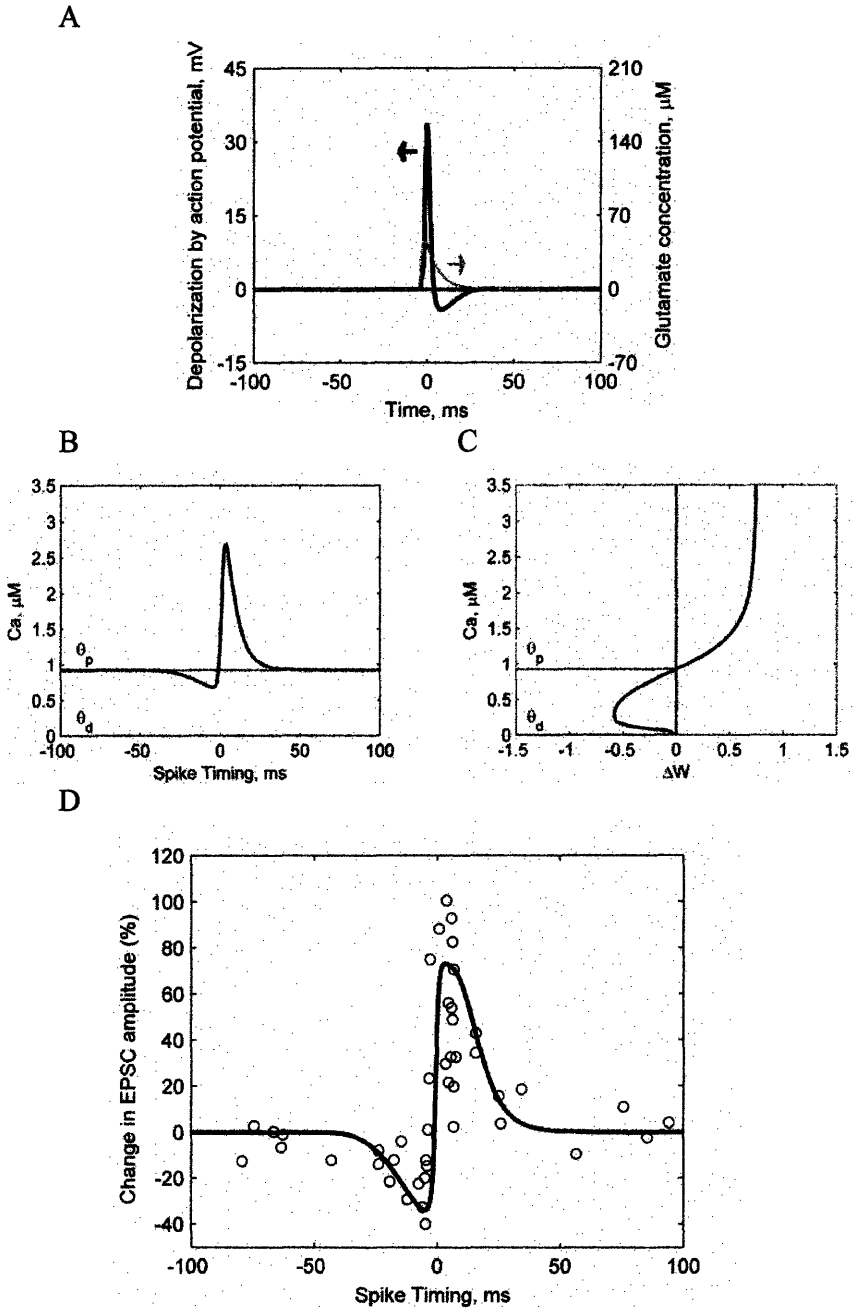

Figure 6-5 Asymmetric STDP following Hebbian rule. The STDP responses were measured after correlated pre- and postsynaptic stimuli 60 pulses at 1 Hz.
(A) Overlapping between back propagating action potential and transient glutamate concentration. (B) Concentrations of CaT vs. spike timing. Two thresholds, θ_p and θ_d (thinner lines) based on the adjacent plot C are labeled. (C) Change in synaptic strength as a function of total calcium concentration according to two-component BCM model. Two thresholds are also labeled. (D) The experimental data and model. Data source: Bi and Poo, 1998 [16].

6.3.2.2 Asymmetric STDP following anti-Hebbian rule

The directional dependence of backward STDP response on temporal order of pre- and postsynaptic stimuli is opposed to that of forward STDP. For instance, in parallel fibre synapses of cerebellum-like structures in electric fish, Bell et al. observed LTP when EPSP precedes action potential and LTD under the opposite condition [9]. There maybe different types of plasticity in cerebral cortex and in cerebellum-like structure. More specific explanation may be the difference in the shape of action potential. The parallel fibre synapses in GABAergic Purkinje-like cells are mostly inhibitory. Similar to other inhibitory synapse, the generated action potential demonstrates apparent hyperpolarization before the peak of the spike. The inversion in action potential may result into backward STDP as shown in Figure 6-6D.

The shape of action potential influences spike timing dependent total calcium concentration and eventually STDP response as summarized in Figure 6-6. First, the inhibitory action potentials measured get hyperpolarized in the beginning and show no refractory phase at the end [9]. Overall they appear significantly different from typical profiles generated from Hodgkin-Huxley model. Therefore, we simulated the APs in this case by inserting inhibitory current to a modified H-H model with depolarizating after potential (DAP) behavior [72](Figure 6-6A). Consequently the output profiles of inhibitory action potentials appear inverted in time compared to normal action potentials. In such case, glutamate influx is out of phase with earlier part of action potential and in sync with later portion. This is why the total calcium concentration drops at positive spike timing and increases at the negative part (Figure 6-6B). After coupling spike timing dependent total calcium concentration (Figure 6-6B) with the function of calcium-dependent synaptic strength (Figure 6-6C), we obtain the response of backward STDP. The good agreement between the output of experiments and theory (Figure 6-6D) suggests that the shape of action potential greatly influences the directionality of STDP responses.

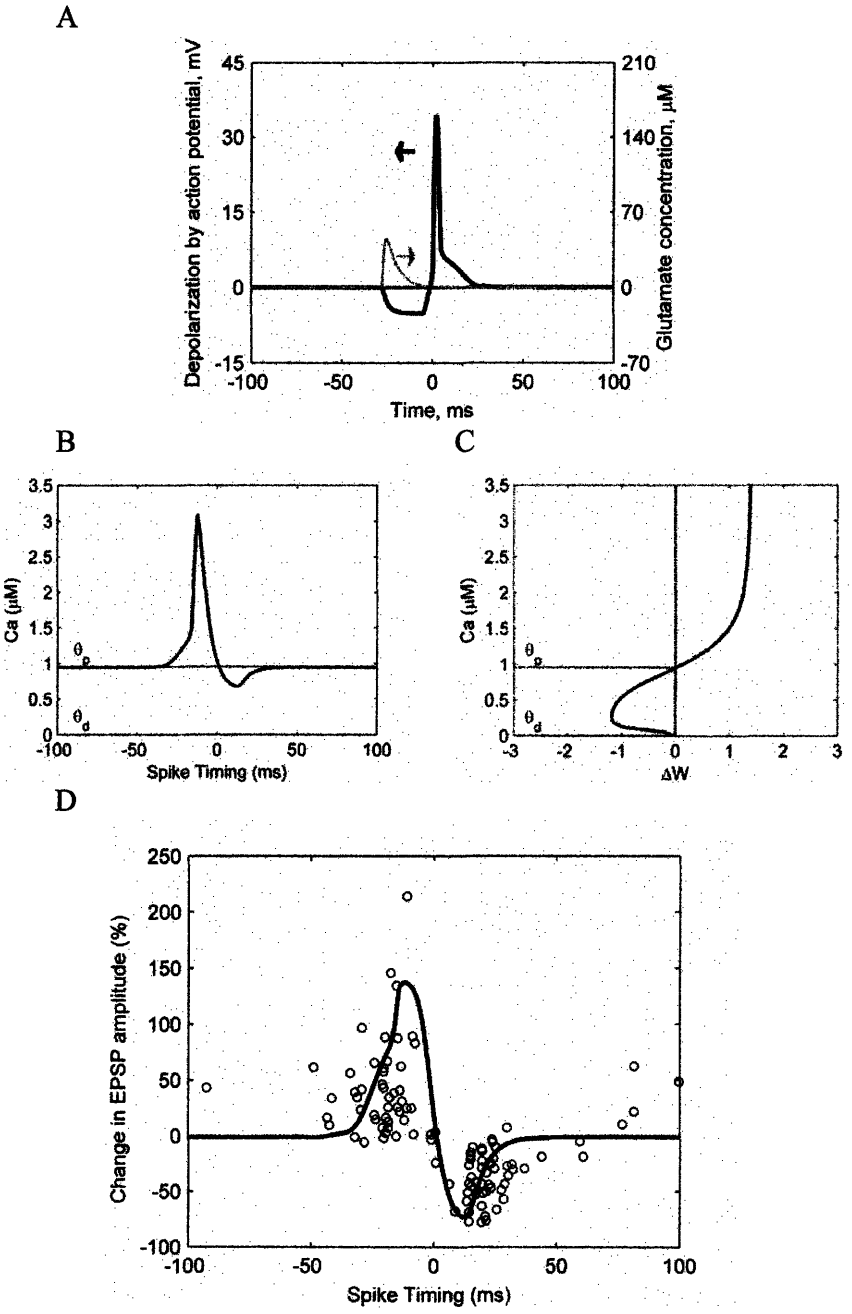

Figure 6-6 Asymmetric STDP following anti-Hebbian rule.
(A) Overlapping between back propagating action potential and transient glutamate concentration. (B) Concentrations of CaT vs. spike timing. Two thresholds, θ_p and θ_d (thinner lines) based on the adjacent plot C are labeled. (C) Change in synaptic strength as a function of total calcium concentration according to two-component BCM model. Two thresholds are also labeled. (D) The experimental data and model. Data source: Bell et al., 1997 [9].

6.3.2.3 Symmetric STDP with mixed LTP and LTD

The third type of STDP demonstrates two depression windows at spike timing around +20 ms and –20 ms, respectively while the time interval in between results into potentiation. This phenomenon was first discovered in CA1 pyramidal neurons of rat hippocampus by Nishiyama et al. [118]. Later on similar responses of two LTD windows at around spike timing of ±25 ms were reported by Wittenberg et al. at CA3-CA1 synapses as well [172]. This phenomenon was studied previously by Shouval et al. and a model of NMDA receptor-dependent bidirectional synaptic plasticity was built accordingly [144]. Their model consisted of NMDA receptor dynamics coupled with BCM rule. The model output followed the general trend of STDP with two LTD windows but was not compared side by side with the experimental data.

Although our model includes similar building blocks as previously proposed, it considered the underlying mechanisms of individual subsystems more rigorously and thus, follows experimental data and underlying mechanisms more closely. First, since the shape of action potential in the experiment appears similar to the type of "depolarizing after-potential" categorized by Izhikevich [72, 118], it was modeled accordingly in Figure 6-7A. Because there is no apparent hyperpolarization portion in the action potential, the convolution between glutamate and backpropogated action potential simply contributes to higher calcium level (Figure 6-7B). The reason for the existence of two depression windows even at monotonously higher calcium concentration was the omega-shaped calcium-dependent synaptic strength. More specifically, as indicated in Figure 6-7B and Figure 6-7D, the highest calcium concentration ($> \theta_p$) at around time zero results into largest increase in synaptic plasticity. Meanwhile, the level of calcium between θ_d and θ_p lead to the two depression windows with the largest drop of synaptic strength corresponding to θ_{min}. The curve of calcium dependent plasticity in Figure 6-7C was inferred from the experimental data of STDP (Figure 6-7D) and the parameter values are listed in Table 6-1.

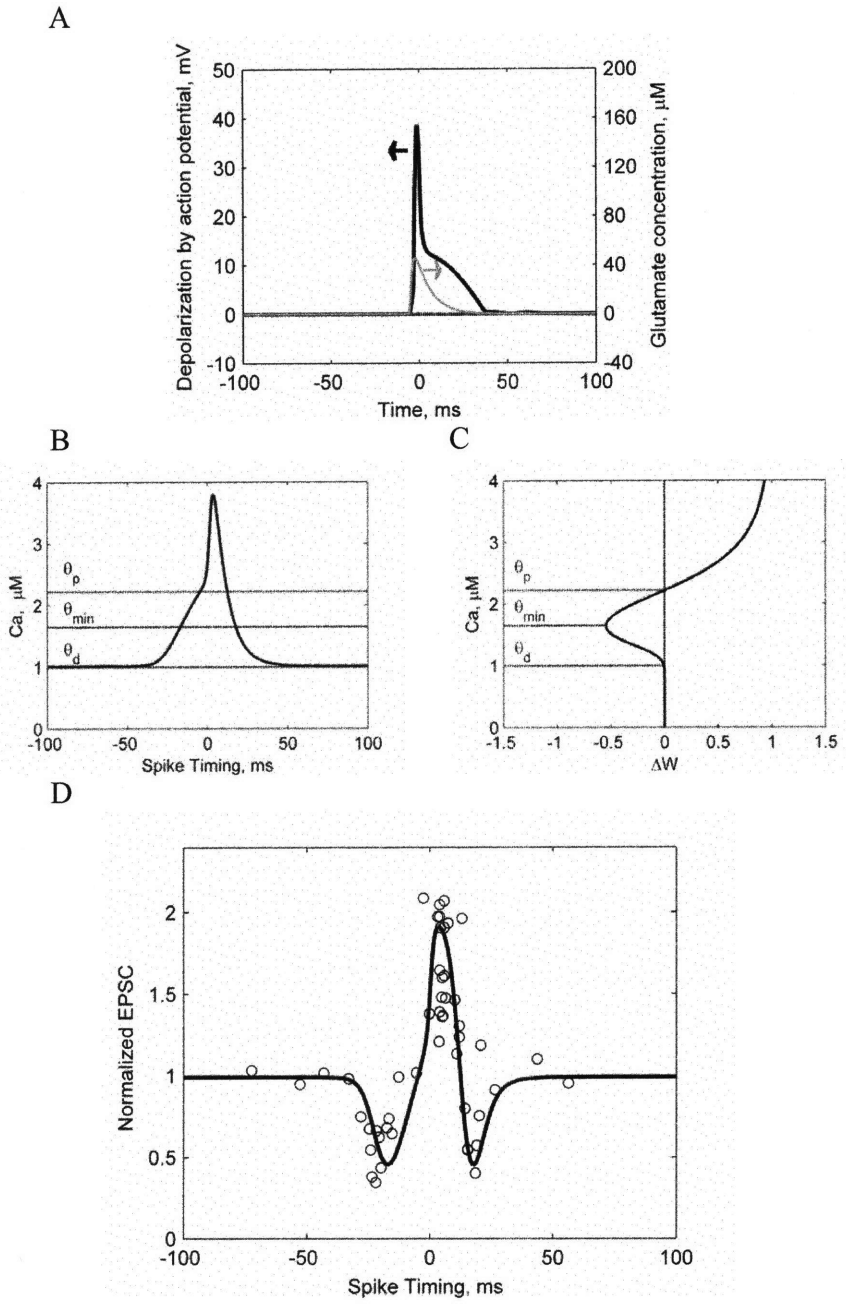

Figure 6-7 Symmetric STDP with mixed LTP and LTD.
(A) Overlapping between back propagating action potential and transient glutamate concentration. (B) Concentrations of CaT vs. spike timing. Three thresholds, θ_p, θ_{min}, and θ_d (thinner lines) based on the adjacent plot C are labeled. (C) Change in synaptic strength as a function of total calcium concentration according to two-component BCM model. Three thresholds are also labeled. (D) The experimental data and model. Data source: Nishiyama et al., 2001 [118].

6.3.2.4 Symmetric STDP with only LTP

The symmetric STDP with only LTP was discovered in hippocampal slice CA1 fairly early and researchers back then already suspected convolution is the cause of the phenomenon. According to the experimental data shown in Figure 6-8D, time lags between pre- and postsynaptic stimuli ranging from -40 ms to 50 ms result into LTP without observable LTD [57]. This type of STDP is the simple to explain because the response appears like common results of convolution.

Again we used H-H model with depolarization after potential to model the action potentials before convolving them with glutamate profiles (Figure 6-8A). Yet the difference is in the exact shapes of BCM curves adopted. In the previous section "6.3.2.3 symmetric STDP with mixed LTP and LTD", shifted BCM model with positive θ_d was used. Here we chose original BCM model with θ_d equal to zero instead, as shown in Figure 6-8C. The parameters were specified so that the accumulated calcium concentration level lies above the threshold value, θ_p (Figure 6-8B). Under such circumstance, the change in synaptic strength is positive and increases monotonously with calcium. Therefore, the timing dependent calcium level becomes symmetric STDP plot with only LTP (Figure 6-8D).

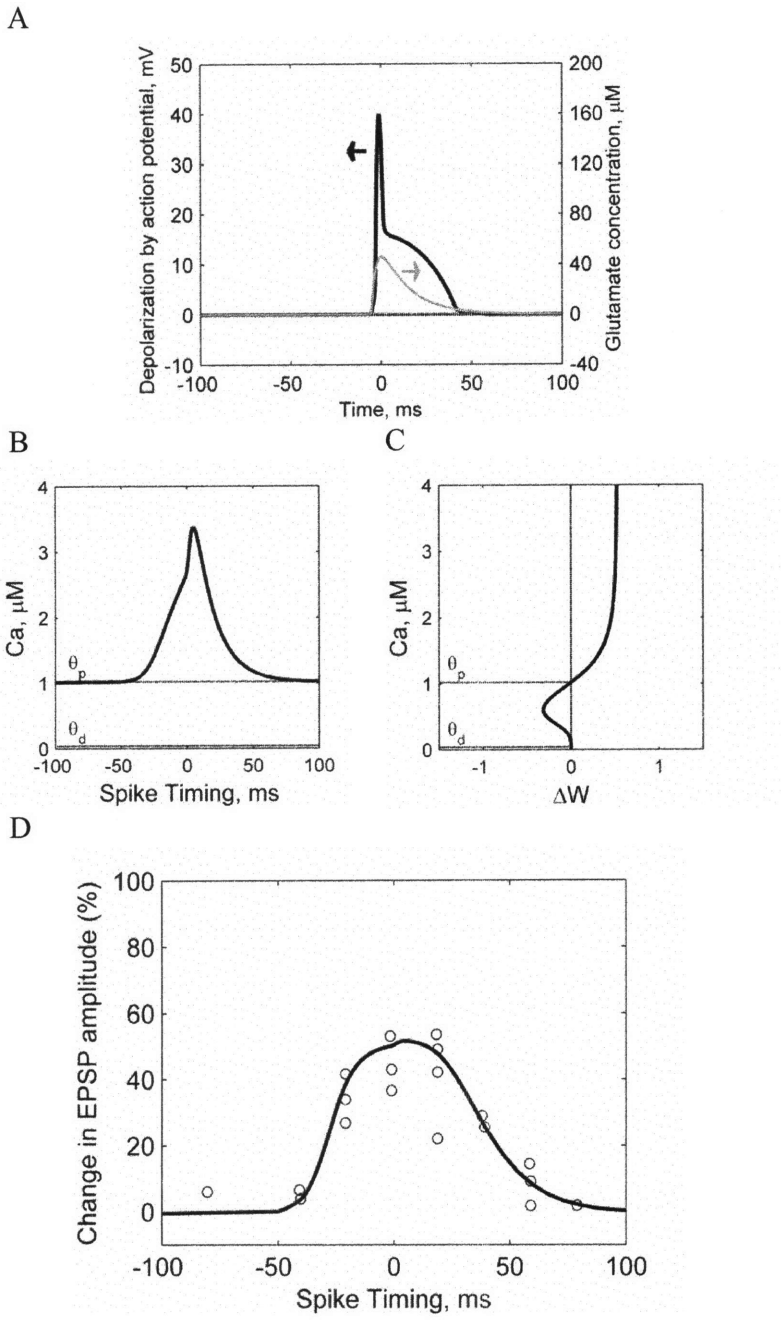

Figure 6-8 Symmetric STDP with only LTP.
(A) Overlapping between back propagating action potential and transient glutamate concentration. (B) Concentrations of CaT vs. spike timing. Two thresholds, θ_p and θ_d (thinner lines) based on the adjacent plot C are labeled. (C) Change in synaptic strength as a function of total calcium concentration according to two-component BCM model. Two thresholds are also labeled. (D) The experimental data and model. Data source: Gustafsson et al. 1986 [57].

6.3.2.5 Symmetric STDP with only LTD

On the other hand, the symmetric STDP with only LTD was discovered in rat barrel cortical slice and in rat hippocampal CA3-CA1 [43, 172], respectively. The experimental protocols adopted for eliciting symmetric STDP with only LTD are similar to previous experiments. The spike timing difference for generating LTD was between -50 ms and 50 ms. Throughout the pairing stimulation, no significant long term potentiation was detected [43, 172].

What causes some synapses to demonstrate STDP with only LTD and others to show LTP only? Since the measure action potentials remain fairly similar (Figure 6-9A), the answer might lie in the relative levels between calcium concentration and the threshold values of BCM rules. The measured dendritic action potentials still exhibit depolarization after potential, so we used similar action potential shapes as in "6.3.2.4 Symmetric STDP with only LTP". Yet we applied a smaller proportional constant, assuming the magnitude of calcium concentration is lower (Figure 6-9B). The reasons might be larger sizes of postsynaptic compartments or weaker calcium current inflow. Then other parameters were assigned such that accumulated calcium concentration level lies between two threshold values, θ_{min} and θ_d. Under this condition, synaptic strength decreases monotonously with calcium so highest concentration level at time zero corresponds to the lowest synaptic strength (Figure 6-9B and Figure 6-9C). Finally the Fig. 9b becomes the STDP with only LTD with the left and right side symmetric to one another (Figure 6-9D).

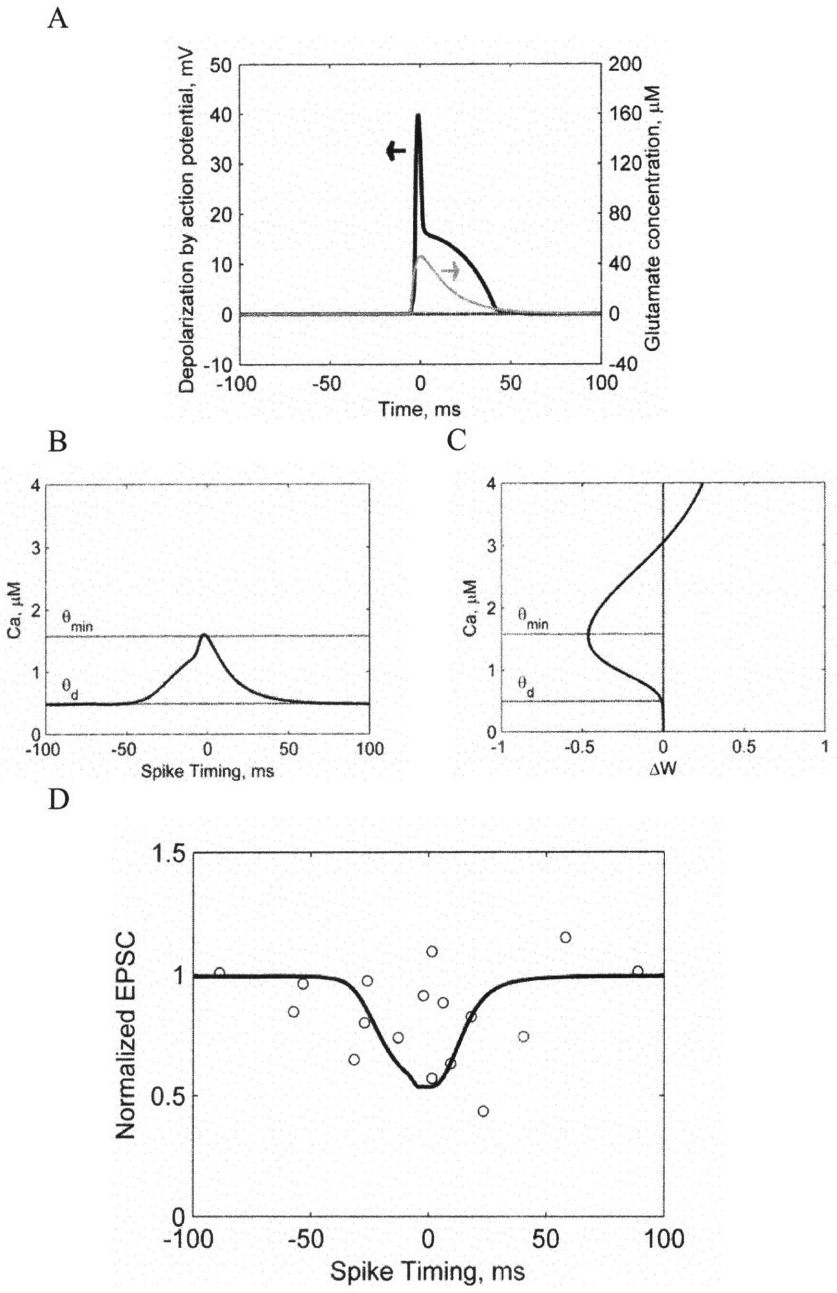

Figure 6-9 Symmetric STDP with only STD.
(A) Overlapping between back propagating action potential and transient glutamate concentration. (B) Concentrations of CaT vs. spike timing. Three thresholds θ_d, θ_{min}, and θ_p (thinner lines) based on the adjacent plot C are labeled. (C) Change in synaptic strength as a function of total calcium concentration according to two-component BCM model. Two thresholds are also labeled. (D) The experimental data and model. Data source: Wittenberg et al. 2006 [172].

Table 6-1 The time constants, estimated parameters and action potential models in various STDP cases

Classification	Parameter	Unit	asymmetric Hebb	asymmetric anti-Hebb	symmetric mixed	symmetric LTP	symmetric LTD
Location	-	-	Rat hippo-campal culture	Cerebellum-like structure	Rat hippo-campal slice CA1	Rat hippo-campal slice CA1	Rat hippo-campal CA3-CA1
Spike timing [15]	Δt (LTD)	ms	-30 ~ 0	0 ~ +50	-30 ~ -10 +15 ~ +20	None	-50 ~ 50
	Δt (LTP)	ms	0 ~ +15	-50 ~ 0	0 ~ +15	-40 ~ 50	None
Parameters of Ca-dependent plasticity	K_{CaK}	μM	1.16	1.20	2.10	1.22	3.84
	K_{CaP}	μM	0.12	0.10	0.9	0.81	1.30
	θ_p	μM	0.92	0.95	2.22	1.02	3.05
	θ_d	μM	0.00 (zero)	0.00 (zero)	1.02 (nonzero)	0.00 (zero)	0.47 (nonzero)
	V_{CaK}	$\mu M \cdot s^{-1}$	3.4	3.5	3.7	4.6	5.0
	V_{CaP}	$\mu M \cdot s^{-1}$	2.1	1.0	0.7	1.2	1.2
Action potential model	-	-	Classical H-H equation [68]	Inhibitory H-H eq. with DAP	H-H eq. with DAP	H-H eq. with DAP	H-H eq. with DAP
References	-	-	Bi and Poo 1998	Bell et al. 1997	Nishiyama et al. 2000	Gustafsson et al. 1986	Wittenberg et al. 2006

‡ θ_p is the upper calcium concentration limit and θ_d is the lower calcium concentration limit in switching directions of calcium-dependent plasticity.

6.4 Conclusion of spike timing dependent plasticity

The spike timing dependent plasticity is the manifestation of several subsystems interacting with one another as shown in Figure 6-10. The temporal order specificity is the result of convolution between presynaptic glutamate flux and postsynaptic depolarization both of which are necessary for activation of NMDA receptors. The glutamate influx is elicited by presynaptic stimuli and membrane depolarization is initiated by action potentials due to postsynaptic stimuli.

The underlying cellular reactions that cause spike timing dependency were not fully understood with the previous molecular biology methodology. Systematic study and model based experiment are more efficient ways in deciphering STDP. Without the quantitative model, a number of qualitative hypotheses are left unchecked. Based on the fact that the unified model proposed here is capable of explaining various kinds of STDP, the actual physiological mechanisms may be close to our description. The temporal specificity is the manifestation of both NMDA receptor-mediated calcium influx and calcium dependent plasticity.

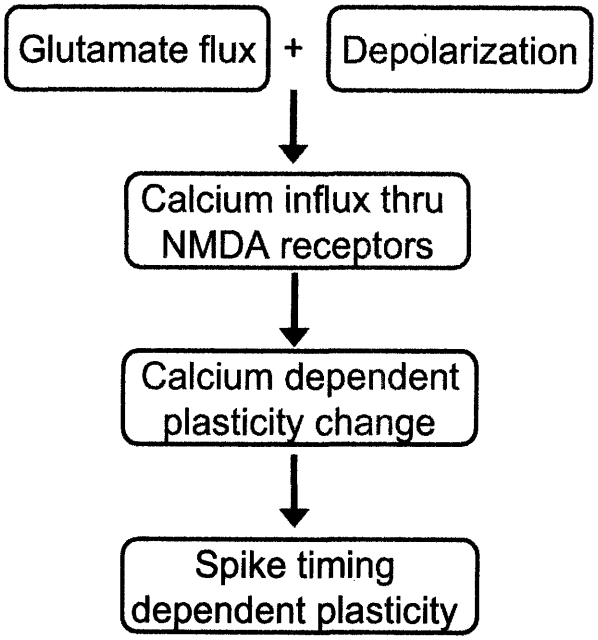

Figure 6-10 The flow chart summarizes mechanisms of spike timing dependent plasticity

Perturbation of parameters (Figure 6-11) demonstrates how different physiological condition leads to the change in STDP response. As shown in Figure 6-11A, raising the sensitivity of calcium-dependent kinase (i.e., decreasing K_{CaK} values) weakens the depression level of the LTD window. The reason is that the more sensitive the kinase is to calcium (i.e., it gets saturated more easily), the lower the level of synaptic strength is. Therefore, the perturbation of K_{CaK} causes the variation of STDP in terms of intensity but not in the width of time window. On the other hand, changing in the recovery rate of potassium channels alters the time course of action potential. As a result, the action

potential recovers from hyperpolarization slower and thus the time window within which LTD prevails are widened (Figure 6-11B).

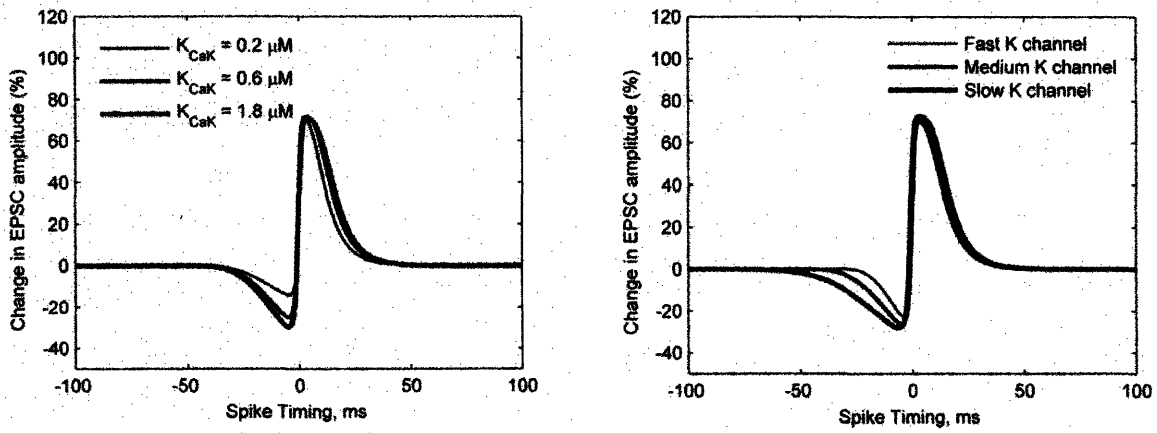

Figure 6-11 Perturbation analysis of STDP.
(A) Change the calcium sensitivity. (B) Change the recovery rate of potassium channel.

With the unified theory developed, we can resolve some of the controversial issues in this field. The first one was whether one coincidence detector is sufficient to demonstrate STDP response [33, 78]. The second issue is whether the spike timing dependent long term potentiation and depression involves independent processes. As demonstrated by the response of the model, NMDA receptor as a single coincidence detector can give rise to a variety of STDP outcome. Therefore, voltage gated calcium channels (VGCC) as the second coincidence detector is not necessarily required. Second, the spike timing potentiation and depression are likely to result from an integrated mechanism. Such mechanism gives rise to potentiation or depression, depending on the relative timing of glutamate flux and membrane depolarization as the two requirements of NMDA receptor activation.

Hebb's learning rule is closely related to the time interval between pre- and postsynaptic neuronal activities. The shape of the action potential plays an important role in determining the time window of spike timing dependent plasticity. The stringent time window requirement is due to the small time constants of both pre- and postsynaptic stimuli. In general, the time range of action potential is as large as 20 ms while that of glutamate flux is in the same order, too. In order for these two signals to interact with one another, the temporal proximity is required. The negatively correlated pre and postsynaptic stimulation may result into anti-Hebbian change in synaptic strength. The hyperpolarization and omega-shaped calcium dependent plasticity are the reasons behind such phenomena. Further development: The third class involves the application of STDP to neural network. Usually the two exponential decay functions for potentiated and depressed portions of the curves are used to exploration what network properties may emerge from such algorithm[23, 151]. How combination of different types of STDP may contribute to some emerging network properties is worth exploring.

6.4.1 Comparison with previous models

The unified model we propose is different from previous models in two essential aspects. First, the approach we took for modeling STDP is more systematic. Second, our model can explain wider range of experimental data than any previous ones. Table 6-3 summarizes this kinetic study and several previous models. Even the two previously developed biophysical models did not consider the synaptic pathways in details systematically as we do in developing this kinetic model. In brief, our model consists of three essential parts: backpropagation of action potentials, dual requirement for NMDA activation, and calcium dependent plasticity. Calcium dependent plasticity has usually been modeled by BCM rule which is crucial but not widely utilized in the modeling work listed. Especially missing in previous works is the accurate depiction of action potential backpropagation. After rigorously modeling various action potentials measured in experiments, we expand the applicability of this kinetic model to cover five different types of STDP. This unifying model has been validated by more sets of experimental data compared to previous models supported by two STDP data at most.

Table 6-2 Model comparison of this kinetic model with respect to previous ones in terms of several key attributes

	Model type	Underlying Mechanism	Data modeled	BCM rule incorporated
Kinetic model unifying spike timing dependent plasticity	biophysical	action potentials, NMDA receptors, and calcium dependent plasticity	five different types of spike timing dependent plasticity	Yes
NMDA receptor dependent bidirectional model[144]	biophysical	NMDA receptors and calcium control hypothesis	one symmetric STDP data with mixed LTP and LTD	Yes
STDP model with two calcium coincidence detector[78]	biophysical	NMDA receptors and voltage-gated calcium channels	one asymmetric STDP data following Hebbian rule	No
Potentiation-depression model[2]	phenomeno-logical	abstract potentiation and depression processes	two asymmetric STDP data following Hebbian rule	No
Exponential fitting functions [15]	phenomeno-logical	two separate exponential functions	one asymmetric STDP data following Hebbian rule	No

6.4.2 Limitations of the model

The applicability of the model is limited by the underlying assumptions we made while developing the model. Making these assumptions is necessary in extracting the essential pathways that contribute to STDP and in keeping the kinetic model mathematically tractable. The assumptions as well as the limitation associated with each assumption are listed below.

Assumption 1: gene regulation is insignificant compared to cytoplasmic signaling pathways throughout the time span of current experiments of STDP. That is, we only considered the signal transduction pathways in cytoplasm but not in nucleus. Upstream calcium signaling is generally considered sufficient to sustain early stage LTP or LTD, granted that late stage development involves also downstream genetic expression [76]. For instance, cAMP response element-binding (CREB) proteins, regulating transcription of certain memory-related genes [108], are crucial for late phase instead of early phase long-term potentiation. To explore longer lasting change of synaptic plasticity, including the transcription kinetics of key synaptic proteins is necessary.

Assumption 2: The spatial dependence of STDP response has not been considered. There is experimental evidence showing that different location of dendrites would result into wider or narrower window of LTD [33, 52]. Qualitatively, the result can be explained by our model: longer tails of back propagated action potentials widen the window within which they can interact with presynaptic stimuli. Therefore, the time constant of the LTD part of the STDP responses is changed. More rigorous modeling work requires detailed cable theory to deduce the functional relationship between stimulating different location of the dendrite and the consequent duration of hyperpolarization in action potentials.

Assumption 3: NMDA receptors were considered as the only gateway of calcium passage and a simple two-component model was used to generalize the reactions initiated by postsynaptic calcium. Reaction pathways have been greatly simplified to illustrate the essential mechanisms causing STDP but actual calcium signaling pathways are far more complex [30]. For instance, voltage gated calcium channels (VGCC) in addition to NMDA receptors allow calcium influx into postsynaptic compartments. Also other calcium-dependent reactions such as those involved in mitogen-activated protein kinase (MAPK) and cyclic adenosine monophosphate (cAMP) pathways, etc. can propagate the presynaptic and postsynaptic signals as well. Therefore, activities of these additional pathways may further influence the temporal responses of spike timing dependent plasticity.

Assumption 4: The waveforms of action potentials are modeled by Hodgkin-Huxley equations. Yet shapes of action potentials can vary significantly depending on the types of neurons and some of them cannot be well depicted by classical Hodgkin-Huxley equations. A summary classifying various action potentials with the corresponding models has been done by Izhikevich [72]. Using those models of action potentials or other more biophysically based ones may expand the applicability of this STDP kinetic model.

6.4.3 New experiments suggested by the model

Knowing the actual physiological reactions is crucial in pinpointing the molecular mechanism of associative learning and in engineering the synaptic plasticity and designing new experiments. The next step in elucidating the molecular mechanism is to identify the exact biomolecules that are involved in downstream calcium signaling. For instance, what are the kinase and phosphotate responsible for calcium dependent phosphorylation and dephosphorylation? Then how are these reactions cause activation and internalization of AMPA receptors, respectively? As suggested by Froemke et al., the time course of STDP is altered due to the difference of dendritic location or more specifically change in the time course of presynaptic response [52]. The associative learning deficits may be related to calcium signaling pathways. Therefore, it is possible that pharmacokinetic method can be used to control the calcium signaling and STDP tendency of certain synapses.

Table 6-3 The summary of nomenclature in Chapter 6

Symbols	Units	Definitions
C_{axon}, C_{dent}	$\mu F/cm^2$	Membrane capacitance of axon and dendrite, respectively
Ca	μM	Postsynaptic calcium concentration
ΔW	-	The change in synaptic strength
g_{inter}	μS	Inter-conductance between dendrite and axon
Glu	μM	Glutamate or glutamate concentration
$g_{NMDAmax}$	μS	Maximum conductance of NMDA receptors
I_{AMPAR}	nA	The current flow through AMPA receptors
I_K, I_{Na}	nA	The potassium and sodium current, respectively
I_{Laxon}, I_{Ldent}	nA	The leakage current at axon and dendrite, respectively
I_{NMDAR}	nA	The current flow through NMDA receptors
I_{pre}, I_{post}	nA	Presynaptic and postsynaptic stimuli current, respectively
k_{AMPARf}	s^{-1}	Rate constant of AMPA receptor activation
k_{AMPARb}	s^{-1}	Rate constant of AMPA receptor inactivation
k_{CaKf}, k_{CaKb}	s^{-1}	The forward and backward rate constant of kinase binding
k_{CaPf}, k_{CaPb}	s^{-1}	The forward and backward rate constant of phosphatase binding
K_{CaK}	μM	Sensitivity of calcium to calcium dependent kinase
K_{CaP}	μM	Sensitivity of calcium to calcium dependent phosphatase
k_{for}, k_{rev}	ms^{-1}	The forward and reverse rate constant of glutamate diffusion
K_{Glu}	μM	Glutamate association constant for half activation of NMDAR
k_{NMDAR}	mV^{-1}	The slope of NMDA receptor voltage dependence function
$k_{removal}$	ms^{-1}	The removal rate constant of glutamate
θ_d	μM	The calcium concentration bordering LTD and no change
θ_{min}	μM	The calcium concentration that leads to the lowest depression
θ_p	μM	The calcium concentration bordering LTP and LTD
V_{CaK}	$\mu M \cdot s^{-1}$	Proportional constant of CaK impact on AMPAR insertion
V_{CaP}	$\mu M \cdot s^{-1}$	Proportional constant of CaP impact on AMPAR removal
$V_{1/2}$	mV	Midway voltage at which g_{NMDA} becomes equal to $g_{NMDAmax}$
V_{axon}, V_{dent}	mV	Membrane potential at axon and dendrite, respectively

7 Calcium Signaling, Synaptic Plasticity, and Amyloid Fibrillation

The early stage of Alzheimer disease (AD) is often characterized by the deposition of amyloid beta (Aβ) plaques and the loss of ability to consolidate long-term memory [140]. The amyloid fibrillation process was modeled in Chapter 3 while Chapters 4, 5, and 6 are focused on the synaptic plasticity at different time scale. There should be linkage between formation of amyloid plaques and the impairment of synaptic plasticity. Therefore, this chapter is devoted to suggesting the potential causal effects between these two phenomena.

Current understanding with respect to the pathological species and disease mechanisms remain vague. The hypotheses of pathological species can be divided into two groups: those viewing Aβ as the rudimentary causes and those pointing to other non-Aβ species, instead. The first group believes the derivatives of amyloid peptides Aβ40 and Aβ42 as the pathological species. Especially their oligomeric aggregates can cause neurotoxicity, development of neurofibrillary tangles, or impairment of long–term potentiation (LTP) [163]. The hypotheses belonging to the second group are summarized together with their supporting evidences.

In the second section of this chapter, the effects of amyloid beta on long-term potentiation (LTP) are discussed because many experimental evidences suggesting so are available. Experimental data of such effect was explained with the calcium entrapment model we proposed. Based on the previous literature and our model for synaptic plasticity, the calcium signaling plays a determining role in regulating synaptic plasticity. Amyloid fibrils may disturb the calcium balance across the cell membrane and disable the synapse from getting long-term potentiated.

7.1 Theoretical hypothesis regarding pathological species

Amyloid fibrils have long been found in the brains of AD patients. Yet the detailed mechanisms and functional roles of Aβ fibrillation *in vivo* remain unclear. The current leading hypotheses regarding pathological species can be categorized into three groups: (1) Aβ fibrils as the main components of senile plague are the neurotoxic species. The accumulation of misfolded Aβ may initiate a cascade of reactions that eventually lead to synaptic dysfunction and neuronal loss [141] (2) Oligomers instead of fibrils are the pathogenic agents. These small molecules may react with membrane proteins and disturb the electrophysiological balance of neuron cells [127]. Soluble oligomers form of Aβ have been claimed to be the necessary and sufficient species to elicit cognitive functional deficit [31, 59]. There are in fact drugs undergoing clinical trials that act on slowing down or reversing the formation of oligomers. (3) All species involved in the fibrillgenesis pathways, including monomers, oligomers, and fibrils, are potential causes of various

neurodegerative diseases. Accordingly, the corresponding therapeutic approach would be to inhibit the upstream β-secretase or γ-secretase to prevent the formation of monomeric Aβ peptides in the first place. Finally, the memory loss in AD patients does not necessarily correlate strongly with the amount of Aβ plaque aggregation. Abnormality of synapse occurs before development of plaques and death of neurons [139]. Therefore, it is likely that the pathological species may not be amyloid fibrils but the reactive oligomers. Reactive oligomers may interact with membrane receptors to influence downstream signal transduction pathways.

There are still other disease mechanisms that do not regard derivatives of amyloid beta as pathological species. The first example is the tau hypothesis. Tau is an intracellular microtubule-associated protein that has been found in the neuronal tissues of some Alzheimer's disease patients [101]. The aggregated form of tau proteins become neurofibrillary tangles, neuritic plaques, which can potentially lead to aberrant cytoskeletal-cell organelle interactions and disruption of axonal transport [173]. Second, disturbance of the cholesterol balance is suspected to accelerate generation of amyloid beta. The strongest evidence comes from the medical findings that applying statin, the cholesterol lowering drug, can alleviate the symptom of AD patients [8, 85]. The third one is relatively broad claim which assert that imbalance of oxireductive reactions are the upstream causes of tangle or fibril formation. More specifically, transferrin fibrils are responsible for transporting human Fe^{III} which is involved in many oxidative and reductive physiological reactions [53, 149]. The fourth hypothesis is related to cholinergic transmission. Experimental evidence showed that synapses containing acetylcholine and glutamate are especially prone to be affected [95]. There are results from clinical trials that show acetylcholinesterase inhibitor, galantamine, can improve the conditions of AD patients [135]. However, there is no dominant theory of so far and the pathological mechanisms remain controversial. Therefore we decide to study the influence of Aβ fibrils on long term plasticity because we suppose there should be close relationship between the potential pathological species and the measurable metrics of memory formation capability.

7.2 Experimental evidence showing impairment of LTP

The amyloid peptides Aβ40 and Aβ42 have been suspected to cause neurotoxicity by development of neurofibrillary tangles that impair long–term potentiation (LTP) [163]. At the early stage of AD, one of the apparent symptoms is the loss of ability to consolidate long term memory. Thus, the coincidence of excessive formation of misfolded amyloid protein and impedance of long term plasticity change suggests the causal relationship between these two phenomena. There are experimental evidences demonstrate that applying Aβ either in vivo or in vitro results into long term depression (LTD) and internalization of AMPA receptors. Removal of AMPA receptors lead to weakened synaptic strength or even loss of dendritic spine [31, 71]. Loss of AMPA receptors further results into moderate level of calcium inflow which by the rule of calcium dependent synaptic plasticity would further weaken the synaptic strength. With the knowledge gained from modeling long term potentiation, the calcium signaling and AMPA receptors are key factors regulating LTP. Thus, understanding how amyloid derivatives alter the properties of membrane receptors and calcium dynamics would be helpful in explaining the functional roles they play.

A

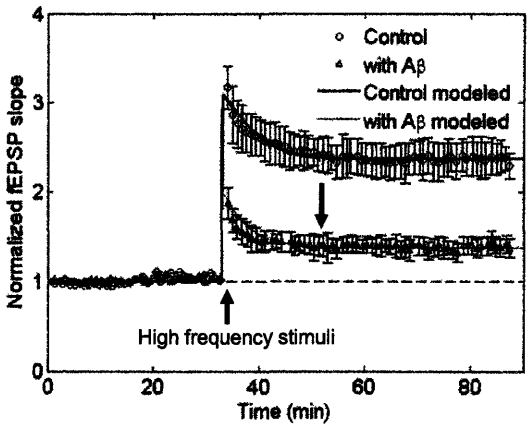

B

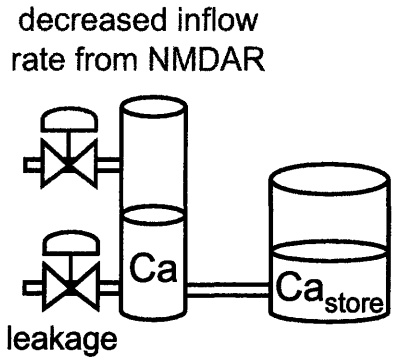

Figure 7-1 The disruption of long-term potentiation by the decreased inflow rate of calcium through NMDA receptors.
(A) The depressed response of LTP by Aβ in pyramidal neurons of rat hippocampus. The difference of parameters in modeling two curves is the amount of calcium inflow. Data source: Vitolo et al., 2002 [163]. (B) The simple analogy plot of plumbing with valves to indicates the potential influence of Aβ on the decreased inflow rate through NMDA receptors.

It has been found that the level of long term potentiation was impaired by the existence of amyloid–β peptide [163]. The sustainability of long term potentiation depends upon the ability of postsynaptic membranes to entrap sufficient intracellular calcium. We proposed that the pathological mechanisms are related to inhibition of membrane calcium channels or disturbance of membrane capacitance. The amount of calcium inflow to postsynapse can be calculated by Eq. (10) which we used to modeled LTP responses. The level of long term potentiation was experimentally found to be lowered by the existence of amyloid–β peptide as shown in Figure 7-1 [163]. It has been shown that Aβ species can regulate trafficking of NMDA receptor [150] so the conductance, g_{NMDAR}, is a function of Aβ concentration.

A

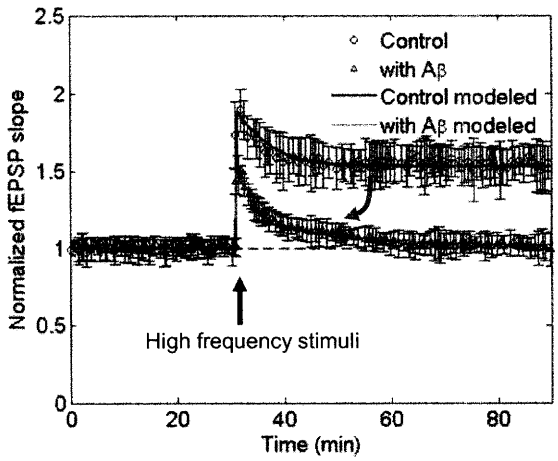

B

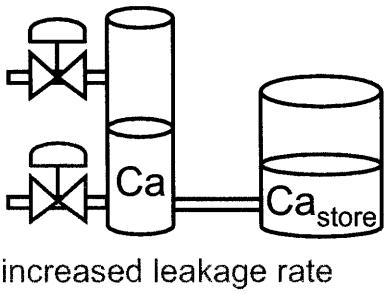

Figure 7-2 The disruption of long-term potentiation by the increase leakage rate of calcium.
(A) The depressed response of LTP by Aβ in the perforant pathway of the dentate gyrus. The difference of parameters in modeling two curves is the rate of calcium leakage. Data source: Wang et al., 2004 [163]. (B) The simple analogy plot of plumbing with valves to indicates the potential influence of Aβ on the increased leakage rate.

As for Figure 7-2, we used higher leakage rate, $I_{leakage}$, to successfully model curves of LTP influenced by Aβ peptides. Experimental evidence suggested that the oligomeric species of Aβ can form donut-shaped structure on membranes, increase leakage rate, and damage the normal function of cell membranes as capacitors [127, 168].

$$CaT \propto \int_{T_{stimuli}} I_{NMDAR} - I_{leakage} dt = \int_{T_{stimuli}} g_{NMDAR}\left(V_{membrane}, Glu\right) \cdot V_{membrane} - I_{leakage} dt \quad (10)$$

Furthermore, the decrease in the amount of calcium entrapped may influence the synaptic strength by altering the total number of AMPA receptors available for synaptic signal transmission. The possible mechanisms may include interference with the endocytosis of postsynaptic AMPA receptors such that the total concentration of AMPA receptors would decrease [71].

7.3 Conclusions regarding effects of amyloid fibrillation on synaptic plasticity

The influence diagram of amyloid fibrillation on synaptic plasticity is shown in Figure 7-3 according to the modeling results in this thesis as well as some references [71, 127]. Amyloid beta peptides aggregate and fibrillate following series reactions. Aβ oligomers may interact with neuronal cell membranes and perturb calcium homeostasis. Since calcium entrapment at postsynapse and the subsequent calcium-dependent reactions are

prerequisite conditions for sustainable change of synaptic plasticity, disruption of calcium balance may lead to failure to induce LTP. Unsustainable calcium level and decreased postsynaptic activities result into the removal or internalization of AMPA receptors. As a result, fewer number of active AMPA receptors, the indicator of synaptic conductance, signify lower efficacy of synaptic transmission [25]. Apoptosis may eventually ensue after long term inactivity of neurons due to internalization of AMPA receptors [169]. Yet one critical question remains under dispute. That is, what are the functional roles of Aβ peptides? The direction of research that may lead to the answer is further discussed in the following Future Work Chapter.

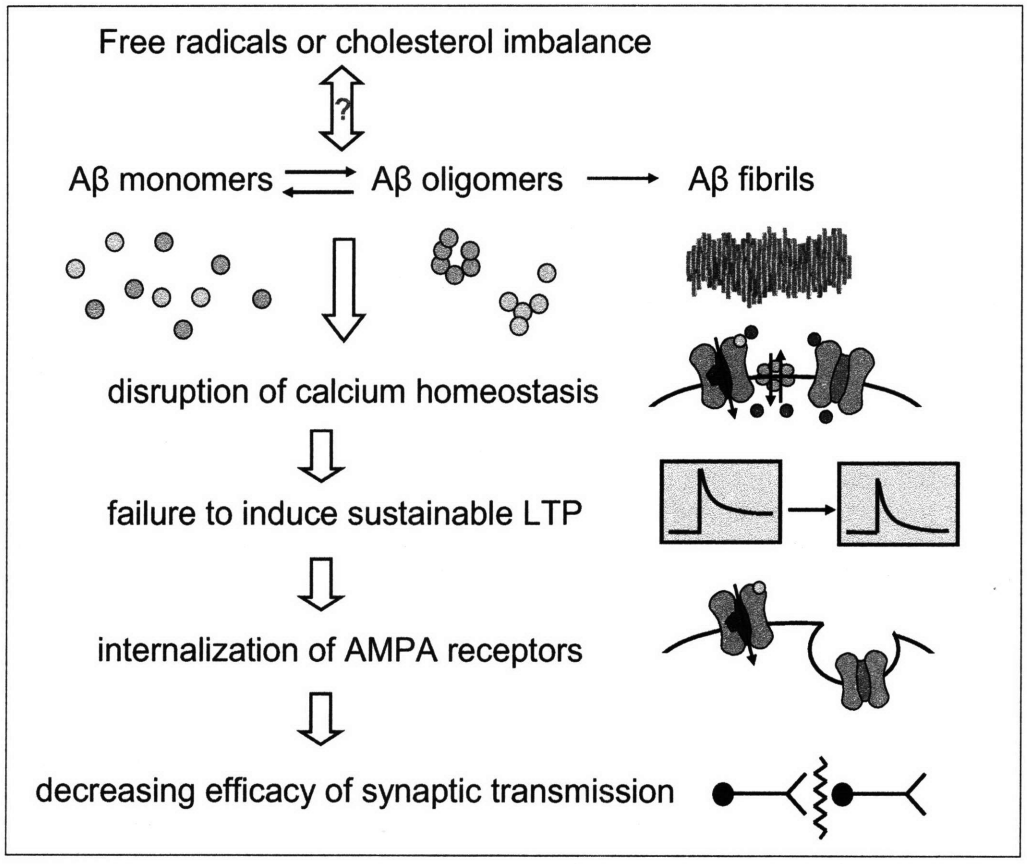

Figure 7-3 The influence diagram of amyloid peptides on synaptic plasticity.

8 Future Work

This thesis has demonstrated the usefulness of applying mathematical methodology and instilling physical insights into neurological systems. While neuroscience remains an active experimental research area, more theoretical work is needed to unify the experimental work and guide the design of further experiments. Based on the work that has been done in this thesis, we suggest the following four directions for further research.

8.1 Investigate the cause and effect between amyloid fibrils and neuronal activities

The roles of amyloid fibrillation in the pathology of many neurodegenerative diseases remain controversial. The biggest question remains whether amyloid plaques are the actual cause of cellular malfunctions or just the effect of upstream homeostatic imbalance. Temporal order in which various symptoms occur is a valuable indicator to distinguish between causes and effects. There are evidences showing that the occurrence of abnormal functions in hippocampal neurons precede appearance of amyloid fibrils in time [153]. They reported transport deficits in axons result into the facilitated proteolytic processing of β-amyloid precursor protein and the subsequent accumulation of β-amyloid peptides. The other issues worth exploring are the function roles or the toxic effects of amyloid fibrils. Several mechanisms of how accumulated amyloid fibrils become toxic to neurons have been suggested. For instance, it has been proposed that amyloid fibrils physically disrupt tissue architecture such as microtubules and cytoskeleton [82, 112]. Also some researchers suggest the puncture of cell membranes leads to ion imbalance and the subsequence abnormality in signal transduction pathways [127]. As for the functional roles, amyloid fibrils have been suggested as a modulator of cholesterol balance [86] or an activation of melanin polymerization [50]. The involvement of Aβ in apolipoprotein and cholesterol balance is also suggested [63]. Research directions along these lines would be helpful in clarifying the causal relationship between accumulation of amyloid plaques and failure of neuronal functions.

8.2 Spatial modeling of synaptic plasticity

The morphology of neuronal network in central nervous systems appears to be one of the most complex living structures. Compared to the intensive modeling work that has been geared toward transient experimental data, many experiments exploring spatial responses in neuronal tissues remain unexplained. To establish the structure-based functionality of neurons, modeling such spatial responses is necessary. Building modules for different types of neurons based on their morphologies is a step toward the realization of small physiologically based neuronal network. NEURON is a set of simulation software suitable for neurobiologists to predict the electrophysiological responses based on

the specifications of morphological data [67]. Although it is partially based on cable theory, the user interface is inflexible in terms of modifying the underlying equations. Therefore, Matlab Simulink® (The MathWorks, Natick, MA) is an alternative simulation environment for computational neuroscientists to implement the spatiotemporal model with hierarchical structure. By comparison, it is easier to check and update the equation-based algorithm in Matlab Simulink®.

8.3 Develop memory modules that incorporates gene expression

Some declarative long-term memory can last for months or years and be recalled at the onset of associated triggers. Although upstream signal transduction pathway is sufficient to elicit early stage of long term plasticity, synthesis of synaptic protein by translation of genes is a more likely way to leave permanent biomolecular memory traces. For instance, the binding between CREB (cAMP response element-binding) proteins and DNA is required in the consolidation of late phase long-term memories [76]. Theoretically, Hill equation is usually adopted to model the gene transcription activated by transcription factors [42]. Integration operation, compared to bistable theories, is more likely to be the true underlying algorithm by which synaptic plasticity can last robustly between neurons. Yet more experimental data beside graded long-term potentiation responses are necessary to test the statement. Experimentally, most of the current tests for long-term potentiation have run time of only a few hours which is too short compared to the time long-term memory can last. Therefore, experiments with longer time constants and detailed measurements of gene expression are critical in validating biophysical memory modules.

8.4 Apply biophysical models to neural network

What emerging properties and collective behaviors may arise from neural network consisting of individual neurons interconnected with one another remain an open question. The current basic elements used for constructing neural networks are oversimplified from a neurophysiological perspective. For instance, the spike timing dependent plasticity (STDP), one of the key underlying mechanisms of associative learning, is not reflected in generic neural network consisting of Hebbian synapses. Associative learning is a powerful ability for animals to generate new insights from collected information or experience. To imitate or even extend associative learning, the feature of STDP needs to be taken into account for the design of basic units in neural network. Other features missing from current neural network include the short-term and long-term synaptic plasticity as well as the firing of neurons.

Other intriguing questions include how neurons with different structure demonstrate distinct functionality and how the ensemble behavior may arise from heterogeneous neuronal network. There are more specific questions such as what response can be jointly demonstrated by a network of neurons connected by both depressing and facilitating synapses. In the meantime, what are the purposes of having synapses with these different attributes? Many of these questions are relevant to enhance our understanding on how learning and memory work yet they are not easy to answer. The joint efforts from both the experimental work and theoretical modeling are required to put pieces of puzzles together before we can see the whole picture of our brains.

9 Conclusions

Quantitative models not only explain experimental measurement but also suggest further design of experiments. There are substantial insights that can be gained the combination of theory and experiments in the field of memory formation. In this thesis, several physiology-based models have been built to elucidate the memory formation mechanisms and the kinetic process of amyloid fibrillation suspected as the cause of memory loss.

Amyloid fibrillation *in vitro* can be interpreted as a three-stage process. Amyloid proteins generally go through misfolding, nucleation, and elongation to become stable insoluble fibrils. Estimated by nonlinear least squares algorithms, the rate constants for nucleation were about ten million times smaller than those for fibril growth. These results, coupled with the positive feedback characteristics of the elongation process, account for the typical sigmoidal behavior during fibrillation. In addition, experiments with different proteins, various initial concentrations, seeding versus non-seeding, and several agitation rates were analyzed with respect to fibrillation using our new model. Moreover, according to *in vivo* findings, the existence of amyloid plaques in neurodegenerative patients is correlated with loss of ability to form short-term or long-term memory in the early stage of disease progression.

Models for short-term and long-term plasticity have been built, respectively with results matching experimental data well. The main reason for short-term depression is depletion of neurotransmitter vesicle while that for short-term facilitation is the enhanced transmitter release due to buildup of residual calcium. As for long-term plasticity, the calcium entrapment model we proposed outputs results that agree with graded long-term potentiation responses triggered by multiple trains of stimuli. In addition, the frequency dependent long term plasticity can be explained by the same model coupled with the calcium dependent protein kinase and phosphatase. This suggests the importance of postsynaptic calcium and the subsequent downstream signaling in sustaining the enhancement of synaptic conductance. Furthermore, in the late ninety's plasticity was found to depend not only on the frequency of stimuli but also on the relative spike timing between pre- and postsynaptic stimuli.

Ever since its discovery, spike timing dependent plasticity (STDP) has become a new experimental protocol for eliciting change in synaptic plasticity. Yet there was few theoretical work that can well clarify its underlying mechanism until we set up a unifying model that can cover quite a variety of STDP responses. Most of the responses can be interpreted as the results of a two-step process. First, the activation of NMDA receptor-gated calcium ion channels requires both release of glutamate from presynase and postsynaptic membrane depolarization. The relative timing between these two signals determines the amount of calcium ion flowing into postsynapse. Second, the level of postsynaptic calcium in turn determines the synaptic conductance through calcium signaling. Again, the importance of calcium ions in synaptic plasticity and thus memory formation is indicated.

The toxic effects and functional roles of Aβ fibrillation in human brains remain controversial. With the knowledge gained from modeling long term synaptic plasticity, we realize that calcium signaling and AMPA receptors are key factors regulating memory formation. Therefore, we support the hypothesis that the oligomeric form of amyloid derivatives perforates neuron membranes and disturbs the intracellular calcium balance. Change in the amount of calcium entrapped in neurons in turn influences the synaptic strength by altering the total number of AMPA receptors available for synaptic signal transmission. The abnormal variation in synaptic strength as well as neuronal activities can have significant impact on the triggering immune systems and determining cell fate. Further work to clarify the casual effects among amyloid fibrillation, disease symptoms, and physiological reaction pathways is an important step toward better understanding in the fundamental causes of memory loss and the pathology of neurodegenerative diseases.

Appendix A Supplemental Materials of Amyloid Fibrillation Model

This supplement contains five sections that support Chapter 3: Modeling Amyloid Fibrillation in the thesis. 1. Details of the methods used for parameter estimation, 2. Comparisons of the model predictions against a simple empirical model. 3. A sensitivity analysis study that identifies key variables. 4. The MATLAB® [110] computer codes used to implement the parameter estimation and numerical solution of the fibrillation kinetics. 5. The abstract of the paper entitled "Osmolyte Controlled Fibrillation Kinetics of Insulin" which deals with additive-induced heterogeneous fibrillation. It is the manuscript we wrote together with Nayak and Prof. Belfort from Rensselaer Polytechnic Institute.

A.1 Parameter estimation

Nonlinear least squares regression [137] was used to estimate the model parameters. The mathematical statement of the optimization problem including the physical constraints is of the form:

$$\begin{aligned} &\underset{\underline{\theta}}{Min} && \Phi(\underline{\theta}) = \sum_{i=1}^{n_{exp}} \left[Y_i - f(t_i;\underline{\theta}) \right]^2 \\ &Subject\ to && \underline{\theta} \geq \underline{0} \end{aligned} \tag{A.1}$$

where $\Phi(\underline{\theta})$ is the objective function to be minimized and $\underline{\theta}$ is vector of n_p parameters to be estimated from Y_i, the measurements of fibril amount at the n_{exp} time points. The solution to the model built in the main paper describing the kinetics of fibril concentration at the time points is denoted by f. A local minimum for Eq. (A.1) can be found by solving the system of algebraic equations.

$$g_j(\underline{\theta}) = \frac{\partial \Phi}{\partial \theta_j} = -2 \sum_{i=1}^{n_{exp}} \left[Y_i - f(t_i;\underline{\theta}) \right] \left(\left. \frac{\partial f}{\partial \theta_j} \right|_{t_i} \right) = 0 \quad ; j = 1,...,n_p \tag{A.2}$$

Both the optimization problem and the embedded differential equations, describing the kinetics, were solved with MATLAB® and its library programs **nlinfit**, **nlparci**, and **nlpredci**. (A copy of the MATLAB code is included in Section 4). The algebraic equation solver **nlinfit** uses the Levenberg-Marquardt method to solve the nonlinear system Eq. (A.2) After a limited number of iterations, the calculation converged to the local minimum. Different starting points were used to ensure that the solution to Eq. (A.2) was indeed a global minimum.

Three different metrics were used to assess the goodness-of-fit for the parameters $\underline{\theta}$. One was the coefficient of determination (R^2), which is the ratio of sum of squared errors due to

regression to the total sum of square errors. Another was the Root Mean Square Error (RMSE). A third measure of the quality of the statistic fit were the confidence intervals for each of the estimates. Several computational steps were required to calculate the standard error of the confidence intervals. First, the population variance s^2 was estimated from the residual errors,

$$s^2 = \frac{1}{\nu}\sum_{i=1}^{n_{exp}}\left[Y_i - f(t_i;\hat{\underline{\theta}})\right]^2 \tag{A.3}$$

where ν is the rank of design matrix and equal to the number of experimental points minus the number of parameters ($n_{exp} - n_p$). The half-width confidence interval, given the level of significance, was calculated using

$$\tilde{\theta}_j = \hat{\theta}_j \pm t_{\nu,\alpha/2} \cdot s \cdot \left[\left(X^T X\right)^{-1}\right]_{jj}^{1/2} \tag{A.4}$$

where $t_{\nu,\alpha/2}$ is the Student t-distribution with degree of freedom ν and significance level α. The significance level used here was 0.317 which corresponds to one standard deviation. X is the linearized design matrix also known as the Jacobian.

$$X_{ij} = \left.\frac{\partial f}{\partial \theta_j}\right|_{t_i} \tag{A.5}$$

Originally there were two forward and two reverse rate constants to be determined but after exploring parameter variations by sensitivity analysis, we found that k_{nu-} did not influence the response significantly (Figure A-2) and so the estimated parameter vector $\underline{\theta}$ has the components [$k_{nu,1}$, $k_{fb,1}$, k_{fb}]

A.2 Comparison of the Kinetic Model against an Empirical Function

In many previous experimental studies regarding fibrillation (see [117] for example), the sigmoidal responses were fitted with an empirical expression of the form.

$$Y = y_i + m_i t + \frac{y_f + m_f t}{1 + e^{-[(t-t_0)/\tau]}} \tag{A.6}$$

where the coefficients (y_i, m_i, y_f, m_f, t_0, τ) were adjusted to fit the time response. Given the often good match to the data it is natural to ask if there is any physical basis for the model.

In general, the set of differential equations defined in our model need to be solved numerically except for some special cases. One is when the natural insulin hexamer is

assumed to dissociate instantaneously and the critical size n is as small as two. Under these assumptions there are two chemical species left: soluble monomers and insoluble fibrils. Since the kinetic model now consists of only two distinct stages (Eq. (A.7)): the slow nucleation process, and the fast fibrillation stage, the nucleation and the fibril elongation reactions both follow second order kinetics.

$$\begin{aligned} A_1 + A_1 &\xrightarrow{k_{nu,1}} F \\ A_1 + F &\underset{k_{fb-}}{\overset{k_{fb,1}}{\rightleftharpoons}} F \end{aligned} \tag{A.7}$$

In this model fibril dissociation is first order with respect to fibril concentration.

$$\frac{dF}{dt} = k_{nu,1}A_1^{\,2} + k_{fb,1}FA_1 - k_{fb-}F \tag{A.8}$$

If the fibrils were on average composed of N monomers then the time derivative of monomer concentration should have been N times as large as that of fibril concentration.

$$\frac{dA_1}{dt} = -N\frac{dF}{dt} \tag{A.9}$$

Under these conditions the monomer concentration, A_1 could be expressed in terms of initial concentrations (A_0) and F by a mass balance; thus, the time derivative of fibril now becomes a single variable differential equation.

$$\begin{aligned} \frac{dF}{dt} &= k_{nu,1}(A_0 - NF)^2 + k_{fb,1}F(A_0 - NF) - k_{fb-}F \\ &= (N^2k_{nu,1} - Nk_{fb,1})F^2 + (k_{fb,1}A_0 - 2Nk_{nu,1} - k_{fb-})F + k_{nu,1}A_0^{\,2} \end{aligned} \tag{A.10}$$

Since, at steady state, the right hand side of Eq. (A.10) was equal to zero, it is a second order algebraic equation in F and we know that the system had at least one stable steady state, so there must be two real roots (r_1, r_2) [154].

$$r_1, r_2 = \frac{-(k_{fb,1}A_0 - 2Nk_{nu,1} - k_{fb-}) \pm \sqrt{(k_{fb,1}A_0 - 2Nk_{nu,1} - k_{fb-})^2 - 4(N^2k_{nu,1} - Nk_{fb,1})k_{nu,1}A_0^{\,2}}}{2(N^2k_{nu,1} - Nk_{fb,1})} \tag{A.11}$$

The set of differential equations were simplified into the form explicitly showing the loci of two roots; one the attractor and the other the repeller (say for $r_1 < r_2$) as in Error! Reference source not found..

$$\frac{dF}{dt} = (N^2 k_{nu,1} - N k_{fb,1})(F - r_1)(F - r_2) \tag{A.12}$$

$$\frac{dA_1}{dt} = (k_{fb,1} - N k_{nu,1})(A_1 - (A_0 - N r_1))(A_1 - (A_0 - N r_2)) \tag{A.13}$$

Each time derivative is a parabolic function of its specie concentration where one is concave and the other is convex in schematic Figure A-2. Referring to Figure A-2 (left), we can track the fibrillation response from a different perspective. At first, the fibril concentration was zero and *dF/dt* was positive. This gave the accelerated concentration until it reached the stationary point which corresponded to the inflection point of $F(t)$. Then, the fibril concentration kept on increasing but in a decelerated way until it reached the stable steady state (saturation condition). A similar argument can be made with respect to monomer concentration by using Figure A-2 (right).

Eq. (A.13) has a similar form to the Verhurst equation [162] and can be solved analytically to give

$$F(t) = r_1 + \frac{r_2 - r_1}{1 + e^{-(t - t_0)/\tau}} \tag{A.14}$$

where the constants are given by

$$\frac{1}{\tau} = (N k_{fb,1} - N^2 k_{nu,1})(r_2 - r_1) \tag{A.15}$$

$$t_0 = \tau \ln(-r_2 / r_1) \tag{A.16}$$

Given that there were no fibrils present at the beginning of the experiment, the analytic solution to the equation shares the same functional form as Eq. (A.6) when m_i and m_f are equal to zero. The models Eq. (A.6) and Eq. (A.14) can now be seem to be related to several experimentally measurable parameters. First, $1/\tau$ is the apparent growth rate constant k_{app}. Second, t_0 is the inflection point where the second order derivative of $F(t)$ equal to zero. Finally, the delay time can be calculated as t_0-2τ.

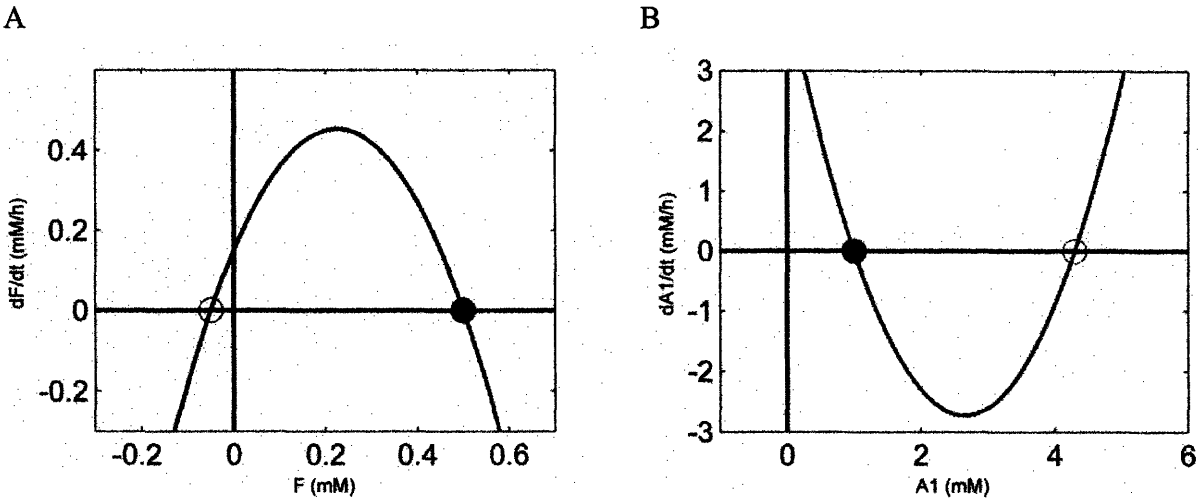

Figure A-1 (A) Time derivative of the fibril concentration as a function of the fibril concentration. (B) Time derivative of the monomer concentration as a function of the monomer concentration.
Solid circles are attractors (stable steady states); open circles are repellers (unstable steady states).

A.3 Sensitivity analysis

Sensitivity analysis was conducted to evaluate the impact of each of the four parameters. The partial derivative of the model response with respect to the j-th parameter was computed by a finite difference method.

$$\frac{\partial f(\underline{\theta})}{\partial \theta_j} \cong \frac{f(\theta_j + \Delta\theta_j) - f(\theta_j)}{\Delta\theta_j} \tag{A.17}$$

To obtain a good estimate of the first derivate as well as to minimize the round-off error, the optimal value of $\Delta\theta_j$ was chosen to be 10^{-4} of θ_j. Due to the fact that rate constants estimated in this study had different units and their values span several orders of magnitude, the logarithmic from of Eq. 17 provided a better way to compare the relative contributions,

$$\frac{\partial \ln f(\underline{\theta})}{\partial \ln \theta_j} = \frac{\theta_j}{f} \frac{\partial f(\underline{\theta})}{\partial \theta_j} \tag{A.18}$$

Figure A-2 shows the results of logarithmic sensitivity analysis as a function of time demonstrating the impact of each parameter at different stages of fibrillation. Notice that changing the value of k_{nu-} several fold did not affect the Y response significantly compared with perturbing the other parameters so k_{nu-} was not considered in the parameter

estimation. The rate constant $k_{nu,1}$, followed by k_{fb-} was the most significant parameter influencing the earlier stage of fibrillation; thus, the delay time is determined by both $k_{nu,1}$ and k_{fb-}. Finally, the equilibrium gain of the signal roughly depended on the products of $k_{nu,1}$ and k_{fb-} divided by $k_{fb,1}$.

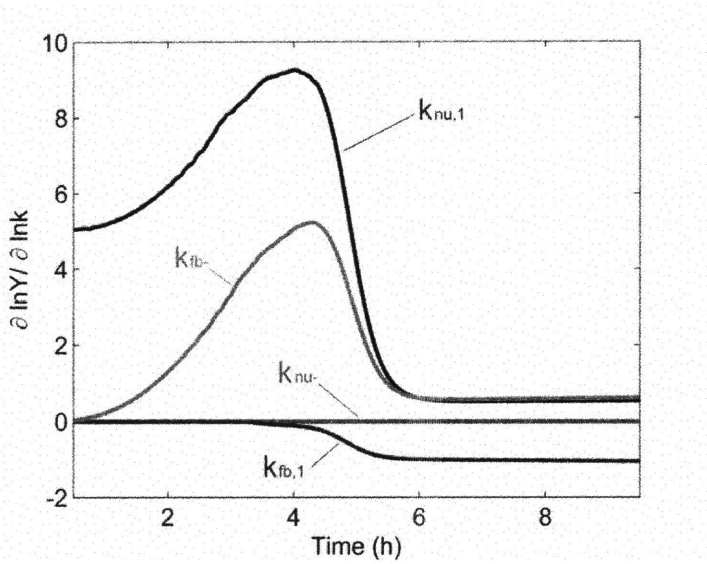

Figure A-2 $\partial lnY/\partial lnk$ represents the logarithmic sensitivity analysis of the rate constant influence on the fibrillation response around the standard condition.
Note that Y is ThT fluorescence intensity and rate constants include $k_{nu,1}$ (black), k_{nu-} (red), $k_{fb,1}$ (blue), and k_{fb-} (magenta).

A.4 MATLAB® Codes of the Model

The results shown in Chapter 3 of the thesis: Modeling Amyloid Fibrillation were obtained using MATLAB® [110] and two m-file functions: **`solveode_fibril`** and **`dA_dt=ode_fibril(t,A,n,theta)`**. The function **`solveode_fibril`**, sets up the parameters for the kinetic model and then solves the resulting set of differential equations using the MATLAB® function **`ode23s`**. The outputs include the fibrillation response and oligomer concentrations as functions of time. The right hand side of the differential equations are evaluated using the function **`dA_dt = ode_fibril(t,A,n,theta)`**.

```
function solveode_fibril;
% % % % % % % % % % % % % % % % % % % % %  % % % % % % % % % % % % % %
% This function solves the set of differential equations defined @    %
% ode_fibril, and plots sigmoidal curves of fibril and oligomer conc.%
% % % % % % % % % % % % % % % % % % % %  % % % % % % % % % % % % % % %

% The following is the list of parameters and initial conditions
n=6; % Critical number of monomers to form a neucleus
b=6e5; % The proportional constant of signal response
theta=[3.54e-2,2.73e6,1.94e3]; % The rate constants [knu1, kfb1, kfb_]
hex0_mg=2; % Initial insulin wt conc. of insulin hexamers (mg/mL)
insulin_kD=6; % The molecular weight of insulin monomer (kD)
```

```
hex0_mM=hex0_mg/insulin_kD/6; % Convert unit from mass to molar conc(mM)
Y0=zeros(1,n+1); % The initial concentration of insulin hexamers (mM)
Y0(n+1)=hex0_mM;

% Run the simulation and plot the results
close all
slots=201; % Specify number of simulation points
t_range=linspace(0,8,slots); % Specify the time scale vector
[t_val,Y_val]=ode23s(@ode_fibril,t_range,Y0,[],n,theta);
signal=Y_val(:,n)*b; % Fluores Signal is proportional to fibril conc.

% Plot the data of UV-vis signal and simulation results
plot(t_val, signal,'b-','LineWidth',1.5);
xlabel('Time (h)','FontSize', 14);
ylabel('UV-vis absorbance @ 600 nm','FontSize', 14);

% Plot the concentration of natural insulin hexamer, monomer, and dimer
figure
plot(t_val, Y_val(:,n+1)*6,'r:',t_val, Y_val(:,1),'b-',t_val, ...
Y_val(:,2),'k-.','LineWidth',1.5);
legend('natural hexamer','monomer','dimer');
xlabel('Time (h)','FontSize', 14);
ylabel ('Cluster Concentration (mM)','FontSize', 14)

% Plot the concentration of 3-mers, 4-mers, and 5-mers
figure
plot(t_val, Y_val(:,3),'r:',t_val, Y_val(:,4),'b-',t_val, Y_val(:,5), ...
'k-.','LineWidth',1.5);
legend('3-mer','4-mer','5-mer','location','southeast');
xlabel('Time (h)','FontSize', 14);
ylabel ('Cluster Concentration (mM)','FontSize', 14)


function dA_dt=ode_fibril(t,A,n,theta)
% % % % % % % % % % % % % % % % % % % % % % % % % % % % % % % % % % % % % %
% Defines the set of ODEs to be solved to simulate fibrillation      %
% A(1~n-1) is the vector of i-mer concentrations (i=1~n-1)           %
% A(n) is fibril conc. and A(n+1) is natural hexamer conc.           %
% t is time and dA_dt is the first order derivatives of A vector     %
% n is the critical size of clusters and is assigned to be 6         %
% theta vector is the set of rate constants [knu1, kfb1, kfb_]      %
% % % % % % % % % % % % % % % % % % % % % % % % % % % % % % % % % % % % % %

dA_dt=zeros(size(A)); % First order derivatives of i-mer concentrations
Jnu=zeros(size(A)); % Flux of i-th nucleation reaction
Jfb=zeros(size(A)); % Flux of i-th fibrillation reaction

% The following is the list of rate constants
khex=3; % Forward rate constant of insulin hexamer dissociation
knu=ones(n,1)*theta(1); % First foward nucleation rate constants
for i=1:n-1
   knu(i)=theta(1)/2*(1+i^(-1/3)); % Correct knu(i) by Stokes-Einstein
Eq.
end
knu_=ones(n,1)*1e-3; % Reverse nucleation constants
kfb=ones(n,1)*theta(2); % First forward fibrillation rate constant
for i=1:n-1
```

```
   kfb(i)=theta(2)*i^(-1/3); % Correct kfb(i) by Stokes-Einstein Eq.
end
kfb_=ones(n,1)*theta(3); % Reverse fibrillation rate constant

% Definitions of reaction fluxes Jhex, Jnu, and Jfb
Jhex=khex*A(n+1); % The flux of hexamer decomposition reaction
for i=1:n-1
   Jnu(i)=knu(i)*A(1)*A(i)-knu_(i)*A(i+1); % The flux of nucleation rxn
   Jfb(i)=kfb(i)*A(n)*A(i)-kfb_(i)*A(n); % The flux of i-mer elongation
end

% There are n+1 equations representing the conc. change of n+1 species
dA_dt(1)=6*Jhex-sum(Jnu(1:n-1))-Jnu(1)-Jfb(1); % Derivative of [monomer]
for i=2:n-1 % from dimer to (n-1)-mer
   dA_dt(i)=-Jnu(i)+Jnu(i-1)-Jfb(i); % Derivatives of [oligomer]
end
dA_dt(n)=Jnu(n-1); % Derivative of fibril concentration
dA_dt(n+1)=-Jhex; % Derivative of insulin hexamer concentration
```

A.5 Abstract of osmolyte controlled fibrillation kinetics of insulin

How proteins, implicated in amyloid diseases, impart toxicity is unknown. What is known is that they are converted from their native-fold to long -sheet-rich fibrils in a typical sigmoidal time-dependent curve. This reaction process from monomer or dimer to oligomer to nuclei and then to fibrils is the subject of intense study. Here, we probe this reaction process using a model protein, human insulin, through the addition of a comprehensive series of stabilizing and destabilizing osmolytes and quantify the analysis using our new kinetic rate model. The results are then collated into a cogent explanation using the preferential exclusion and accumulation of osmolytes away from and at the protein surface during nucleation, respectively. Both the heat of solution and the neutral molecular surface area of the osmolytes correlate linearly with two fitting parameters of the kinetic rate model, i.e. the lag-time and the nucleation rate prior to fibril formation. Also, the action of osmolytes on the reaction appears to be independent and additive. These kinetic and thermodynamic results support the preferential exclusion model and the existence of oligomers including nuclei and larger structures that could induce toxicity.

Appendix B Supplemental Materials of STDP

This supplement contains four sections that support Chapter 6: Modeling Spike Timing Dependent Plasticity in the thesis. 1. The action potential backpropagation was modeled by interconnected compartment models of axon and dendrite. 2. A different version of Hodgkin-Huxley equations was developed to depict action potentials with depolarization after potential. 3. Biophysical model is included to explain the voltage dependence of NMDA receptor activities. 4. A simple diffusion model is used to link presynaptic stimuli to glutamate concentration.

B.1 Model action potential backpropagation

For modeling the dynamics of action potential backpropagation, we incorporated two parts of the spiking neuron: the axon and the dendrite into the multi-compartment model [34]. The scheme of equivalent circuit is shown in FigureB-1. The axon is assumed to be where the action potentials (APs) are initiated. How injection of external current triggers APs was modeled by Hodgkin-Huxley equations.

$$C_{axon}\frac{dV_{axon}}{dt} = -I_{Na} - I_K - I_{Laxon} + I_{post} + I_{inter} \tag{B-1}$$

Where the sodium, potassium, and leakage currents at axon are expressed in Eq. (B-2). The variable m, h, and n are gating variables while E_{Na}, E_K, and E_{Laxon} are the reverse membrane potentials. Further details and parameter values can be found in [10, 68].

$$\begin{aligned} I_{Na} &= \bar{g}_{Na} m^3 h\left(V_{axon} - E_{Na}\right) \\ I_K &= \bar{g}_K n^4 \left(V_{axon} - E_K\right) \\ I_{Laxon} &= \bar{g}_{Laxon}\left(V_{axon} - E_{Laxon}\right) \end{aligned} \tag{B-2}$$

The dendrite is where the signals from presynaptic and postsynaptic neurons converge. First, the neurotransmitters released from presynaptic neurons bind with the membrane receptors on postsynaptic dendrites. The binding increases the opening probability of receptor-gated ionic channels. Second, the initiated postsynaptic APs can get back propogated to influence the charge balance at dendrites through an interconnecting conductance we call g_{inter}.

$$C_{dent}\frac{dV_{dent}}{dt} = -I_{NMDAR} - I_{AMPAR} - I_{Ldent} - I_{inter} \tag{B.3}$$

The current interflowing between axon and dendrite can be calculated as the product of the conductance with the potential difference between two compartments based on Ohm's law.

$$I_{inter} = g_{inter}(V_{dent} - V_{axon}) \tag{B.4}$$

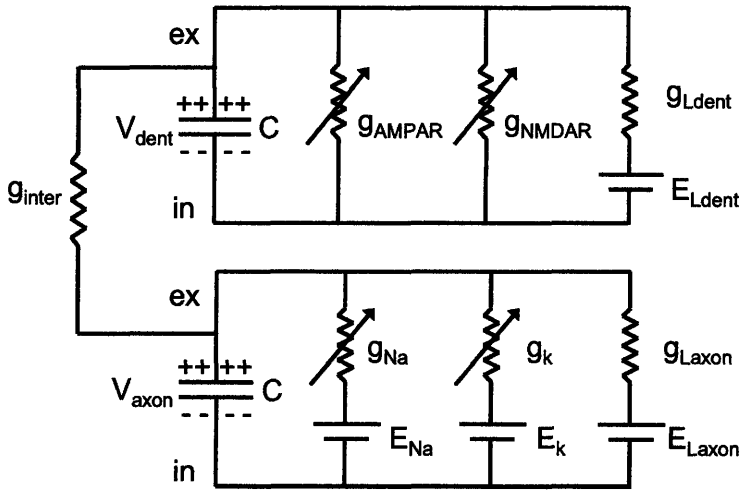

Figure B-1 The equivalent circuit for computing membrane potentials at dendrite and axon. Two compartments are linked by inter-compartmental conductance (g_{inter}).

B.2 Modified Hodgkin-Huxley equations for depolarization after potential

The shapes of action potentials vary significantly, depending on the types and locations of neurons. Although the output of Hodgkin-Huxley equations represents one major type of action potential, it cannot account for all the classes of action potential. Therefore, various spiking models have been developed independently or based on the H-H equations. To model the experimental data of various types of STDP, a precise simulation of action potentials initiated at the neurons of interest is necessary.

Several types of neurons mentioned in the manuscript demonstrate depolarization after potential (DAP) behavior. These neurons, at the repolarization stage, depolarize instead of hyperpolarize once reaching the resting potential, which is -65 mV according to H-H equations. Therefore, the level of membrane potential does not drop below the steady state value. To implement the introduction of DAP into H-H model, we decided to reverse the hyperpolarization part of the action potential whenever the membrane potential V_m is smaller than -65 mV. The constant k_{DAP} is added to control the degree of depolarization after potential. The Matlab® codes to execute the algorithms are as follow and the comparison between the output of classical H-H model and that with DAP behavior is shown in Figure B-2A and Figure B-2B.

```
IF  Vm < -65

    THEN Vm = -65 + kDAP * (-65 - Vm)

ELSE

    Vm = Vm

END
```

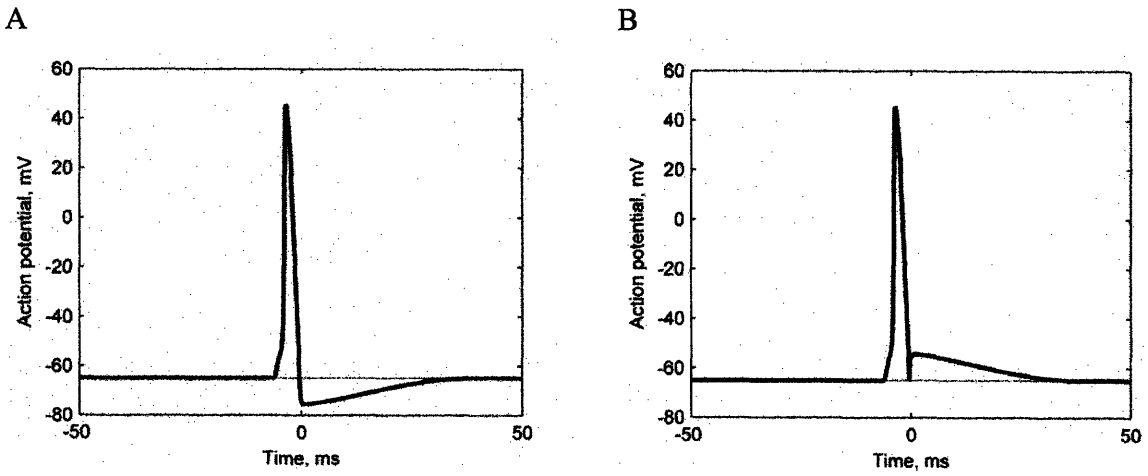

Figure B-2 The action potential initiated by stimulus based on two different versions of Hodgkin-Huxley model.
(A) The output by classical H-H model. (B) The output of H-H model with DAP behavior ($k_{DAP} = 1$).

B.3 The voltage dependence of NMDA receptor activities

The conductance of NMDA receptor-gated ion channel is included in Chapter 6. There is glutamate dependence as well as voltage dependence. This section is devoted to explain the functional form of the voltage dependence as shown in Eq. (B.5).

$$g_{NMDAR}(V) = \frac{g_{NMDARmax}}{1 + e^{-k_{NMDA}(V - V_{1/2})}} \tag{B.5}$$

It is assumed that the receptor-gated ion channels either exist in the open or close state. The conductance of NMDA receptors (g_{NMDAR}) is correlated with the gating variable n which is the proportion of ion channels that exists in the open state. The transition between open and close gates is assumed to follow first order kinetics with the opening rate constant $\alpha_n(V)$ and closing rate constant $\beta_n(V)$ as shown in Eq. (B.6).

$$(1-n) \underset{\beta_n(V)}{\overset{\alpha_n(V)}{\rightleftarrows}} n \tag{B.6}$$

The rate of change in n is equal to the production rate minus the consumption rate as shown in Eq. (A.2) which can be rewritten in the standard form of linear first order differential equation.

$$\begin{aligned} \frac{dn}{dt} &= \alpha_n(V)(1-n) - \beta_n(V)n = \alpha_n(V) - \left(\alpha_n(V) + \beta_n(V)\right)n \\ \tau_n(V)\frac{dn}{dt} &= n_\infty(V) - n \end{aligned} \tag{B.7}$$

The parameters $n_\infty(V)$ and $\tau_n(V)$ are defined as follows:

$$\begin{aligned} \tau_n(V) &= \frac{1}{\alpha_n(V) + \beta_n(V)} \\ n_\infty(V) &= \frac{\alpha_n(V)}{\alpha_n(V) + \beta_n(V)} \end{aligned} \tag{B.8}$$

The state transition with rate constant $\alpha_n(V)$ is assumed to be rate-limited by barriers requiring thermal energy. The Arrhenius equation can be use to predict the dependency of rate constant on temperature as well as on voltage [34]. The energy required to cross the membrane (E_α) is the products of the charge (q), voltage difference (V), and proportional constant (B_α). Also the same for $\beta_n(V)$.

$$\begin{aligned} \alpha_n(V) &= A_\alpha \exp(-E_\alpha / k_B T) = A_\alpha \exp(-qB_\alpha V / k_B T) = A_\alpha \exp(-B_\alpha V / V_T) \\ \beta_n(V) &= A_\beta \exp(-B_\beta V / V_T) \end{aligned} \tag{B.9}$$

After inserting the expression of $\alpha_n(V)$ and $\beta_n(V)$ into Eq. (B.8), we get the expression of maximum gating variable, $n_\infty(V)$ with the same functional form to that of $g_{NMDAR}(V)$. Therefore, the Arrhenius equation is the biophysical explanation of voltage dependent conductance of NMDA receptors.

$$g_{NMDAR}(V) \propto n_\infty(V) = \frac{1}{1 + (A_\beta / A_\alpha)\exp\left((B_\alpha - B_\beta)V / V_T\right)} \tag{B.10}$$

B.4 Diffusion model for converting presynaptic stimuli to glutamate concentration

Presynaptic stimuli cause release of glutamate as neurotransmitters which diffuse across synaptic cleft to reach postsynaptic receptors. Theoretically spatiotemporal diffusion models coupled with reactions can describe the transportation of glutamate at synapse but the details of setting up and solving complex partial differential equations deviate from the scope of this study. Instead, the relationship between glutamate concentration and the presynaptic stimuli (I_{pre}) can be assumed to follow a simple two compartment model for simplicity (Figure B-3A). At first, we suggest that presynaptic glutamate (Glu_{pre}) is transported through synaptic cleft to become available (Glu) to postsynaptic receptor; the reverse direction is also possible. Initially without stimulation, the concentrations of Glu and Glu_{pre} are both zero. The forward and reverse rate constants of transportation are k_{for} and k_{rev}, respectively. Meanwhile, glutamate is constantly removed by glutamate transporter with rate constant k_{remove}.

$$\begin{aligned}\frac{dGlu_{pre}}{dt} &= -k_{for}Glu_{pre} + k_{rev}Glu + I_{pre} \\ \frac{dGlu}{dt} &= k_{for}Glu_{pre} - k_{rev}Glu - k_{remove}Glu\end{aligned} \tag{B.11}$$

$$\frac{d}{dt}\begin{pmatrix} Glu_{pre} \\ Glu \end{pmatrix} = \begin{pmatrix} -k_{for} & k_{rev} \\ k_{for} & -(k_{for}+k_{remove}) \end{pmatrix}\begin{pmatrix} Glu_{pre} \\ Glu \end{pmatrix} + \begin{pmatrix} 1 \\ 0 \end{pmatrix} I_{pre} \tag{B.12}$$

With two equations and two unknowns, the linear system of ordinary differential equation with known initial conditions can be integrated. Given I_{pre} of amplitude 1nA lasting for 1 ms as an input, glutamate concentration rises rapidly and decreases gradually as shown in Figure B-3B. The parameter values of k_{for}, k_{rev}, and k_{remove} are estimated and summarized in Table B-1.

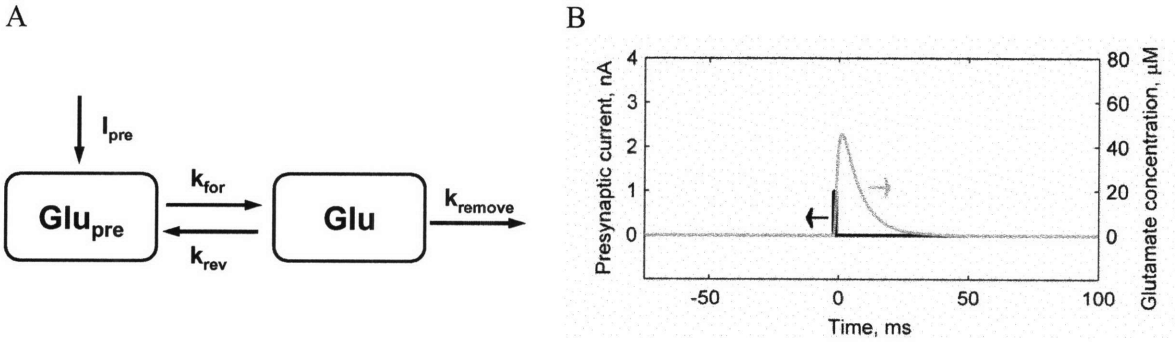

Figure B-3 (A)The scheme of two compartment model for converting presynaptic current (I_{pre}) into glutamate concentration (Glu). (B) The example presynaptic current input and glutamate concentration response.

Table B-1 Common parameter values in the model, independent of the STDP types

Parameters	Units	Values
$g_{Ldendrite}$	μS	3.0e-4
g_{inter}	μS	3.5e-4
$g_{NMDAmax}$	μS	1.0e-3
g_{AMPA}	μS	2.0e-4
k_{AMPARf}	s^{-1}	0.47
k_{AMPARb}	s^{-1}	1.0
k_{for}	ms^{-1}	0.3
k_{remove}	ms^{-1}	0.4
k_{rev}	ms^{-1}	0.3
k_{NMDA}	mV^{-1}	0.1
$V_{1/2}$	mV	-30

Appendix C Hodgkin-Huxley Equations

The Hodgkin-Huxley equations belong to conductance-based compartment model. Physiologically just like other cells, neurons are surrounded by double-lipid membranes separate cytoplasm from extracellular space. Ion pumps maintain concentration gradients across membranes and thus electrical potential. The basic scheme of single compartment models is shown in Figure C-1 [10].

C.1 Conductance-based compartment model

Neuronal cell membranes have been modeled as capacitors separating electric charge. The ion channels across the membrane act as conductance that allows ionic current flow between intracellular and extracellular space. The transmembrane current flow perturbs electrical balance and may initiate action potentials. The reverse potentials E_{Na}, E_K, and E_L exist due to the concentration gradients of ions across the membrane maintained by ion pumps. The current balance equation according to Kirchoff's Law can be written as follows:

$$C\dot{V} = -I_{Na} - I_K - I_L + I_{ex} \tag{C.1}$$

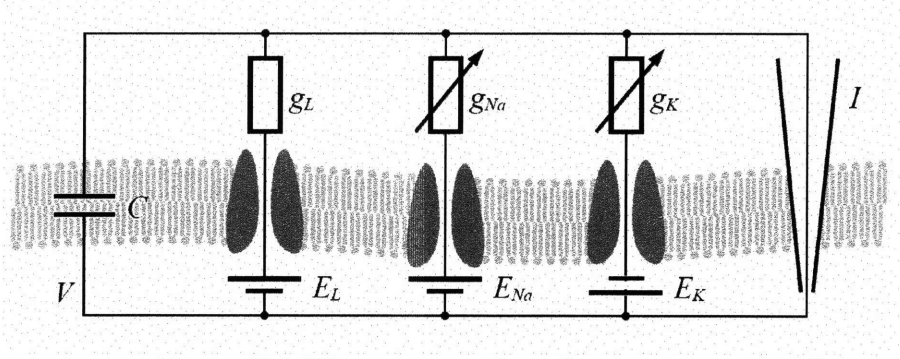

Figure C-1 The representation of compartment model

C.2 Ion channels

For Hodgkin-Huxley model, the types of channels considered include sodium, potassium, and leakage [68]. Each ion channel is selective to specific type of ion. Ionic current through ion channel is determined by the opening and closing of ion channels. The gating variables represent the degree of opening of a certain ion channel and they follow first order kinetics with voltage-dependent rate constants α (V) and β (V). The voltage dependence was determined experimentally and has been formulated into equations [34]. The detailed model for each ion channel is described below. With the system of ordinary differential equations (ODEs) fully defined, four variables with four equations, the ODEs can be integrated to get the response of membrane potential. The resting membrane potential is approximately -65 mV.

Sodium channels are controlled by two gating variables: m and h, both of which depend on the membrane potential. The activation variable m increases with membrane potential while inactivation variable decreases with it. The dynamics of sodium channels are described in Eq. (C.2).

$$
\begin{aligned}
&I_{Na} = g_{Na} m^3 h (V - E_{Na}) \\
&\dot{m} = \alpha_m(V)(1-m) - \beta_m(V)m \\
&\dot{h} = \alpha_h(V)(1-h) - \beta_h(V)h \\
&g_{Na} = 120\ mS/cm^2;\ E_{Na} = -50\ mV \\
&\alpha_m(V) = 0.1(V+40)/(1-\exp(-(V+40)/10)) \\
&\beta_m(V) = 4\exp(-(V+65)/18) \\
&\alpha_h(V) = 0.07\exp(-(V+65)/20) \\
&\beta_h(V) = 1/(1+\exp(-(V+35)/10))
\end{aligned}
\tag{C.2}
$$

Potassium delayed-rectifier current flows through potassium channels which are controlled by one single gating variable n. The variable n grows with respect to membrane voltage. The overall dynamics of potassium channels are described in Eq. (C.3).

$$
\begin{aligned}
&I_K = g_K n^4 (E_K - V) \\
&\dot{n} = \alpha_n(V)(1-n) - \beta_n(V)n \\
&g_K = 36\ mS/cm^2;\ E_K = -77\ mV \\
&\alpha_n(V) = 0.01(V+55)/(1-\exp(-(V+55)/10)) \\
&\beta_n(V) = 0.125\exp(-(V+65)/80)
\end{aligned}
\tag{C.3}
$$

The leakage current, I_L, approximates the passive properties of the cell has linear relationship with the membrane voltage.

$$
\begin{aligned}
&I_L = g_L(E_L - V) \\
&g_L = 0.3\ mS/cm^2;\ E_L = -54.38\ mV
\end{aligned}
\tag{C.4}
$$

C.3 Modulation by using building blocks in Simulink

We used individual modules in Simulink to incorporate the dynamics of ionic channels into the hierarchical model. Modulation can facilitate the reuse of the building blocks and make debugging simpler. There are three levels of model complexity introduced as shown in Figure C-2. The top one outlines the input and output signals. The second level describes the ion channels as conductance and neuronal membrane as capacitor. The connections between building blocks with transfer functions embedded are drawn based upon Hodgkin-Huxley equations. The third level includes the detailed dynamics of both sodium and potassium channels. There are two channel variables (h and m) controlling sodium channels and only one (n) influencing potassium channels.

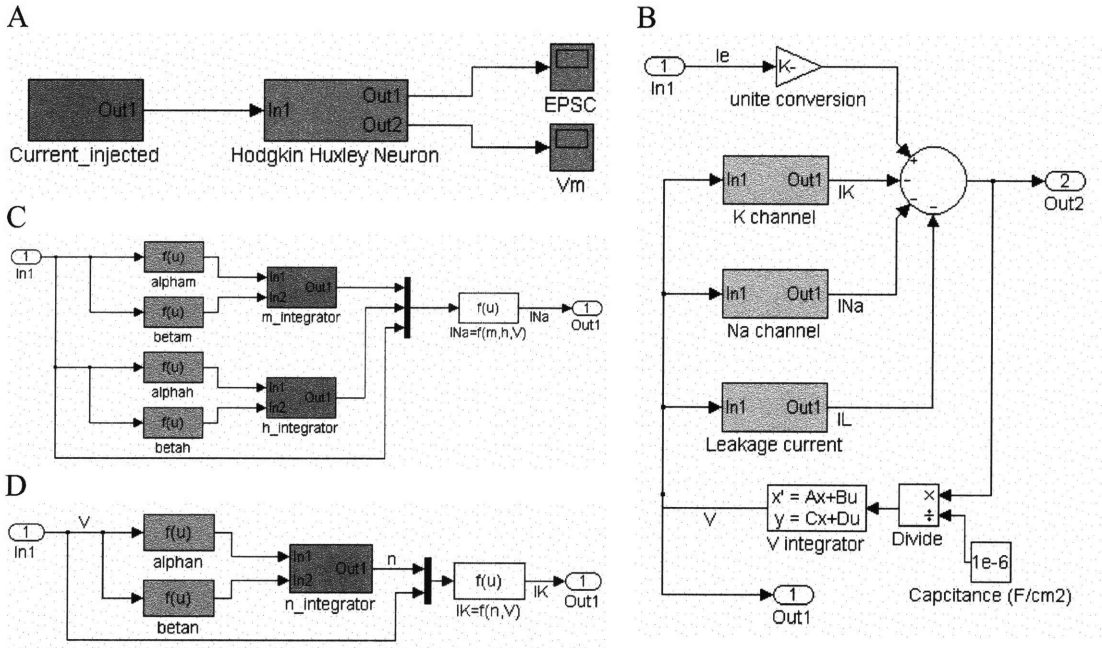

Figure C-2 The hierarchical Simulink structure to implement Hodgkin-Huxley equations. (A) The main directory that takes the current injected as input and exports the excitatory postsynaptic current and membrane potential. (B) The ion channels embedded in the conductance-based model. (C) The detailed structure describing the dynamics of sodium channels. (D) The detailed structure describing the dynamics of potassium channels .

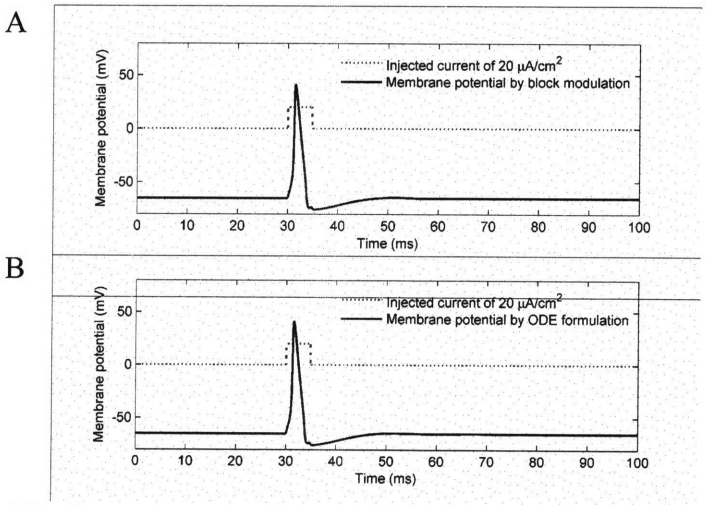

Figure C-3 The input current and output membrane potential based on Hodgkin-Huxley equations.
(A) The response based on standard H-H model. (B) The response based on hierarchical model implemented in Simulink.

C.4 Modification of H-H model

The shapes of action potentials vary significantly, depending on the types and locations of neurons. Although the output of Hodgkin-Huxley equations represents one major type of action potential, it cannot account for all the classes of action potential. Therefore, various spiking models have been developed independently or based on the H-H equations. To model the responses from various types of neuron, a precise simulation of action potentials initiated at the neurons of interest is necessary. There are two aspects of H-H model that we modified for the modeling work of spike timing dependent plasticity. The first is the kinetics of potassium channels and the second is the depolarization after potential behavior.

C.4.1 Change the kinetics of K channels

The recovery rate of potassium channels is described by the two ion channel rate constants $\alpha_n(V)$ and $\beta_n(V)$. While $\alpha_n(V)$ is the opening rate constant, $\beta_n(V)$ is the closing rate constant; both of them are voltage dependent. The potassium current flow through rectifier potassium channels recovers the membrane potential from the hyperpolarization state. Since different kinds of neurons demonstrate different length of the tail after action potential, to control the rate of the recovery, the values of $\alpha_n(V)$ and $\beta_n(V)$ need to be adjusted. As shown in Figure C-4, slow K channels result into long post action potential tail and fast K channel render swifter recovery. For the classical H-H equations (fast K channel), the value pre voltage terms constant of $\alpha_n(V)$ and $\beta_n(V)$ are 0.032 and 0.5, respectively, based on Eq. (C.3). As for slow K channel, those values are adjusted to 0.15; for medium K channel, 0.32.

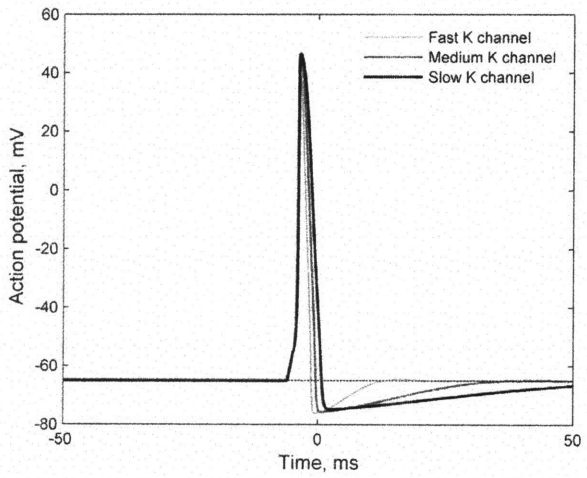

Figure C-4 The output of Hodgkin-Huxley equations with different rates of potassium channel kinetics.

C.4.2 Introduce depolarization after potential

Several types of neurons mentioned in the manuscript demonstrate depolarization after potential (DAP) behavior. These neurons, at the repolarization stage, depolarize instead of hyperpolarize once reaching the resting potential, which is -65 mV according to H-H equations. Therefore, the level of membrane potential does not drop below the steady state value. To implement the introduction of DAP into H-H model, we decided to reverse the hyperpolarization part of the action potential whenever the membrane potential V_m is smaller than -65 mV. The constant k_{DAP} is added to control the degree of depolarization after potential. The detailed Matlab® codes to execute the algorithms are are included in Appendix B.2 and the comparison between the output of classical H-H model and that with DAP behavior is shown in Figure C-5. Larger kDAP represents higher degree of depolarization after potential.

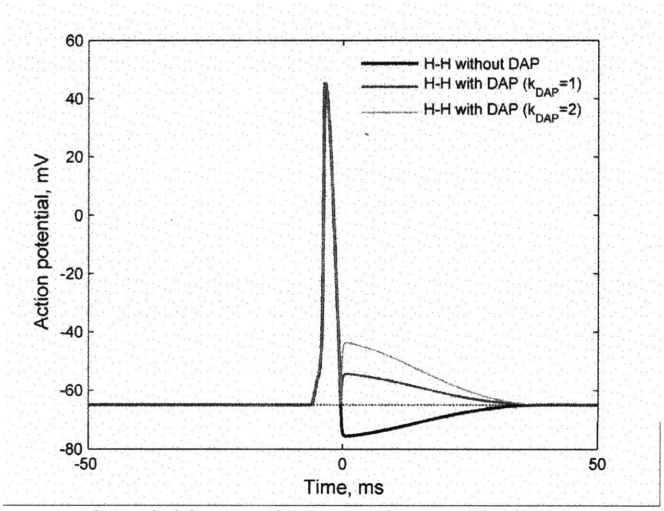

Figure C-5 The output of Hodgkin-Huxley equations with different degree of depolarization after potential (DAP).

Appendix D Artificial Neural Network

Artificial neural network (ANN) is a computational tool inspired by the network of neurons in biological nervous system. It is a network consisting of arrays of artificial neurons linked together with different weights of connection. The states of the neurons as well as the weights of connections among them evolve according to certain learning rules. Practically speaking, neural networks are nonlinear statistical modeling tools which can be used to find the relationship between input and output or to find patterns in vast database. ANN has been applied in statistical model development, adaptive control system, pattern recognition in data mining, and decision making under uncertainty.

D.1 Classical Hebb's Rule

Hebb's rule is a postulate proposed by Donald Hebb in 1949 [65]. It is a learning rule that describes how the neuronal activities influence the connection between neurons, i.e., the synaptic plasticity. It provides an algorithm to update weight of neuronal connection within neural network. Hebb's rule provides a simplistic physiology-based model to mimic the activity dependent features of synaptic plasticity and has been widely used in the area of artificial neural network. Different versions of the rule have been proposed to make the updating rule more realistic.

The weight of connection between neurons is a function of the neuronal activity. The classical Hebb's rule indicates "neurons that fire together, wire together". In the simplest form of Hebb's rule, Eq. (A.1), w_{ij} stands for the weight of the connection from neuron j to neuron i as shown in Figure C-1A. Furthermore, simple artificial network composed of a single layer of perceptron can be constructed. Perceptron can be seen as the simple feedforward network acting as the binary classifier, which is the principal algorithm in Hopfield model.

$$w_{ij} = x_i x_j \tag{D.1}$$

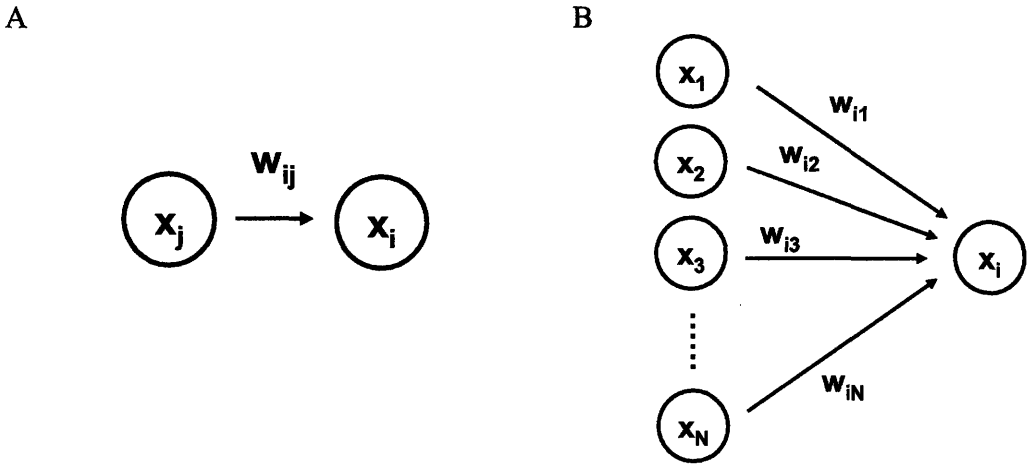

Figure D-1 The plasticity within neural network. (A) The single connection between neuron *i* and neuron *j*. (B) A network of neurons connecting to neuron *i*.

D.2 Hopfield Model

Hopfield model is an associative memory model using the Hebb's rule for all possible pairs ij with binary units. The state variable x_i of the neuron *i* takes on either on of the two possible values: 1 or -1, which corresponds to the firing state or not firing state, respectively. The summary plot of a signal layer Hopfield network is shown in Figure D-3A. A three layer perceptron is demonstrated in Figure D-3B.

$$S_i(t+1) := sgn\left(\sum_j w_{ij} S_j(t) - \mu_i\right) \tag{D.2}$$

Where *sgn* is the sign function defined as follows:

$$sgn(x) = \begin{cases} 1 & if\ x \geq 0 \\ -1 & if\ x < 0 \end{cases} \tag{D.3}$$

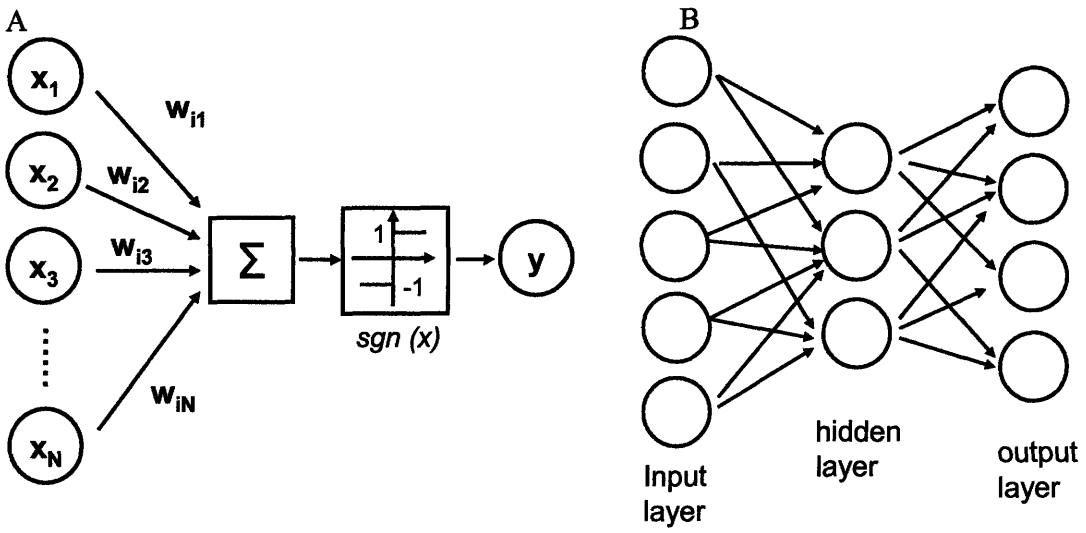

Figure D-2 The schematic diagram of neural network.
(A) Hopfield neuron. The unit fires if the weighted sum $\Sigma_j w_{ij}S_j$ of the inputs reaches or exceeds the threshold μ_i [66]. (B) An example of three layer perceptron.

D.3 The Drawbacks of Hebb's Rule

Though being simple, the classical Hebb's rule has some disadvantages. Depending on the application area of neural network, some drawbacks are tolerable but some need improvement. Generally speaking, for the purpose of data processing and statistical analysis, the speed and power of computation are valued more than the resemblance between the model and the physiological realism. On the other hand, for unraveling the memory formation mechanism and harvesting the emerging properties of biological network, the models need to be built upon a certain degree of biophysical basis.

D.3.1 Stability of Hebbian network

For classical Hebb's rule, there is no algorithm for synapses to get weaker and no upper bound that limits how strong the connectivity can get [93]. Therefore, it is intrinsically unstable. To overcome the stability problem, Bienenstock, Cooper, and Munro proposed an omega shaped learning rule called BCM rule. . The general BCM improves Hebb's rule and takes the following form:

$$\frac{dw_{ij}}{dt} = \varphi(x_i)\cdot x_j - k_w \cdot w_{ij} \qquad \text{(D.4)}$$

There are two main differences between these two rules: the decay of synaptic weight with a rate constant k_w and the nonlinear dependence of synaptic weight with respect to postsynaptic activities. As shown in Figure D-3, Hebb's rule poses linear dependence of synaptic strength on postsynaptic activity while BCM rule sets nonlinear omega-shaped dependence. The nonlinearity was described by the postsynaptic activation function, $\varphi(x)$. For BCM rule, the activation function is negative for x_i under threshold value θ_w but grows positive once the postsynaptic activity becomes larger than θ_w. Such functional dependence can guarantee the limit of synaptic strength as well as provide algorithm for decreasing or weakening synaptic connectivity.

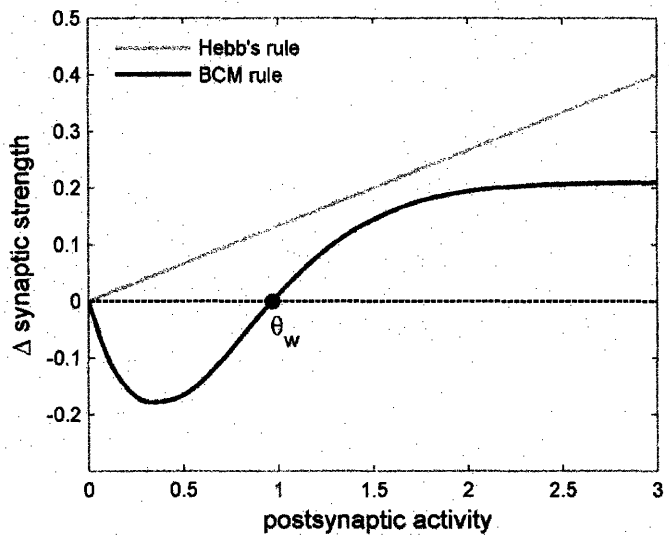

Figure D-3 The activation function of synaptic strength with respect to postsynaptic activity for Hebb's rule and BCM rule. The x-axis corresponds to postsynaptic activity, x_i and the y-axis represents the activation function, $\varphi(x)$ in Eq. (D.4).

D.3.2 The simplification of neuronal activities

Under external stimulation, neurons fire and emit a series of pulses instead of a simple output level. In Hebb's rule, only a single value x_i is assigned to the neuron i to represent its activity. Yet the simplification results into the loss of information such as the threshold and tendency of firing as well as the detailed change in the short-term and the long-term plasticity. The variety and emerging properties may be the results of differentiated neurons. The network of these specialized neurons with individual attributes gives rise to bountiful functionality.

D.3.3 The ability to model spike timing dependence

It has been experimentally shown that the change in synaptic plasticity depends upon the relative spike timing between presynaptic and postsynaptic neurons. Spike timing dependence has become an important experimental protocol in eliciting change in synaptic plasticity since its discovery. Although the role of temporal order was suggested in the original statement of Hebb's rule, the time window requirement is not incorporated in the equations. Thus modification has to be made to improve Hebb's rule.

There are various subtypes of spike timing dependent plasticity (STDP); details are provided in Chapter 6: Modeling Spike Timing Dependent Plasticity. Some synapses demonstrate anti-Hebbian behavior in which presynaptic spiking preceding postsynaptic stimulation results into long term depression instead of potentiation. Still other synapses demonstrate only spike timing dependent potentiation or depression. Therefore, modifying classical Hebb's rule can lead to more versatile and realistic behavior of neural network.

Bibliography

1. Abarbanel HDI, Gibb L, Huerta R, Rabinovich MI (2003) Biophysical model of synaptic plasticity dynamics. Biol Cybern 89:214-226
2. Abarbanel HDI, Huerta R, Rabinovich MI (2002) Dynamical model of long-term synaptic plasticity. Proc Natl Acad Sci USA 99:10132-10137
3. Abbott LF, Varela JA, Sen K, Nelson SB (1997) Synaptic depression and cortical gain control. Science 275:221-224
4. Agena SM, Bogle IDL, Pessoa FLP (1997) An activity coefficient model for proteins. Biotechnol Bioeng 55:65-71
5. Akopian G, Walsh JP (2002) Corticostriatal paired-pulse potentiation produced by voltage-dependent activation of NMDA receptors and L-type Ca^{2+} channels. J Neurophysiol 87:157-165
6. Atluri PP, Regehr WG (1996) Determinants of the time course of facilitation at the granule cell to purkinje cell synapse. J Neurosci 16:5661-5671
7. Augustine GJ (2001) How does calcium trigger neurotransmitter release. Curr Opin Neurobiol 11:320-326
8. Austen B, Christodoulou G, Terry JE (2002) Relation between cholesterol levels, statins and Alzheimer's disease in the human population. J Nutr Health Aging 6:377-382
9. Bell CC, Han VZ, Sugawara Y, Grant K (1997) Synaptic plasticity in a cerebellum-like structure depends on temporal order. Nature 387:278-281
10. Benda J (2002) PhD Thesis: Single Neuron Dynamics Models Linking Theory and Experiment. In: Universität zu Berlin, Berlin, Germany
11. Berkholz R, Guthke R (2001) Model based sequential experimental design for bioprocess optimisation—an overview. Springer, Brussels, Belgium
12. Bertram R, Sherman A, Stanley EF (1996) Single-domain/bound calcium hypothesis of transmitter release and facilitation. J Neurophysiol 75:1919-1931
13. Betz W (1970) Depression of transmitter release at the neuromuscular junction of the frog. J Physiol (Lond) 206:629-644
14. Bhalla US, Iyengar R (1995) Emergent properties of networks of biological signaling pathways. Science 2:381-387
15. Bi G, Poo M (2001) Synaptic modification by correlated activity: Hebb's postulate revisited. Annu Rev Neurosci 24:139-166
16. Bi G, Poo M (1998) Synaptic modifications in cultured hippocampal neurons: dependence on spike timing, synaptic strength, and postsynaptic cell type. J Neurosci 18:10464-10472
17. Bienenstock EL, Cooper LN, Munro PW (1982) Theory for the development of neuron selectivity: orientation specificity and binocular interaction in visual cortex. J Neurosci 2:32-48
18. Bird RB, Stewart WE, Lightfoot EN (2002) Transport Phenomena. John Wiley and Sons, New York City, NY
19. Bitan G, Lomakin A, Teplow DB (2001) Amyloid ß-protein oligomerization prenucleation interactions revealed by photo-induced cross-linking of unmodified proteins. J Biol Chem 276:35176-35184
20. Bliss T, Lømo T (1973) Long-lasting potentiation of synaptic transmission in the dentate area of the anaesthetized rabbit following stimulation of the perforant path. J Physiol 232:331-356

21. Blitz DM, Foster KA, Regehr WG (2004) Short-term synaptic plasticity: a comparison of two synapses. Nat Rev Neurosci 5:630-640
22. Bradshaw JM, Kubota Y, Meyer T, Schulman H (2003) An ultrasensitive Ca^{2+}/calmodulin-dependent protein kinase II-protein phosphatase 1 switch facilitates specificity in postsynaptic calcium signaling. Proc Natl Acad Sci USA 100:10512-10517
23. Burkitt AN, Meffin H, Grayden DB (2004) Spike-timing-dependent plasticity: the relationship to rate-based learning for models with weight dynamics determined by a stable fixed point. Neural Comput 16:885-940
24. Byrne JH (1982) Analysis of synaptic depression contributing to habituation of gill-withdrawal reflex in Aplysia californica. J Neurophysiol 48:431-438
25. Carroll RC, Beattie EC, von Zastrow M, Malenka RC (2001) Role of AMPA receptor endocytosis in synaptic plasticity Nat Rev Neurosci 2:315-324
26. Castellani GC, Quinlan EM, Bersani F, Cooper LN, Shouval HZ (2005) A model of bidirectional synaptic plasticity: From signaling network to channel conductance. Learn Mem 12:423-432
27. Castellani GC, Quinlan EM, Cooper LN, Shouval HZ (2001) A biophysical model of bidirectional synaptic plasticity: Dependence on AMPA and NMDA receptors. Proc Natl Acad Sci USA 98:12772-12777
28. Chen CY, Horowitz JM, Bonham AC (1999) A presynaptic mechanism contributes to depression of autonomic signal transmission in NTS. Am J Physiol Heart Circ Physiol 277:1350-1360
29. Cho K, Aggleton JP, Brown MW, Bashir ZI (2001) An experimental test of the role of postsynaptic calcium levels in determining synaptic strength using perirhinal cortex of rat. J Physiol 532:459-466
30. Clapham DE (1995) Calcium Signaling, Review. Cell 80:259-268
31. Cleary JP, Walsh DM, Hofmeister JJ, Shankar GM, Kuskowski MA, Selkoe DJ, Ashe KH (2005) Natural oligomers of the amyloid-ß protein specifically disrupt cognitive function. Nat Neurosci 8:79-84
32. Collins SR, Douglass A, Vale RD, Weissman JS (2004) Mechanism of prion propagation: amyloid growth occurs by monomer addition. PLoS Biol 2:1582–1590
33. Dan Y, Poo MM (2006) Spike timing-dependent plasticity: from synapse to perception. Physiol Rev 86:1033-1048
34. Dayan P, Abbott LF (2001) Theoretical neuroscience: computational and mathematical modeling of neural systems. MIT Press, Cambridge, MA
35. Dekay JG, Chang TC, Mills N, Speed HE, Dobrunz LE (2006) Responses of excitatory hippocampal synapses to natural stimulus patterns reveal a decrease in short-term facilitation and increase in short-term depression during postnatal development. Hippocampus 16:66-79
36. Del Castillo J, Katz B (1954) Statistical factors involved in neuromuscular facilitation and depression. J Physiol (Lond) 124:574-585
37. Destexhe A, Mainen ZF, Sejnowski TJ (1994) Synthesis of models for excitable membranes, synaptic transmission and neuromodulation using a common kinetic formalism. J Compu Neurosci 1:195-230
38. Dittman JS, Kreitzer AC, Regehr WG (2000) Interplay between facilitation, depression, and residual calcium at three presynaptic terminals. J Neurosci 20:1374-1385
39. Dittman JS, Regehr WG (1998) Calcium dependence and recovery kinetics of presynaptic depression at the climbing fiber to Purkinje cell synapse. J Neurosci 18:6147-6162

40. Dodge Jr FA, Rahamimoff R (1967) Co-operative action a calcium ions in transmitter release at the neuromuscular junction. J Physiol 193:419-432
41. Dudek SM, Bear MF (1992) Homosynaptic long-term depression in area CA1 of hippocampus and effects of N-methyl-D-aspartate receptor blockade. Proc Natl Acad Sci USA 89:4363-4367
42. Edelstein-Keshet L (2005) Mathematical Models in Biology. Society for Industrial and Applied Mathematics, Philadelphia, PA
43. Egger V, Feldmeyer D, Sakmann B (1999) Coincidence detection and changes of synaptic efficacy in spiny stellate neurons in rat barrel cortex. Nat Neurosci 2:1098-1105
44. English JD, Sweatt JD (1997) A requirement for the mitogen-activated protein kinase cascade in hippocampal long term potentiation. J Biol Chem 272:19103-19106
45. Evans KC, Berger EP, Cho CG, Weisgraber KH, Lansbury Jr PT (1995) Apolipoprotein E is a kinetic but not a thermodynamic inhibitor of amyloid formation: implications for the pathogenesis and treatment of Alzheimer disease. Proc Natl Acad Sci USA 92:763-767
46. Fernández-Chacón R, Königstorfer A, Gerber SH, García J, Matos MF, Stevens CF, Brose N, Rizo J, Rosenmund C, Südhof TC (2001) Synaptotagmin I functions as a calcium regulator of release probability. Nature 410:41-49
47. Flyvbjerg H, Jobs E, Leibler S (1996) Kinetics of self-assembling microtubules: an "inverse problem" in biochemistry. Proc Natl Acad Sci USA 93:5975-5979
48. Fogler HS (1998) Elements of chemical reaction engineering. Prentice-Hall, Upper Saddle River, NJ.
49. Fortune E, Rose G (2001) Short-term synaptic plasticity as a temporal filter. Trends Neurosci 24:381-385
50. Fowler DM, Koulov AV, Alory-Jost C, Marks MS, Balch WE, Kelly JW (2006) Functional amyloid formation within mammalian tissue. PLoS Biol 4:100-107
51. Freudenrich CC (2001) How Your Brain Works. In: Howstuffworks (http://www.howstuffworks.com/brain1.htm)
52. Froemke RC, Poo MM, Dan Y (2005) Spike-timing-dependent synaptic plasticity depends on dendritic location. Nature 434:221-225
53. Ghosh S, Mukherjee A, Sadler Peter J, Verma S (2008) Periodic iron nanomineralization in human serum transferrin fibrils. Angew Chem 120:2249-2253
54. Gill R (1994) Protein engineering of insulin-like growth factor. PhD Thesis. In:University of London, London, UK
55. Gingrich KJ, Byrne JH (1985) Simulation of synaptic depression, posttetanic potentiation, and presynaptic facilitation of synaptic potentials from sensory neurons mediating gill-withdrawal reflex in Aplysia. J Neurophys 53:652-669
56. Gosal WS, Morten IJ, Hewitt EW, Smith DA, Thomson NH, Radford SE (2005) Competing pathways determine fibril morphology in the self-assembly of ß2-microglobulin into amyloid. J Mol Biol 351:850-864
57. Gustafsson B, Wigstrom H (1986) Hippocampal long-lasting potentiation produced by pairing single volleys and brief conditioning tetani evoked in separate afferents. J Neurosci 6:1575
58. Han VZ, Grant K, Bell CC (2000) Reversible associative depression and nonassociative potentiation at a parallel fiber synapse. Neuron 27:611-622
59. Hardy J, Selkoe DJ (2002) The amyloid hypothesis of Alzheimer's disease: progress and problems on the road to therapeutics. Science 297:353

60. Hasegawa K, Ono K, Yamada M, Naiki H (2002) Kinetic modeling and determination of reaction constants of Alzheimer's b-amyloid fibril extension and dissociation using surface plasmon resonance. Biochemistry 41:13489–13498
61. Hashimoto K, Kano M (1998) Presynaptic origin of paired-pulse depression at climbing fibre-Purkinje cell synapses in the rat cerebellum. J Physiol 506:391-405
62. Hassiepen U, Federwisch M, Mulders T, Wollmer A (1999) The lifetime of insulin hexamers. Biophys J 77:1638-1654
63. Hayashi H, Campenot RB, Vance DE, Vance JE (2001) Apolipoprotein E-containing lipoproteins protect neurons from apoptosis via a signaling pathway involving low-density lipoprotein receptor-related protein-1. J Neurosci 27:254-266
64. Hayashi Y, Shi SH, Esteban JA, Piccini A, Poncer JC, Malinow R (2000) Driving AMPA receptors into synapses by LTP and CaMKII: requirement for GluR1 and PDZ domain interaction. Science 287:2262-2267
65. Hebb D (1949) The Organization of Behavior. A Neuropsychological Theory. Wiley, New York, NY
66. Hertz J, Krogh A, Palmer RG (1991) Introduction to the theory of neural computation. Addison-Wesley Publishing Company, Redwood City, CA
67. Hines M (1993) NEURON—a program for simulation of nerve equations. Kluwer Academic Publishers, San Francisco, CA
68. Hodgkin A, Huxley A (1952) A quantitative description of membrane current and its application to excitation and conduction in nerve. J Physiol 117:500-544
69. Holmgren C, Harkany T, Svennenfors B, Zilberter Y (2003) Pyramidal cell communication within local networks in layer 2/3 of rat neocortex. J Physiol 551:139-153
70. Hong DP, Fink AL (2005) Independent heterologous fibrillation of insulin and its β-chain peptide. Biochemistry 44:16701-16709
71. Hsieh H, Boehm J, Sato C, Iwatsubo T, Tomita T, Sisodia S, Malinow R (2006) AMPAR removal underlies Aß-induced synaptic depression and dendritic spine loss. Neuron 52:831-843
72. Izhikevich EM (2004) Which model to use for cortical spiking neurons? IEEE Trans Neural Networks 15:1063-1070
73. Izhikevich EM, Desai NS, Walcott EC, Hoppensteadt FC (2003) Bursts as a unit of neural information: selective communication via resonance. Trends Neurosci 26:161-167
74. Jahr CE, Stevens CF (1990) Voltage dependence of NMDA-activated macroscopic conductances predicted by single-channel kinetics. J Neurosci 10:3178-3182
75. Jimenez JL, Nettleton EJ, Bouchard M, Robinson CV, Dobson CM, Saibil HR (2002) The protofilament structure of insulin amyloid fibrils. Proc Natl Acad Sci USA 99:9196–9201
76. Kandel ER (2001) The molecular biology of memory storage: A dialog between genes and synapses. Science 294:1030-1038
77. Kandel ER, Schwartz JH, Jessell TM (2000) Principles of neural science. McGraw-Hill New York, NY
78. Karmarkar UR, Buonomano DV (2002) A model of spike-timing dependent plasticity: one or two coincidence detectors? J Neurophysiol 88:507-513
79. Katz B, Miledi R (1968) The role of calcium in neuromuscular facilitation. J Physiol (Lond) 195:481-492
80. Kayed R, Head E, Thompson JL, McIntire TM, Milton SC, Cotman CW, Glabe CG (2003) Common structure of soluble amyloid oligomers implies common mechanism of pathogenesis. Science 300:486-489

81. Khurana R, Ionescu-Zanetti C, Pope M, Li J, Nielson L, Ramirez-Alvarado M, Regan L, Fink AL, Carter SA (2003) A general model for amyloid fibril assembly based on morphological studies using atomic force microscopy. Biophys J 85:1135-1144
82. King ME, Kan HM, Baas PW, Erisir A, Glabe CG, Bloom GS (2006) Tau-dependent microtubule disassembly initiated by prefibrillar β-amyloid. J Cell Biol 175:541-546
83. Kingsland SE (1995) Modeling Nature. University of Chicago Press, Chicago, IL
84. Korn H, Faber DS, Burnod Y, Triller A (1984) Regulation of efficacy at central synapses. J Neurosci 4:125-130
85. Koudinov AR, Berezov TT (2005) Cholesterol, statins, and Alzheimer disease. PLoS Med 2:e81
86. Koudinov AR, Koudinova NV (2005) Cholesterol homeostasis failure as a unifying cause of synaptic degeneration. J Neurol Sci 229:233–240
87. Krishnan R, Lindquist SL (2005) Structural insights into a yeast prion illuminate nucleation and strain diversity. Nature 435:765-772
88. Kusano K, Landau EM (1975) Depression and recovery of transmission at the squid giant synapse. J Physiol 245:13-32
89. Lashuel HA, Lansbury PT (2006) Are amyloid diseases caused by protein aggregates that mimic bacterial pore-forming toxins? Cambridge University Press, Cambridge, UK.
90. Lee CC, Nayak A, Belfort G, McRae GJ (2006) A mathematical model of amyloid fibrillation: the case for insulin. In: Biophysical Society Conference. Salt Lake City, Utah.
91. Lee HK, Barbarosie M, Kameyama K, Bear MF, Huganir RL (2000) Regulation of distinct AMPA receptor phosphorylation sites during bidirectional synaptic plasticity. Nature 405:955-959
92. Lee HK, Kameyama K, Huganir RL, Bear MF (2003) NMDA induces long-term synaptic depression and dephosphorylation of the GluR1 subunit of AMPA receptors in hippocampus. Neuron 112:631-643
93. Leon NC (2000) Memories and memory: a physicist's approach to the brain. International Journal of Modern Physics A 15:4069-4082
94. Levenspiel O (1999) Chemical Reaction Engineering. John Wiley and Sons, New York City, NY
95. Levey AI (1996) Muscarinic acetylcholine receptor expression in memory circuits: Implications for treatment of Alzheimer disease. Proc Natl Acad Sci USA 93:13541
96. LeVine III H (2005) Multiple ligand binding sites on Aß (1–40) fibrils. Protein Folding Symposium #7, Amyloids 12:5-14
97. LeVine III H (1999) Quantification of beta-sheet amyloid fibril structures with thioflavin T. Methods Enzymol 309:274-284
98. Lisman J (1989) A mechanism for the Hebb and the anti-Hebb processes underlying learning and memory. Proc Natl Acad Sci USA 86:9574-9578
99. Liu Y, Lashuel HA, Choi S, Xing X, Case A, Ni J, Yeh LA, Cuny GD, Stein RL, Lansbury PT (2003) Discovery of inhibitors that elucidate the role of UCH-L1 activity in the H1299 lung cancer cell line. Chem Biol 10:837-846
100. Lomakin A, Teplow DB, Kirschner DA, Benedek GB (1997) Kinetic theory of fibrillogenesis of amyloid beta-protein. Proc Natl Acad Sci USA 94:7942–7947
101. Lu Q, Wood JG (1993) Functional studies of Alzheimer's disease tau protein. J Neurosci 13:508-515

102. MacLeod KM, Horiuchi TK, Carr CE (2007) A role for short-term synaptic facilitation and depression in the processing of intensity Information in the auditory brain stem. J Neurophysiol 97:2863-2874
103. Malenka RC, Nicoll RA (1999) Long-term potentiation--a decade of progress? Science 285:1870-1874
104. Manno M, Craparo EF, Martorana V, Bulone D, San Biagio PL (2006) Kinetics of insulin aggregation: disentanglement of amyloid fibrillation from large-size cluster formation. Biophys J 90:4585-4591
105. Markram H, Lübke J, Frotscher M, Sakmann B (1997) Regulation of synaptic efficacy by coincidence of postsynaptic APs and EPSPs. Science 275:213-215
106. Markram H, Wang Y, Tsodyks M (1998) Differential signaling via the same axon of neocortical pyramidal neurons. Proc Natl Acad Sci USA 95:5323-5328
107. Matveev V, Wang XJ (2000) Implications of all-or-none synaptic transmission and short-term depression beyond vesicle depletion: a computational study. J Neurosci 20:1575-1588
108. Mayr B, Montminy M (2001) Transcriptional regulation by the phosphorylation-dependent factor CREB. Nat Rev Mol Cell Biol 2:599-609
109. Meyer-Luehmann M, Spires-Jones TL, Prada C, Garcia-Alloza M, de Calignon A, Rozkalne A, Koenigsknecht-Talboo J, Holtzman DM, Bacskai BJ, Hyman BT (2008) Rapid appearance and local toxicity of amyloid-β plaques in a mouse model of Alzheimer's disease. Nature 451:720-724
110. Michaelis M, Menten ML (1913) Kinetics of invertase action. Z Biochem 49:333-369
111. Miller DP, de Pablo JJ (2000) Calorimetric solution properties of simple saccharides and their significance for the stabilization of biological structure and function. J Phys Chem B 104:8876-8883
112. Mukaetova-Ladinska EB, Garcia-Siera F, Hurt J, Gertz HJ, Xuereb JH, Hills R, Brayne C, Huppert FA, Paykel ES, McGee M (2000) Staging of cytoskeletal and ß-amyloid changes in human isocortex reveals biphasic synaptic protein response during progression of Alzheimer's disease. Am J Pathol 157:623-636
113. Mulkey RM, Herron CE, Malenka RC (1993) An essential role for protein phosphatases in hippocampal long-term depression. Science 261:1051-1055
114. Neher E, Augustine GJ (1992) Calcium gradients and buffers in bovine chromaffin cells. J Physiol (Lond) 450:273-301
115. Nelson R, Sawaya MR, Balbirnie M, Madsen AO, Riekel C, Grothe R, Eisenberg D (2005) Structure of the cross-β spine of amyloid-like fibrils. Nature 435:773-778
116. Nguyen HD, Hall CK (2004) Molecular dynamics simulations of spontaneous fibril formation by random-coil peptides. Proc Natl Acad Sci USA 101:16180-16185
117. Nielsen L, Khurana R, Coats A, Frokjaer S, Brange J, Vyas S, Uversky VN, Fink AL (2001) Effect of environmental factors on the kinetics of insulin fibril formation: elucidation of the molecular mechanism. Biochemistry 40:6036-6046
118. Nishiyama M, Hong K, Mikoshiba K, Poo MM, Kato K (2000) Calcium stores regulate the polarity and input specificity of synaptic modification. Nature 408:584-588
119. O'Connor DH, Wittenberg GM, Wang SSH (2005) Graded bidirectional synaptic plasticity is composed of switch-like unitary events. Proc Natl Acad Sci USA 102:9679-9684
120. O'Neil PV (1995) Advanced engineering mathematics. PWS Publishing Company, Boston, MA

121. Osterbye T, Jorgensen KH, Fredman P, Tranum-Jensen J, Kaas A, Brange J, Whittingham JL, Buschard K (2001) Sulfatide promotes the folding of proinsulin, preserves insulin crystals, and mediates its monomerization. Glycobiology 11:473-479
122. Padrick SB, Miranker AD (2002) Islet amyloid: phase partitioning and secondary nucleation are central to the mechanism of fibrillogenesis. Biochemistry 41:4694-4703
123. Pallitto MM, Murphy RM (2001) A mathematical model of the kinetics of ß-amyloid fibril growth from the denatured state. Biophys J 81:1805-1822
124. Parnas H, Segel LA (1981) A theoretical study of calcium entry in nerve terminals, with application to neurotransmitter release. J Theor Biol 91:125-169
125. Pasternack RF, Gibbs EJ, Sibley S, Woodard L, Hutchinson P, Genereux J, Kristian K (2006) Formation kinetics of insulin-based amyloid gels and the effect of added metalloporphyrins. Biophys J 90:1033-1042
126. Poon CS, Young DL (2006) Nonassociative learning as gated neural integrator and differentiator in stimulus-response pathways. Behav Brain Funct 2:29
127. Quist A, Doudevski I, Lin H, Azimova R, Ng D, Frangione B, Kagan B, Ghiso J, Lal R (2005) Amyloid ion channels: A common structural link for protein-misfolding disease. Proc Natl Acad Sci USA 102:10427-10432
128. Richardson MJE, Melamed O, Silberberg G, Gerstner W, Markram H (2005) Short-term synaptic plasticity orchestrates the response of pyramidal cells and interneurons to population bursts. J Computat Neurosci 18:323-331
129. Rizzuto R, Pozzan T (2006) Microdomains of intracellular Ca^{2+}: molecular determinants and functional consequences. Physiol Rev 86:369-408
130. Rosenmund C, Sigler A, Augustin I, Reim K, Brose N, Rhee JS (2002) Differential control of vesicle priming and short-term plasticity by Munc13 isoforms. Neuron 33:411-424
131. Rozov A, Burnashev N, Sakmann B, Neher E (2001) Transmitter release modulation by intracellular Ca2+ buffers in facilitating and depressing nerve terminals of pyramidal cells in layer 2/3 of the rat neocortex indicates a target cell-specific difference in presynaptic calcium dynamics. J Physiol 531:807-826
132. Scheibel T, Bloom J, Lindquist SL (2004) The elongation of yeast prion fibers involves separable steps of association and conversion. Proc Natl Acad Sci USA 101:2287-2292
133. Schlüter OM, Basu J, Südhof TC, Rosenmund C (2006) Rab3 superprimes synaptic vesicles for release: implications for short-term synaptic plasticity. J Neurosci 26:1239-1246
134. Schneggenburger R, Sakaba T, Neher E (2002) Vesicle pools and short-term synaptic depression: lessons from a large synapse. Trends Neurosci 25:206-212
135. Scott LJ, Goa KL (2000) Galantamine: a review of its use in Alzheimer's disease. Drugs 60:1095-1122
136. Seber GAF, Lee AJ (2003) Linear Regression Analysis. American Statistical Association, Hoboken, NJ
137. Seber GAF, Wild CJ (2003) Nonlinear Regression. Wiley, Hoboken, NJ
138. Seinfeld JH, Pandis SN (1998) Atmospheric chemistry and physics: from air pollution to climate change. John Wiley and Sons, New York City, NY
139. Selkoe DJ (2002) Alzheimer's disease is a synaptic failure. Science 298:789-791
140. Selkoe DJ (2001) Alzheimer's disease: genes, proteins, and therapy. Physiol Rev 81:741-766

141. Selkoe DJ (2004) Cell biology of protein misfolding: The examples of Alzheimer's and Parkinson's diseases. Nat Cell Biol 6:1054-1061
142. Serio TR, Cashikar AG, Kowal AS, Sawicki GJ, Moslehi JJ, Serpell L, Arnsdorf MF, Lindquist SL (2000) Nucleated conformational conversion and the replication of conformational information by a prion determinant. Science 289:1317–1321
143. Shoghi-Jadid K, Barrio JR, Kepe V, Wu HM, Small GW, Phelps ME, Huang SC (2005) Imaging ß-amyloid fibrils in Alzheimer's disease: a critical analysis through simulation of amyloid fibril polymerization. Nucl Med Biol 32:337-351
144. Shouval HZ, Bear MF, Cooper LN (2002) A unified model of NMDA receptor-dependent bidirectional synaptic plasticity. Proc Natl Acad Sci USA 99:10831-10836
145. Simons-Weidenmaier N, Weber M, Plappert C, Pilz P, Schmid S (2006) Synaptic depression and short-term habituation are located in the sensory part of the mammalian startle pathway. BMC Neurosci 7:38-51
146. Sipe JD (2005) Amyloid Protein: The Beta Sheet Conformation and Disease. John Wiley and Sons, New York, NY
147. Sippy T, Cruz-Martin A, Jeromin A, Schweizer FE (2003) Acute changes in short-term plasticity at synapses with elevated levels of neuronal calcium sensor-1. Nat Neurosci 6:1031-1038
148. Sluzky V, Tamada JA, Klibanov AM, Langer R (1991) Kinetics of insulin aggregation in aqueous solutions upon agitation in the presence of hydrophobic surfaces. Proc Natl Acad Sci USA 88:9377-9381
149. Smith MA, Harris PLR, Sayre LM, Perry G (1997) Iron accumulation in Alzheimer disease is a source of redox-generated free radicals. Proc Natl Acad Sci USA 94:9866-9868
150. Snyder EM, Nong Y, Almeida CG, Paul S, Moran T, Choi EY, Nairn AC, Salter MW, Lombroso PJ, Gouras GK (2005) Regulation of NMDA receptor trafficking by amyloid-bold beta. Nat Neurosci 8:1051-1058
151. Song S, Miller KD, Abbott LF (2000) Competitive Hebbian learning through spike-timing-dependent synaptic plasticity. Nat Neurosci 3:919-926
152. Stevens CF, Wang Y (1995) Facilitation and depression at single central synapses. Neuron 14:795-802
153. Stokin GB, Lillo C, Falzone TL, Brusch RG, Rockenstein E, Mount SL, Raman R, Davies P, Masliah E, Williams DS (2005) Axonopathy and transport deficits early in the pathogenesis of Alzheimer's Disease. Science 307:1282-1288
154. Strogatz SH (1994) Nonlinear dynamics and chaos: with applications to physics, biology, chemistry, and engineering. Perseus Books, Cambridge, MA
155. Südhof TC (2004) The synaptic vesicle cycle. Annu Rev Neurosci 27:509-547
156. Sun HY, Dobrunz LE (2006) Presynaptic kainate receptor activation is a novel mechanism for target cell-specific short-term facilitation at Schaffer collateral synapses. J Neurosci 26:10796-10807
157. Thies RE (1965) Neuromuscular depression and the apparent depletion of transmitter in mammalian muscle. J Neurophysiol 28:427-442
158. Thomson AM (2000) Facilitation, augmentation and potentiation at central synapses. Trends Neurosci 23:305-312
159. Trussell LO, Zhang S, Raman IM (1993) Desensitization of AMPA receptors upon multiquantal neurotransmitter release. Neuron 10:1185-1196
160. Tsodyks MV, Markram H (1997) The neural code between neocortical pyramidal neurons depends on neurotransmitter release probability. Proc Natl Acad Sci USA 94:719-723

161. Ulrich D (2002) Dendritic resonance in rat neocortical pyramidal cells. J Neurophysiol 87:2753-2759
162. Verhulst PF (1844) Recherches mathématiques sur la loi d'accroissement de la population. Mem Acad Roy, Brussels, Belgium
163. Vitolo OV, Sant'Angelo A, Costanzo V, Battaglia F, Arancio O, Shelanski M (2002) Amyloid ß-peptide inhibition of the PKA/CREB pathway and long-term potentiation: Reversibility by drugs that enhance cAMP signaling. Proc Natl Acad Sci USA 99:13217-13221
164. von Gersdorff H, Borst JGG (2002) Short-term plasticity at the calyx of Held. Nat Rev Neurosci 3:53-64
165. von Gersdorff H, Schneggenburger R, Weis S, Neher E (1997) Presynaptic depression at a Calyx synapse: the small contribution of metabotropic glutamate receptors. J Neurosci 17:8137-8146
166. Wakerly JF (1994) Digital design: principles and practices. Prentice-Hall, Upper Saddle River, NJ
167. Wang F, Hull RL, Vidal J, Cnop M, Kahn SE (2001) Islet amyloid develops diffusely throughout the pancreas before becoming severe and replacing endocrine cells. Diabetes 50:2514–2520
168. Wang Q, Walsh DM, Rowan MJ, Selkoe DJ, Anwyl R (2004) Block of long-term potentiation by naturally secreted and synthetic amyloid β-peptide in hippocampal slices is mediated via activation of the kinases c-Jun N-terminal kinase, cyclin-dependent kinase 5, and p38 mitogen-activated protein kinase as well as metabotropic glutamate receptor type 5 J Neurosci 24:3370-3378
169. Wang Y, Ju W, Liu L, Fam S, D'Souza S, Taghibiglou C, Salter M, Wang YT (2004) AMPA endocytosis is essential for NMDA-induced neuronal apoptosis. J Biol Chem 279:41267-41270
170. Weimer RM, Jorgensen EM (2003) Controversies in synaptic vesicle exocytosis. J Cell Sci 116:3661-3666
171. Whitehead A, Rabinovich MI, Huerta R, Zhigulin VP, Abarbanel HDI (2003) Dynamical synaptic plasticity: a model and connection to some experiments. Biol Cybern 88:229-235
172. Wittenberg GM, Wang SSH (2006) Malleability of spike-timing-dependent plasticity at the CA3-CA1 synapse. J Neurosci 26:6610-6617
173. Wood JG, Mirra SS, Pollock NJ, Binder LI (1986) Neurofibrillary tangles of Alzheimer disease share antigenic determinants with the axonal microtubule-associated protein tau (τ). Proc Natl Acad Sci USA 83:4040-4043
174. Wood SJ, Wypych J, Steavenson S, Louis JC, Citron M, Biere AL (1999) α-synuclein fibrillogenesis is nucleation-dependent J Biol Chem 274:19509-19512
175. Wu LG, Betz WJ (1998) Kinetics of synaptic depression and vesicle recycling after tetanic stimulation of frog motor nerve terminals. Biophys J 74:3003-3009
176. Xiong W, Ferrell JE (2003) A positive-feedback-based bistable 'memory module' that governs a cell fate decision. Nature 426:460-465
177. Xu J, He L, Wu L-G (2007) Role of Ca^{2+} channels in short-term synaptic plasticity. Curr Opin Neurobiol 17:352-359
178. Xu J, Wu LG (2005) The decrease in the presynaptic calcium current is a major cause of short-term depression at a calyx-type synapse. Neuron 46:633-645
179. Yamada WM, Zucker RS (1992) Time course of transmitter release calculated from simulations of a calcium diffusion model. Biophys J 61:671-682
180. Yang SN, Tang YG, Zucker RS (1999) Selective Induction of LTP and LTD by Postsynaptic $[Ca^{2+}]_i$ Elevation. J Neurophysiol 81:781-787

181. Zhou Z, Champagnat J, Poon CS (1997) Phasic and long-term depression in brainstem nucleus tractus solitarius neurons: differing roles of AMPA receptor desensitization. J Neurosci 17:5349-5356
182. Zucker RS (1989) Short-term synaptic plasticity. Ann Rev Neurosci 12:13-31
183. Zucker RS, Regehr WG (2002) Short-term synaptic plasticity. Annu Rev Physiol 64:355-405